Avalanching on dunes and its effects:

Size statistics, stratification, & seismic surveys

Matthew Iain Arran

St. Catharine's College

UNIVERSITY OF CAMBRIDGE

May 2018

A dissertation submitted for the degree of Doctor of Philosophy

Summary

Geophysical research has long been interdisciplinary, with many phenomena on the Earth's surface involving multiple, linked processes that are best understood using a combination of techniques. This is particularly true in the case of grain flows on sand dunes, in which the sedimentary stratification with which geologists are concerned arises from the granular processes investigated by physicists and engineers, and the water permeation that interests hydrologists and soil scientists determines the seismic velocities of concern to exploration geophysicists.

In this dissertation, I describe four projects conducted for the degree of Doctor of Philosophy, using a combination of laboratory experimentation, fieldwork, numerical simulation, and mathematical modelling to link avalanching on dunes to its effects on stratification, on the permeation of water, and on seismic surveys.

Firstly, I describe experiments on erodible, unbounded, grain piles in a channel, slowly supplied with additional grains, and I demonstrate that the behaviour of the consequent, discrete avalanches alternates between two regimes, typified by their size statistics. Reconciling the 'self-organised criticality' that several authors have predicted for such a system with the hysteretic behaviour that others have observed, the system exhibits quasi-periodic, system-spanning avalanches in one regime, while in the other avalanches pass at irregular intervals and have a power-law size distribution.

Secondly, I link this power-law size distribution to the strata emplaced by avalanches on bounded grain piles. A low inflow rate of grains into an experimental channel develops a pile, composed of strata in which blue-dyed, coarser grains overlie finer grains. Associating stopped avalanche fronts with the ‘trapped kinks’ described by previous authors, I show that, in sufficiently large grain piles, mean stratum width increases linearly with distance downslope. This implies the possibility of interpreting paleodune height from the strata of aeolian sandstones, and makes predictions for the structure of avalanche-associated strata within active dunes.

Thirdly, I discuss investigations of these strata within active, Qatari barchan dunes, using dye-infiltration to image strata in the field and extracting samples across individual strata with sub-centimetre resolution. Downslope increases in mean stratum width are evident, while measurements of particle size distributions demonstrate preferential permeation of water along substrata composed of finer particles, explaining the strata-associated, localised regions of high water content discovered by other work on the same dunes.

Finally, I consider the effect of these within-dune variations in water content on seismic surveys for oil and gas. Having used high performance computing to simulate elastic wave propagation in the vicinity of an isolated, barchan sand dune, I demonstrate that such a dune acts as a resonator, absorbing energy from Rayleigh waves and reemitting it over an extensive period of time. I derive and validate a mathematical framework that uses bulk properties of the dune to predict quantitative properties of the emitted waves, and I demonstrate the importance of internal variations in seismic velocity, resulting from variations in water content.

Contents

Declaration

This dissertation is the result of my own work and includes nothing which is the outcome of work done in collaboration except as declared in the Acknowledgements and specified in the text.

It is not substantially the same as any that I have submitted, or, is being concurrently submitted for a degree or diploma or other qualification at the University of Cambridge or any other University or similar institution. I further state that no substantial part of my dissertation has already been submitted, or, is being concurrently submitted for any such degree, diploma or other qualification at the University of Cambridge or any other University or similar institution.

It does not exceed the prescribed word limit for the Degree Committee of the Faculty of Maths, as no such word limit exists.

Acknowledgements

This work was supported by a PhD studentship within the Cambridge Earth Systems Science Doctoral Training Partnership (ESS DTP), funded by the National Environmental Research Council, grant number NE/L002507/1. Additional support was provided by Schlumberger Cambridge Research (SCR), through a CASE studentship. I am grateful for both studentships, for the development opportunities provided by the ESS DTP, and for Ed Kragh and Jon-Fredrik Hopperstad's support for the project at SCR.

My travel has been partially supported by St. Catharine's College, by Gordon Research Conferences, and by the American Geophysical Union. I've gained a great deal from the intellectual atmospheres that each fosters, which have contributed to my belief in the value of interdisciplinary communication.

While conducting this work, I have been based at the Department for Applied Mathematics and Theoretical Physics (DAMTP) and at SCR. At both locations, I have been fortunate to be surrounded by excellent facilities, kind and hardworking support staff, supportive colleagues, and senior researchers who have been generous with their time. The G.K. Batchelor Laboratory at DAMTP relies upon the work of Mark Hallworth, its safety officer, and especially upon that of Stuart Dalziel, its director; I am indebted to both of them. Very little of this project would have been possible without the time and expertise of the Laboratory's technicians, with whom it has been a pleasure to work: David Page-Croft, Paul Mitton, Colin Hitch, Andy Denson, and John Milton. All my apparatus was designed in collaboration with them and constructed by them.

The work described in chapter 4 was conducted in a large, interdisciplinary collaboration,

funded by the Qatar National Research Foundation and led by Michel Louge. I am appreciative of all those who made my work in Qatar possible and am particularly grateful for the contributions of Anthony Hay and Michel Louge. Anthony had a significant influence on the design of sampling methods and extracted four sets of samples himself, while Michel shaped the aims of the work, my approach to fieldwork, and the interpretation of results. Alexandre Valance facilitated the analysis of six sets of samples, which was conducted by Jean-Luc Métayer at INSA in Rennes. At the Cambridge Department of Geography, Chris Rolfe facilitated my analysis of ten more sets of samples.

The work described in chapter 5 was conducted at SCR and supervised by Everhard Muyzert, who conceived of the project, guided its development, and reviewed drafts of the manuscript from which the chapter was derived. I am very grateful to him for introducing me to the field of seismology, in which I will be conducting further research.

My doctoral studies have been supervised by Nathalie Vriend, to whom the extent of my gratitude is immeasurable. From introducing me to the field of granular matter via a fourth year undergraduate project to reviewing this dissertation, through four field expeditions, four paper submissions, and over a dozen presentations, Nathalie has always given her time and her wisdom generously. I am unceasingly impressed with her dedication to supporting more-junior researchers and to communicating science as clearly as possible, whether in specialist publications or to the general public.

I would not be here without the support of my parents and brothers[a], or that of those who have taught me. I am especially indebted to Andrew Frankenburg, much missed, and to Irena Borzym. I am who I am thanks to Derby friends, Cambridge friends, and Scouting, and the last three years have been a pleasure, thanks largely to Catz MCR, the Hillwalkers, and all at no. 29. In particular, I am outstandingly fortunate to be facing the future with the woman I love, without whom the last month's work would not have been possible. Aš tave myliu, Ieva, je t'aime.

---

[a] Thanks for letting me finish first, Chris!

Chapter 1

Introduction

The study of avalanching on dunes is a clear example of the benefits of interdisciplinarity. In a variety of different fields, researchers have studied a variety of related problems, from the fundamental behaviour of the sand avalanches that occur on dunes to the properties of avalanche-emplaced heterogeneities within them, and to the effects of heterogeneities on the propagation of acoustic waves. Drawing links between these different problems, even where such links appear tenuous, can lead to the formulation of new hypotheses and to more accurate modelling. With this in mind, I consider a range of problems connected to aeolian dunes and to the avalanches upon them.

Aeolian sand dunes are a remarkable natural phenomenon, consisting of millions of tonnes of sand and yet crossing countries in the geological blink of an eye. On fully-developed dunes, the mechanisms for this migration are the transportation of sand grains up one face of each dune, by the wind, and the avalanching of such grains down the opposite face, under gravity.

This avalanching is associated with the fundamental properties of granular matter, which grant materials such as sand an array of rich and complex behaviour. On a more practical level, avalanches on sand dunes are analogous to those of agricultural grains, to rockfalls on scree slopes, and to certain processes in the production of pharmaceuticals. In many of these applications, it is important to know the probabilities of avalanches having certain sizes.

On dunes themselves, such probability distributions of avalanche size determine the form of layers that are emplaced within each dune during its migration. Each layer, referred to as a ‘stratum’, is a consequence of the spontaneous separation (‘segregation’) of differently-sized grains within each avalanche. The strata that were emplaced by avalanches on ancient dunes are preserved in certain sandstones and are a key tool in interpreting the ancient climates in which the dunes were formed. Meanwhile, those emplaced on active dunes guide the permeation of water within each dune.

The presence of such water is essential to permanently stopping deleterious dune migration, whether via revegetation or by bacterial action. Furthermore, it has an important influence on the propagation of sound waves within the dune.

Since differences in sound propagation affect exploratory seismic surveys for oil or gas, the results of near-dune seismic surveys depend on the pattern of water within the dune, which depends in turn on stratification during the dune's migration, which depends at last on the size statistics of avalanching on dunes.

In this dissertation, I discuss these four problems: avalanching on the surface of dunes, stratum-emplacement at this surface, water permeation within dunes, and dunes' effects on seismic surveys. In chapter 2, I experimentally investigate discrete avalanches on the surface of a grain pile, as occur on desert sand dunes. Motivated by my results, I examine in chapter 3 the widths of the strata emplaced by such avalanches. Chapter 4 describes fieldwork conducted on active dunes in the Qatari desert, identifying such strata and associating them with the permeation of water within dunes. In chapter 5, I numerically simulate the effect on seismic surveys of sand dunes and of the water that has permeated within them. Finally, I summarise my conclusions in chapter 6. Appendices A, B, C, and D contain material supplementary to chapters 2, 3, 4, and 5, respectively, while Appendix E describes technical difficulties encountered during my doctoral studies, so that they may be avoided in any future work.

Given the disparate motivations, backgrounds, and methodologies for these pieces of work, each chapter contains an abstract, an introduction, a description of methodology, a discussion of results, and recommendations for further work on the topic. I confine myself here to providing an introduction to granular avalanches and to aeolian sand dunes.

1.1 Granular avalanches

1.1.1 Solid-like and fluid-like behaviour

Granular matter is at once both familiar and exotic. Examples surround us in our everyday experience, from grains of rice to steel ball bearings, and granules are processed in industries from copper-mining [246] to cup-making [244]. Yet the behaviour of granular materials is often counterintuitive, even under familiar conditions[a]. The volume of space that they inhabit changes during and following disturbances, without changes in temperature, pressure, or chemical composition [252, 265]. Furthermore, an apparently homogeneous and isotropic collection of grains can impose loads at its base quite different from its overlying weight, as demonstrated by Janssen's observations of pressure saturation at the base of a grain-filled hopper [170] and by a central decrease in load at a conical, poured sandpile's base, as described by Smid and Novosad [272] and Jotaki and Moriyama [174]. Finally, when subjected to disturbance, a mixture of differerently-sized grains can spontaneously separate, with larger particles rising even in some cases in which they are more dense [56, 126].

Underlying these exotic phenomena is the ability of granular systems to display both solid-like and fluid-like behaviour. Grains are athermal and their collisions are highly dissipative, so that an undriven granular system quickly adopts a state corresponding to a local minimum of its energy landscape. In this solid-like state, grains have few degrees of freedom (if any), and are able to support certain 'compatible' external stresses. However, when the system is disturbed or its conditions changed in an incompatible manner, grains are able to rearrange themselves in a fluid-like fashion, increasing their number of degrees of freedom and moving over one another as the system adopts a new energy-minimising state which may be very different from the previous one.

The combination of fluid-like and solid-like behaviour is typified by the case of avalanches on piles of grains. A pile consists of static grains in a solid-like state, supporting their own weight with non-zero slope angle. On its surface, however, grains are able to flow. Such flowing grains dissipate energy through interparticle collisions, but remain in a fluid-like state as long as the slope angle is sufficient for gravity to balance friction. The difficulty of modelling

---

[a] I take familiar conditions to imply systems of large numbers of grains that are sufficiently large for thermal fluctuations to be negligible, undergoing dissipative collisions under gravity, and henceforth I consider only such systems.

avalanching arises from capturing the transitions between solid-like and fluid-like behaviour.

1.1.2 Modelling the solid-like pile

Continuum models for solid-like behaviour exist, but struggle to predict the time or position at which a pile yields and transitions to fluid-like behaviour.

On the basis that the contacts between grains are elastic, the simplest approach is to assume a yield stress and to model the entire pile as an elastic medium. This may be valid when considering small increments in stress [199], but is problematic when considering the net stress within the pile [63], for reasons both practical and theoretical. In practice, if grains' elastic moduli are high then strain within the pile will be immeasurably small, while if moduli are low then grain deformation results in changes in the contact network, making the stress-strain relation incalculable. On a theoretical level, strain can be defined only in reference to an unstressed state and such a state is unphysical for uncohesive granular materials.

To avoid the definition of a reference state, another approach is to calculate stress within a pile by assuming that a relation between stress components holds everywhere within it. Geotechnical engineers use, among others, Mohr's generalisation [233] of the Coulomb failure condition [78] and Schofield and Wroth's Granta Gravel and Cam Clay models [265], but these originated as conditions for yield to occur and so to assume their validity throughout the pile is to exclude their use in predicting yield. The 'fixed principal axes' relation of Bouchaud et al. [39, 63–66, 73, 308, 309] instead supposes that i) the principal axes of the stress tensor are aligned normal to the pile's surface and down it wherever grains are emplaced and ii) these principal axes do not change unless the external stress becomes incompatible with the pile's structure. Whilst this relation is successful in describing static cases, where stress propagates along long-lived 'force chains' [130, 131, 289, 320], one of its fundamental properties is that it predicts yield everywhere whenever external conditions do not match those of the pile's construction, and so it cannot be used to predict the time or position at which a nonideal pile yields.

That these deterministic, continuum models fail to predict yield points indicates the importance of random, grain-scale properties. Failure occurs locally and depends on the local arrangements of individual grains. This is fundamentally linked to the appearance of fluid-like behaviour, for which locality is the first principle of modelling.

1.1.3 Modelling the fluid-like avalanche

Among local constitutive relations for dense flows of grains, a consensus has formed in support of the '$\mu(I)$' model [129, 173]. Its central principle is that, within a dense flow of hard spheres of density ρ and diameter d, the only local, non-dimensional kinematic parameter is the inertial number I, equal to the ratio of two timescales: $\tau_p = d\sqrt{(\rho/p)}$, over which grains relax towards each other under a confining pressure p, and $\tau_{\dot{\gamma}} = 1/\dot{\gamma}$, over which grains move over one another under shear rate $\dot{\gamma}$. The local volume fraction ϕ and local internal friction angle μ are then expected to be functions of I.

However, the $\mu(I)$ model fails as grains come to a rest and $I \to 0$. Barker et al. have shown that empirically-derived functions for μ and ϕ lead to partial differential equations that are ill-posed for small I, with strain concentrated in shear bands of infinitesimal width [28]. Furthermore, such ill-posedness is avoided only if $\mu \to 0$ as $I \to 0$, which implies that grains coming to a rest experience no resistance to motion [29]. This is clearly unphysical.

To describe the low-I behaviour uncaptured by the $\mu(I)$ model, a number of groups have introduced 'non-locality', in the form of a scalar field describing the extent to which behaviour is fluid-like. In 'partial fluidisation theory', Aranson et al. [15–17, 292] used an order parameter that evolves by a Ginzburg-Landau equation and corresponds to the proportion of particle contacts that are long-lived. Kamrin and Koval [177] instead developed a previous 'kinetic elastoplastic' theory for emulsions [36] to define a 'granular fluidity' $g = \dot{\gamma}/\mu$. Taking g_{loc} to be the value predicted for g by the $\mu(I)$ model and l to be some typical cooperation length, they assumed $g = \left(1 - l^2\nabla^2\right)^{-1} g_{\mathrm{loc}}$. In contrast, motivated by parsimony, Bouzid et al. [45–47] use I as a proxy for fluidity and suppose that the internal friction angle $\mu = \mu_{\mathrm{loc}}(I)(I - l^2\nabla^2 I)/I$ for a given function $\mu_{\mathrm{loc}}(I)$. These different models capture much of the low-I behaviour of fluid-like granular matter, but sufficient experimentation has not yet been performed to distinguish them. Furthermore, the latter two models do not capture the changes in fluidity over time that are essential to avalanching.

Due to the difficulty of describing these changes in fluidity, a class of models elides the details of solid-like/fluid-like transitions. Instead, they consider only the erosion of grains from a solid-like pile by a fluid-like avalanche and the deposition of grains from the latter onto the former.

1.1.4 Erosion-deposition models

Whilst erosion and deposition by avalanches have long been investigated by the geophysical community (as reviewed by Iverson [165, 166]), the paradigmatic model for these processes dates to 1994 and is referred to as the BCRE model [40, 41]. The model consists of partial differential equations for the height h of a sandpile and the density R of rolling grains upon it, with R advected downslope at a constant speed v and subject to diffusive dispersion. The relation between the solid-like sandpile and the fluid-like rolling grains is captured by an erosion rate $\mathit{\Gamma}$, increasing R at the expense of h. In the BCRE model, $\mathit{\Gamma}$ is taken to be proportional to R and to have additive contributions from diffusive dispersion and from excesses in slope angle above the repose angle θ_r, but subsequent modifications considered a range of forms of $\mathit{\Gamma}$ [14, 44, 219]. In all these cases, the central principle is the conservation of depth-averaged mass.

Later work added to this condition the conservation of depth-averaged momentum, in order to specify the depth-averaged velocity v at which rolling grains move downslope. The relevant system of depth-averaged equations was stated by Saint-Venant [260] and applied for non-erosive avalanches by Savage and Hutter [262], but it was Douady et al. [92] who generalised the equations to allow for erosion and deposition. Douady et al. closed the generalised system of equations by assuming a linear velocity profile, showing that in this case terms cancel so that equations of BCRE-form can be recovered. If a different velocity profile is assumed, or none is, then other closures are required. Most geophysicists have specified erosion rates, as summarised by Iverson [166], whilst Bouchut et al. and Capart et al. [42, 60] chose to introduce kinetic energy balances. Gray et al. [100, 101] avoided the problem by considering a shallow pile, ignoring the interface between static and flowing grains, and using a Froude number condition to distinguish solid-like and fluid-like regions.

On a deep sandpile, such as a dune, the distinction between solid-like and fluid-like regions cannot be avoided, whilst the small differences in the angle of the slope make the system sensitive to the exact erosion condition. Furthermore, depth-averaged models are derived in the limit of gradual variation in flow properties, making them unsuited to modelling the sharp fronts of avalanches. Consequently, the validity of erosion-deposition models is unclear in the case of avalanching on dunes.

1.2 Aeolian sand dunes

The systematic study of aeolian sand dunes originates in the work of Ralph Alger Bagnold, much of it published in 'The Physics of Blown Sand and Desert Dunes' [22], which provides an introduction to the field that is difficult to surpass. My own introduction shall therefore be very brief.

On land, sand is transported through the action of the wind. Under the stress imposed by this wind, individual grains may be displaced from the desert floor, gaining momentum from the wind while exposed to it. Consequently, they collide with and displace other grains, increasing the number of grains in motion over a saturation length L_S, until grains' reaction forces sufficiently diminish windspeed for sand transport to be steady[b] [22, 267]. In this steady state, a vanishingly small number of grains are in suspension, the desert floor having been denuded of those grains sufficiently small to be suspended [22, 230]. A significant volume undergo saltation: having been displaced from the desert floor to a height of order centimetres and accelerated by the wind in its direction of travel, they follow extended aerial trajectories [22, 97]. Other grains reptate, following short trajectories of heights comparable to the grains' diameters, as a result of bombardment by saltating grains [22, 286]. The flux of grains transported in this manner depends on the grains' sizes as well as on windspeed, so that different windspeeds transport grains with a different distribution of sizes [22, 211]. Clearly, the size distribution of grains arriving at a given location also depends on the direction of sand transport and therefore on the wind's direction.

When that arrival location has a surface of loose sand, the pattern of grains' trajectories leads to the formation of aeolian ripples. If the topography of the sand's surface has a wavelength corresponding to the typical length of saltation trajectories, grains ejected into saltation from one upwind slope will tend to impact upon the next, so that multiple grains reptate towards and across the slope's peak and an average of one grain is ejected into saltation to continue the process [22, 98] [c]. Consequently, ripples grow and migrate downwind.

On a larger scale, dunes arise through the effect of topography on windspeed and that of windspeed on aeolian transport. As wind flows up a topographic rise, the compression

---

[b] This increase is not necessarily monotonic, with both Bagnold [22] and Selmani et al. [267] observing 'overshoot' of sand flux in certain conditions.

[c] Bagnold proposed this mechanism with little evidence, resulting in it being disputed by Anderson [12] on theoretical grounds. Numerical simulations by Durán et al. [98] provide it with strong support.

of streamlines results in an increase in windspeed, increasing the rate of transport of sand [67, 168, 302]. Provided the width of the rise is greater than the saturation length L_S, so that sand transport adjusts to the increase in windspeed before the crest is reached, grains are transported towards and across the crest. As a result, the topographical perturbation is amplified, becoming a growing dune which migrates downwind [67, 201]. When the dune is sufficiently large, flow separates downwind of its crest, resulting in a rapid decrease of sand flux [22, 302]. This steepens the dune's leeward face, forming a slip face down which grains will avalanche [238, 242, 279].

Whilst the process of dune growth and slip face formation is common to all dunes, their morphology is diverse. In a predominantly unidirectional wind environment with a low sand supply, dunes are isolated and have a single slip face. The only relevant lengthscale is L_S, so that they adopt approximately identical, crescentic shapes and are referred to as barchans [22, 67, 113, 154, 200]. Dunes rarely migrate in a steady state, since there is no requirement for the incoming flux of sand to match the outgoing flux, but change shape quickly and size slowly in response to changes in inflow conditions [114, 181]. If sand supply is high and predominantly unidirectional then long, sinuous slip faces are formed transverse to the wind, whilst if the wind comes from two directions then dunes are longitudinal, with slip faces corresponding to each wind direction[d]. Finally, those dunes that form in multidirectional wind environments are referred to as star dunes [22, 157, 230], with multiple slip faces.

Of these multiple dune forms, barchans are attractive due to their simple history of formation and the possibility of considering them in isolation. In the following I will assume a barchan morphology by default, though many of my results are equally applicable to other forms of dune.

---

[d] These are also referred to as linear dunes or seif/saif/sayf dunes, from Arabic 'sword'.

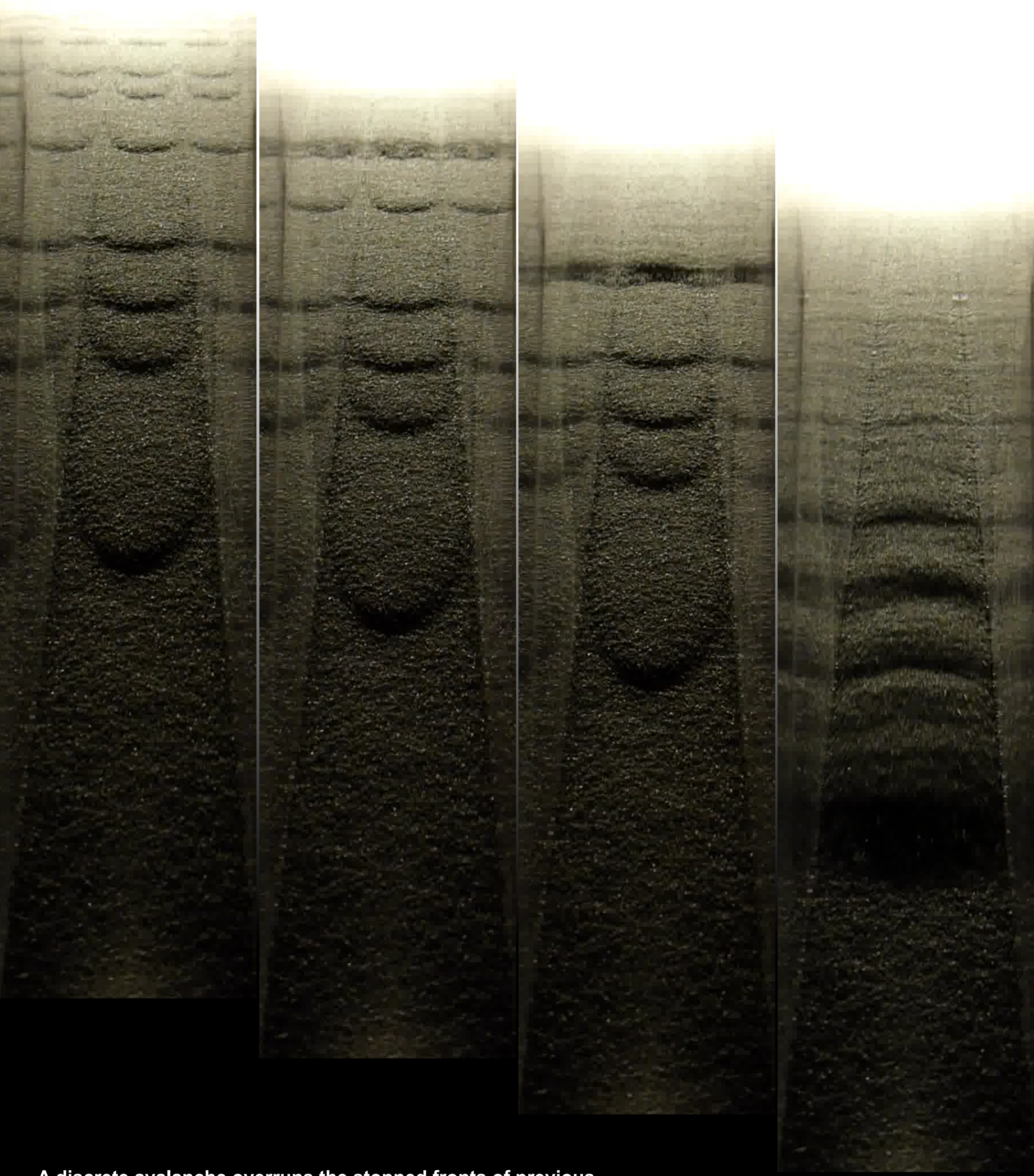

A discrete avalanche overruns the stopped fronts of previous avalanches and mobilises the static grains.
Frames are captured at intervals of 3.0, 1.2 and 3.4 s, using a Panasonic DMC-TZ40 camera, fixed to the bottom of a top-lit channel, 2.5 m long, 5 cm wide, inclined at 32º, and filled to a depth of 11 cm with angular construction sand. Images are rotated, cropped, and brightened, with reflections visible on the channel's sidewalls.

Chapter 2

Intermittency between avalanche regimes on grain piles

> *'Perhaps by staring at the sand as sand, words as words, we can come close to understanding how and to what extent the world that has been ground down and eroded can still find in sand a foundation and model.'*
>
> Italo Calvino, *Collection of Sand*

This chapter is substantially derived from a manuscript published as a Rapid Communication in Physical Review E 97, 5th June 2018, under the same title and with the authors Matthew I. Arran and Nathalie M. Vriend. DOI: 10.1103/PhysRevE.97.060901.

Abstract

I experimentally investigate discrete avalanches of grains, driven by a low inflow rate, on an erodible pile in a channel. I observe intermittency between one regime, in which avalanches are quasi-periodic and system-spanning, and another, in which they pass at irregular intervals and have a power-law size distribution. Observations are robust to changes of inflow rate and grain type, and require no tuning of external parameters. I demonstrate that the state of the pile's surface determines whether avalanche fronts propagate to the end of the channel or stop partway down, and I introduce a toy model for the latter case that reproduces the observed power-law size distribution. I suggest direct applications to avalanches of pharmaceutical and geophysical grains, and the possibility of reconciling the 'self-organised criticality' predicted by several authors with the hysteretic behaviour described by others.

2.1 Introduction

Discrete avalanches on the surface of grain piles appear in contexts as diverse as desert sand dunes [22, 279] and agricultural corn silos [54, 110, 182]. The size distributions of such avalanches are significant in a number of these contexts, controlling the assessed 'flowability' of pharmaceutical grains [206], and determining the hazard posed by rock falls above talus slopes [218].

The topic has attracted interest from the wider physics community as a result of Bak, Tang, and Wiesenfeld's 'sandpile' model, an n-dimensional cellular automaton that introduced the concept of 'self-organised criticality' [24, 25, 176]. At each step of the automaton, an integer z, representing local slope, is incremented by one at a randomly-selected site, representing the addition of grains to a pile. For some constant K, an avalanche starts at site $\boldsymbol{x}_a$ when

$$z(\boldsymbol{x}_a) > K. \tag{2.1}$$

The avalanche is represented by the map $z(\boldsymbol{x}_a) \to z(\boldsymbol{x}_a) - 2n$, $z(\boldsymbol{x}) \to z(\boldsymbol{x}) + 1$ for $||\boldsymbol{x} - \boldsymbol{x_a}|| = 1$, iterated until no sites satisfy (2.1), at which point the avalanche is deemed to stop. The size of the avalanche is defined to be the number of sites that, at some time, satisfied (2.1). In Bak, Tang, and Wiesenfeld's simulations of this automaton, the system self-organises over time into a state in which the size of the subsequent avalanche is sensitive to the exact function $z(\boldsymbol{x})$, with the probability of an avalanche having size s decaying as s^{-1}. Without tuning of external parameters, a locally-hysteretic system with only short-range interactions displays scale-invariant spatio-temporal correlations between fluctuations.

This concept has been invoked in areas from solar flares [20] through forest fires [94] to neuron firing [69], but conditions for its applicability remain unclear [122, 143, 296]. Watkins et al. [296] sought to clarify the concept, hypothesising that three conditions should be satisfied for a system to display the behaviour referred to as self-organised criticality: a locally non-linear response to forcing; 'avalanching', as local interactions spread this response through space; and a separation of timescales between the slow forcing and the fast avalanching.

These conditions appear to be satisfied on grain piles subject to the slow addition of grains, where the yield condition discussed in chapter 1 is non-linear; literal avalanches can occur; and the time interval between avalanches is much longer than the duration of each avalanche. On such grain piles, the 'sandpile' model predicts a power-law distribution of avalanche sizes, as observed for grains of specific varieties of rice in a channel [121], and for grain rearrangements on an inclined plane, long before avalanching [48, 85].

However, most authors have instead reported quasi-periodic, system-spanning avalanches, either in rotating drums [61, 106, 107, 169] or on the surface of a short pile [121, 169, 207][a]. These authors used a variety of methods to detect avalanches: sound emissions during flow [106, 107]; changes in capacitance at the point of outflow [169]; changes in the basal contact position [61]; optical scattering from the avalanches' surfaces [207]; and imaging of the pile through sidewalls [121]. All recorded that avalanches propagated the entire length of their systems, with the time intervals between avalanches having a narrow distribution.

Such authors, reporting quasi-periodic avalanches, explain the limited applicability of the 'sandpile' model to physical piles of grains by the model's omission of inertial effects, with the model's avalanches stopping as soon as the condition for their initiation is no longer satisfied. Physical avalanches are inertial, so that, under the addition of grains, a static grain pile is metastable whenever its slope is between an angle of repose θ_r, at which any avalanche will stop, and a maximum slope angle θ_m, at which any disturbance initiates an avalanche [81, 187, 248]. The associated hysteresis between static and flowing grains is associated with a time interval between avalanches, during which the top of the pile steepens from θ_r to θ_m. Approaching θ_m, the pile yields and an avalanche propagates downslope, leaving behind it a slope at θ_r on which future avalanches will likewise continue to propagate. This physical description explains the quasi-periodic, system-spanning avalanches hitherto observed, and the matter has been considered settled.

In this chapter, I report entirely new behaviour: without tuning of external parameters, a grain pile in a long channel exhibits intermittency between two regimes. In one regime, avalanches are quasi-periodic and system-spanning, as previously reported. In the other, the time intervals between avalanches are irregular and most avalanches stop partway down the channel, with the frequency distribution of their lengths satisfying a power-law. I successfully reproduce behaviour in this new regime with a toy model, in which the power-law size distribution arises from interactions between each avalanche and the stopped fronts of previous avalanches. I show furthermore that the existence of the two regimes, and of the spontaneous transitions between them, can be qualitatively described by a reduced dynamical system. My experiments involve

---

[a] Vidar et al. [121] observe a power-law distribution of avalanche sizes for certain varieties of rice and observe system-spanning avalanches for others.

inertial avalanches of $O(10^6)$ grains, and my observations are robust to changes of inflow rate and of grain type, demonstrating their relevance to a variety of grain piles.

2.2 Methods and Results

For my experiments, I first use angular construction sand with mean particle diameter $\bar{d} = 0.47$ mm, standard deviation in particle diameter 0.10 mm, and angle of repose $\theta_r = 32°$. An $L = 2.5$ m long channel of width $W = 5$ cm is inclined at θ_r, as depicted in Fig. 2.1. Grains flow into the channel via a nozzle at its top, while its bottom is partially closed by an inclined plate, establishing an 11 cm deep pile of static grains at their angle of repose. I then permit further grains to flow through the nozzle with constant flux $Q = 3.05$ cm^{3}s^{-1}. This is sufficiently small that the pile increases in height slowly and locally at the channel's top before losing stability, so that discrete avalanches flow along the channel on the surface of the pile, with a quiescent interval between each avalanche and the next. Footage of avalanching is available online [19].

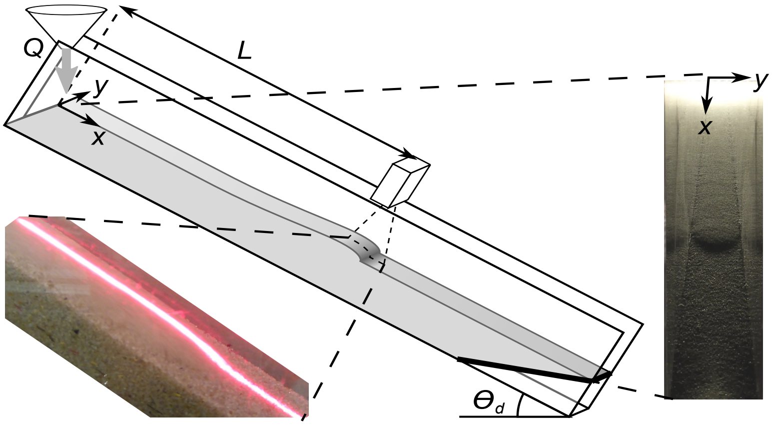

Figure 2.1: Schematic of experimental apparatus. The channel is smooth-walled and has a base roughened with sandpaper. Inset, right, is an image of an avalanche propagating down the channel on the surface of the grain pile, while inset, left, is an image of such an avalanche's front in the field of view of a laser profile scanner.

In each experiment, a Micro-Epsilon scanCONTROL 2800-100 laser profile scanner measures surface height along a section of the channel's centreline, at a fixed distance X downslope. From these height profiles, I may distinguish the times at which avalanches pass the scanner.

While maintaining identical inflow conditions, I observe alternation between two regimes: one in which avalanches pass the scanner quasi-periodically (henceforth 'the quasi-periodic regime') and another in which the intervals between avalanches are irregular (henceforth 'the irregular regime'). An example of this alternation is depicted in Fig. 2.2.

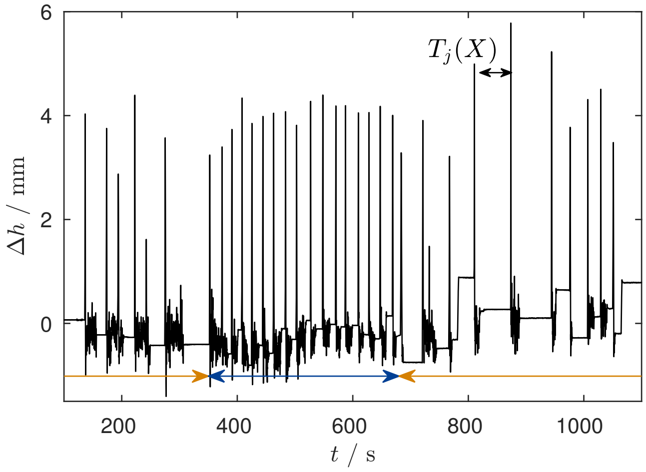

Figure 2.2: Alternation between quasi-periodic and irregular regimes. When fixed a distance X downslope, the scanner measures surface heights $h(x_i)$ at distances x_i downslope, with X the midpoint of x_i. I calculate $\Delta h = \langle h(x_i) \rangle_{x_i<X} - \langle h(x_i) \rangle_{x_i>X}$. Over time t, each avalanche front passing the scanner is associated with a peak in Δh. At a distance $X = 0.34L = 844$ mm downslope, avalanches pass quasi-periodically between times $t = 350$ s and $t = 680$ s (marked in blue), while at earlier and later times the intervals between avalanches $T_j(X)$ are irregular (marked in orange).

Since all avalanches propagate from the channel's top, the avalanches passing the scanner are those with a length greater than X. I measure the time intervals between such avalanches using the data processing described in Appendix A, section A.1, classify in the quasi-periodic regime any 12 consecutive intervals with a standard deviation less than 20% of their mean, and classify in the irregular regime any intervals that are not in a consecutive set of 6 with a standard deviation less than 20% of their mean. For each regime, I calculate the mean of the intervals in that regime, $\bar{T}(X)$. Supposing an avalanche to involve some minimum number of grains, I expect this mean interval to scale with $\bar{d}^3/Q$.

To find the size distribution of avalanches in each regime, I change the position of the scanner, varying X. I observe that in the quasi-periodic regime $\bar{T}$ remains constant (Fig. 2.3, $R^2 = 0.011$, p-value for rejection 0.5, as described in Appendix A, section A.3). This indicates that each avalanche propagates the entire length of the channel and flows out over the inclined plate at its end, in accord with the reports of Ref.s [61, 106, 107, 121, 169, 207] and corresponding to the hysteresis between static and flowing grains that they and I have described. In the irregular regime, however, $\bar{T}$ increases linearly with X ($R^2 = 0.94$, p-value for rejection 0.59). The frequency of avalanches which have a length greater than X therefore decays as X^{-1}, and hence the probability density of an avalanche being of length X decays as X^{-2}.

I repeat these experiments with a smaller inflow nozzle, decreasing the flow rate Q by a factor of more than 3, to 0.9 cm^3s^{-1}. Scaling times $\bar{T}$ by Q, I observe excellent collapse, indicating a separation of timescales between the slow forcing, via input of gravitational potential energy, and the fast avalanching. This demonstrates that my experiments are in the low-Q limit that is relevant to many physical situations and is a precondition for the applicability of self-organised criticality. Since my system also features both non-linear interactions and avalanching, and the observed power-law decay is among self-organised criticality's hallmarks [122, 143, 296], it is reasonable to compare my results to others for which the existence of self-organised criticality is claimed.

I seek to explain the size distribution of avalanches in the irregular regime, in which most avalanches stop after propagating only a short distance. In this regime, if an avalanche propagates sufficiently far down the channel to overrun the stopped front of a previous avalanche, it mobilises the static grains, resulting in a larger avalanche that is able to propagate further. To model this process, I first assume that avalanching is instantaneous in comparison to the intervals of time $T_i(0)$ between one avalanche and the next, which I take to be independent and identically distributed, with mean τ. I then make the simplifying assumptions that stopped avalanche fronts are of equal height H, and that each front leaves behind it a slope at the angle of repose. In the absence of stopped avalanche fronts, the ith avalanche would therefore propagate a distance $x_i^0 = QT_i(0)/HW$. Furthermore, each stopped avalanche will, if its front is overrun, add its own length to the final length of the overrunning avalanche. I may write the process algorithmically, with at each time the distances downslope of stopped avalanche fronts denoted by the increasing sequence $S = (s_1, s_2, ..., s_n)$. Iterating over avalanche number i:

1) Initialise avalanche length $x_i \mapsto x_i^0$ (the slope yields, mobilizing a given volume of grains)
2) While $x_i \geq s_1$ (the avalanche is able to overrun the first stopped avalanche front), $S \mapsto (s_2, s_3, ..., s_n)$ and $x_i \mapsto x_i + s_1$ (the stopped avalanche is mobilised, adding its

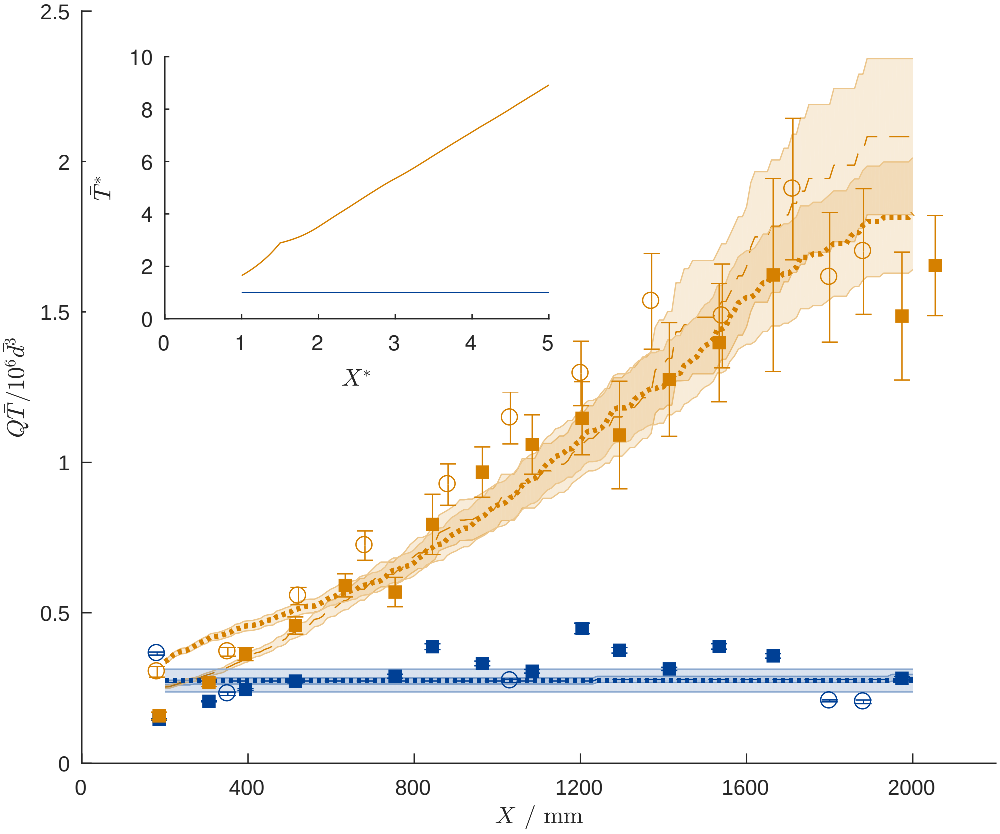

Figure 2.3: Hysteretic and power-law behaviour in the quasi-periodic (blue) and irregular (orange) regimes. I conduct experiments with continuous fluxes $Q = 0.9$ (○) and 3.05 (▪) cm^3 s^{-1} of sand ($\bar{d} = 0.47$ mm), as well as with interrupted inflows of the same sand (- -) and of glass beads (···, $\bar{d} = 0.22$ mm). Error bars and shaded regions represent the standard errors of the means over observed avalanches. For $X > 2000$ mm, the effect of the channel's end is significant. Raw data is in Appendix A, section A.2. I model the quasi-periodic regime with the assumption that all avalanches propagate to the end of the channel, while an overrunning-mobilisation model reproduces the behaviour observed in the irregular regime (inset).

length to that of the overrunning avalanche).

3) Once $S = \varnothing$ or $x_i < s_1$ (no stopped front can be overrun), $S \mapsto (x_i, S)$ (the avalanche stops a distance x_i downslope).

Simulating this process numerically, with $\tau = H = W = Q = 1$ and with the distribution of $T_i(0)$ taken in turn to be uniform, lognormal and exponential, I find that this model system reproduces the linear increase with X of $\bar{T}(X)$ (see inset, Fig. 2.3, for which time intervals

$T_i(0)$ are drawn from a uniform distribution between 0.5 and 1.5). The asymptotic behaviour of $\bar{T}$ at high X is insensitive to the distribution of $T_i(0)$.

To determine the relevance of this overrunning-mobilisation model, I repeat the above experiments, but now halt inflow upon the start of each avalanche. After the avalanche has come to a stop, surface height is measured over the entirety of the channel's centreline, and the position of the stopped avalanche front is detected from this full-length height profile (details of detection are described in Appendix A, section A.1). Inflow is then resumed and the time interval until the start of the next avalanche recorded, with this process repeated over 400 avalanches. As no grains flow into the channel during each avalanche, this procedure is equivalent to conducting experiments with an infinite separation of timescales, and I observe in Fig. 2.3 the same behaviour of $\bar{T}$ as in the original experiments.

The new data support the relevance of the overrunning-mobilisation model. Considering the interaction of flowing avalanches with stopped avalanche fronts, I observe in Fig. 2.4 the same qualitative behaviour in experiments as is predicted by the model. However, in experiments, the exact position at which an avalanche stops is sensitive to the state of the static pile over which it propagates, as demonstrated by the early cessation of the avalanches depicted in Fig. 2.4a at $t = 111$ s and $t = 123$ s. This sensitivity prevents me from accurately predicting, at this time, which stopped avalanche fronts will be overrun by a given avalanche, and hence from accurately predicting the final length of individual avalanches (unsuccessful attempts are described in Appendix E, section E.1).

Instead, I calculate the correlation between observed avalanche lengths and the lengths predicted by the overrunning-mobilisation model, over a large number of avalanches. I consider the last 200 avalanches in the irregular regime, for which my measurements of the time intervals between avalanches are most precise, and for each of the preceding 10 avalanches calculate a value H_i equal to the mean increase in surface height in the wake of the avalanche's stopped front, with respect to the last prior height profile with no stopped avalanche fronts in the corresponding region. To predict avalanche lengths, I take H to be the median of the measured values H_i, I use the measured values of Q and W, and I input to the overrunning-mobilisation model the positions of stopped avalanche fronts prior to each avalanche and the time interval $T_i(0)$ before each avalanche. Pearson's correlation coefficient between my predictions and my observations is 0.45. While this value indicates that effects other than overrunning and mobilisation are important, the correlation is highly significant; the probability of such correlation would be $p = 10^{-11}$ if avalanche lengths were randomly sampled from the distribution of their lengths.

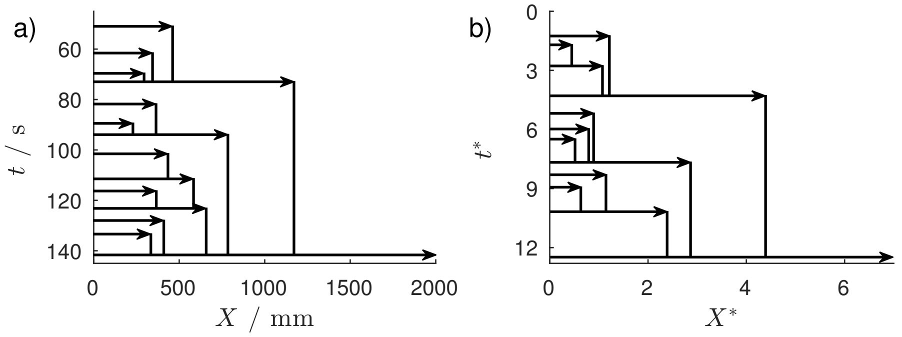

Figure 2.4: Comparison of experimentally observed avalanche-front interactions (a) with realisations of the overrunning-mobilisation model (b). Avalanches paths as observed in experiments (a) and simulations (b) appear as horizontal arrows down the channel, while stopped avalanche fronts appear as vertical lines with constant X. In panel b I use a log-normal distribution of nondimensionalised intervals between avalanches, with mean 1 and standard deviation 1/2.

Having described behaviour in each of the two regimes, I use the full-length height profiles to analyse the intermittency between them. I consider the state of the static grain pile after each avalanche that propagates to the end of the channel, which I refer to as a ‘zero-front state’. In particular, I consider two statistics: the average slope angle $\bar{\theta}$, as determined by the gradient of the least-squares line of best fit to each full-length height profile; and the variance σ^2 of residuals from that line of best fit. The higher the slope variability σ^2, the more regions of shallow local slope the subsequent avalanche will have to pass over, making it more likely to stop. The higher the value of $\bar{\theta}$, the more potential energy will be available to the subsequent avalanche, making it more likely to overcome those regions and hence less likely to stop.

In Fig. 2.5, a trajectory in the $\sigma^2 - \bar{\theta}$ plane elucidates the mechanism for intermittency. σ^2 is low in zero-front states subsequent to quasi-periodic, system-spanning avalanches, making the subsequent avalanche unlikely to stop, and maintaining the system in the same regime. However, such avalanches cause net erosion of grains at the channel’s top, decreasing $\bar{\theta}$ over time. At some point an avalanche will have insufficient potential energy to overcome even minor regions of shallow local slope, stopping partway down the slope, and forcing the system into the irregular regime, despite the value of σ^2. In zero-front states subsequent to irregular avalanches, σ^2 is high, so that most avalanches continue to stop partway down the slope even after each of the rare avalanches that propagate to the end of the channel. However, the erosion and deposition of grains are highly sensitive to the details of stopped avalanche fronts' emplacement and mobilisation, resulting in large changes in both σ^2 and $\bar{\theta}$ over consecutive zero-front states. At some point, the subsequent avalanche has sufficient available potential energy to propagate to the channel's end, forcing the regime into the quasi-periodic regime.

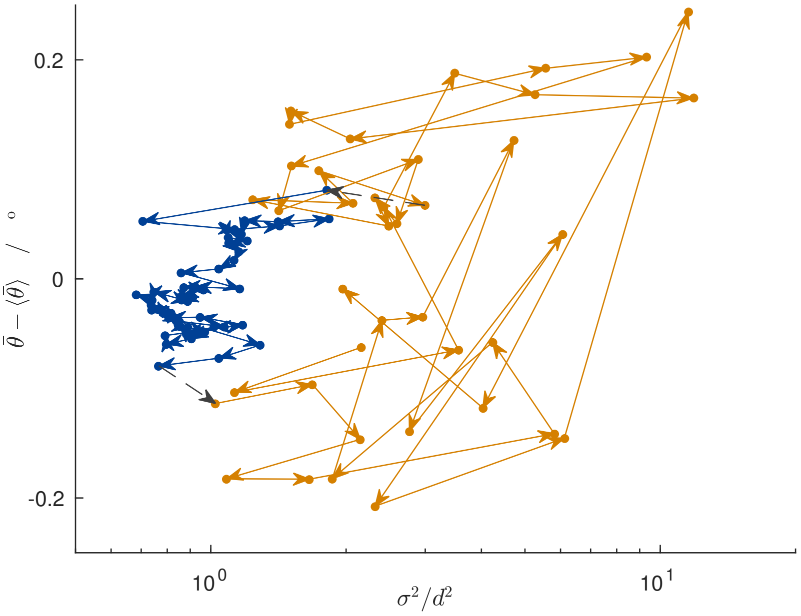

Figure 2.5: System evolution, in the $\sigma^2 - \bar{\theta}$ plane, over one cycle between regimes. The slope variability σ^2 remains low while the system is quasi-periodic (blue) and high while it is irregular (orange), maintaining each regime. The average slope angle $\bar{\theta}$, meanwhile, provides the stimulus for changes of regime, varying chaotically in the irregular regime and recovering gradually in the quasi-periodic regime.

Figure 2.6 provides further evidence for this mechanism, demonstrating the change in surface height at the top of the channel, a proxy for $\bar{\theta}$, over the course of over 2000 avalanches. Furthermore, changing $\bar{\theta}$ directly in the course of an experiment, by raising or lowering the entire channel's inclination by as little as 0.1°, forces the system from the irregular regime to the quasi-periodic regime, or vice versa. Directly increasing σ^2, by lightly brushing the surface of the grain pile, forces the system from the quasi-periodic regime to the irregular regime.

To verify the applicability of these results to other types of grains, I replace sand in my experiments with an inflow flux $Q = 1.22\ \mathrm{cm}^3\ \mathrm{s}^{-1}$ of spherical glass beads, halted during each avalanche. Previous authors have shown avalanches of such grains to be substantially different from those of sand [38, 280]. The glass beads have mean particle diameter $\bar{d} = 0.22$ mm, standard deviation in particle diameter 0.07 mm, and angle of repose $\theta_r = 25°$. Avalanches

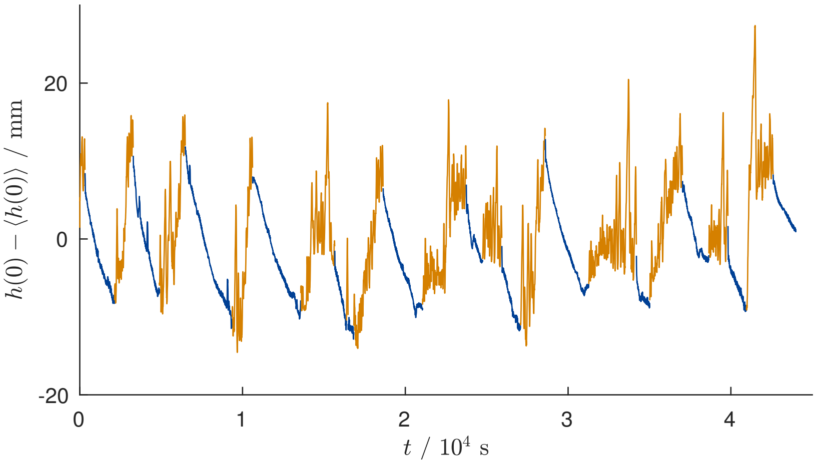

Figure 2.6: Evolution of $h(0)$, a proxy for $\bar{\theta}$, over multiple cycles between regimes. Surface height at the top of the channel $h(0)$, smoothed over individual avalanches, is approximately proportional to $\bar{\theta}$. $h(0)$ varies chaotically in the irregular regime (orange) and recovers gradually in the quasi-periodic regime (blue).

are shallower, at any time the extent of moving grains is shorter, and erosion by each avalanche in the quasi-periodic regime is significantly greater. Despite these differences, I observe the same behaviour as described above, with intermittency between one regime of quasi-periodic, system-spanning avalanches and another regime of irregular avalanches that can both stop, and overrun and mobilise existing stopped fronts. The duration of each instance of the quasi-periodic regime is reduced to 2-3 avalanches, but behaviour in this regime remains clearly distinct from that in the irregular regime, as is shown in Fig. 2.3. In the irregular regime, the correlation between the avalanche lengths predicted by the overrunning mobilisation mechanism and the observed avalanche lengths, using a value of H calculated from 10 previous avalanches, is 0.20 ($p = 10^{-14}$ under the assumption that avalanche lengths are random, sampled from their observed distribution).

2.3 Discussion

The similarity of the system's behaviour, despite different properties on the grain and avalanche scales, indicates the applicability of this work to a variety of granular systems. The measured flowability of pharmaceutical granules will differ depending in which of the two regimes the measurement system is in, while alternation between regimes will affect the cross-bedding of sedimentary rocks laid down by surface avalanching of grains. My approach may also be useful in describing disordered systems under shear, where observations of similar intermittency have been made [33, 82, 150].

The differences in the system's behaviour, meanwhile, indicate the possibility of reconciling the two classes of previous experiments: those that exhibit the power-law size statistics associated with self-organised criticality, and those that instead exhibit quasi-periodic system-spanning avalanches. The shallower avalanches of the smaller glass beads have less inertia than those of sand, so that a smaller degree of slope variability is sufficient for avalanches to stop, and hence for the quasi-periodic regime to be disrupted. This would explain the reduced duration of the quasi-periodic regime. From this perspective, in [48, 85], small rearrangements display power-law statistics because even the slope variability associated with individual grains is sufficient to stop the low-inertia motion of small numbers of grains. In [121], one of the varieties of rice has more spherical grains than the other two, and this sphericity not only allows inertia to be higher, due to lower rolling friction, but also reduces the energy barriers associated with the variability of the pile's surface. As a result, avalanches on a small pile of this variety of rice have a narrow size distribution, rather than the broad power-law distribution exhibited by avalanches of the other two varieties. In [207] the system is too small for slope variability to stop avalanches, while in [61, 106, 107, 169], the average slope angle is increased after each avalanche by the rotation of the different drums, so that the system is maintained in the quasi-periodic regime. A system such as that I have described, with macroscopic avalanches propagating on a slope both undisturbed by rotation and sufficiently long for avalanches to be able to stop, can support both the quasi-periodic regime and the irregular regime and will exhibit intermittency between them.

2.4 Recommendations

I recommend the following extensions to this work:

- Conduct experiments in a longer channel, to verify that my results are robust to changes in system size.
- Determine the boundary between the quasi-periodic and irregular regimes in the $\theta - \sigma^2$ parameter space, inclining the channel between avalanches to control θ and using acoustic perturbations to control roll waves and hence σ^2.
- Attempt to predict the lengths of avalanches with the continuum models discussed in chapter 1, using Monte Carlo methods to account for uncertainty in parameters and pile profile measurements, to which the system is sensitive.

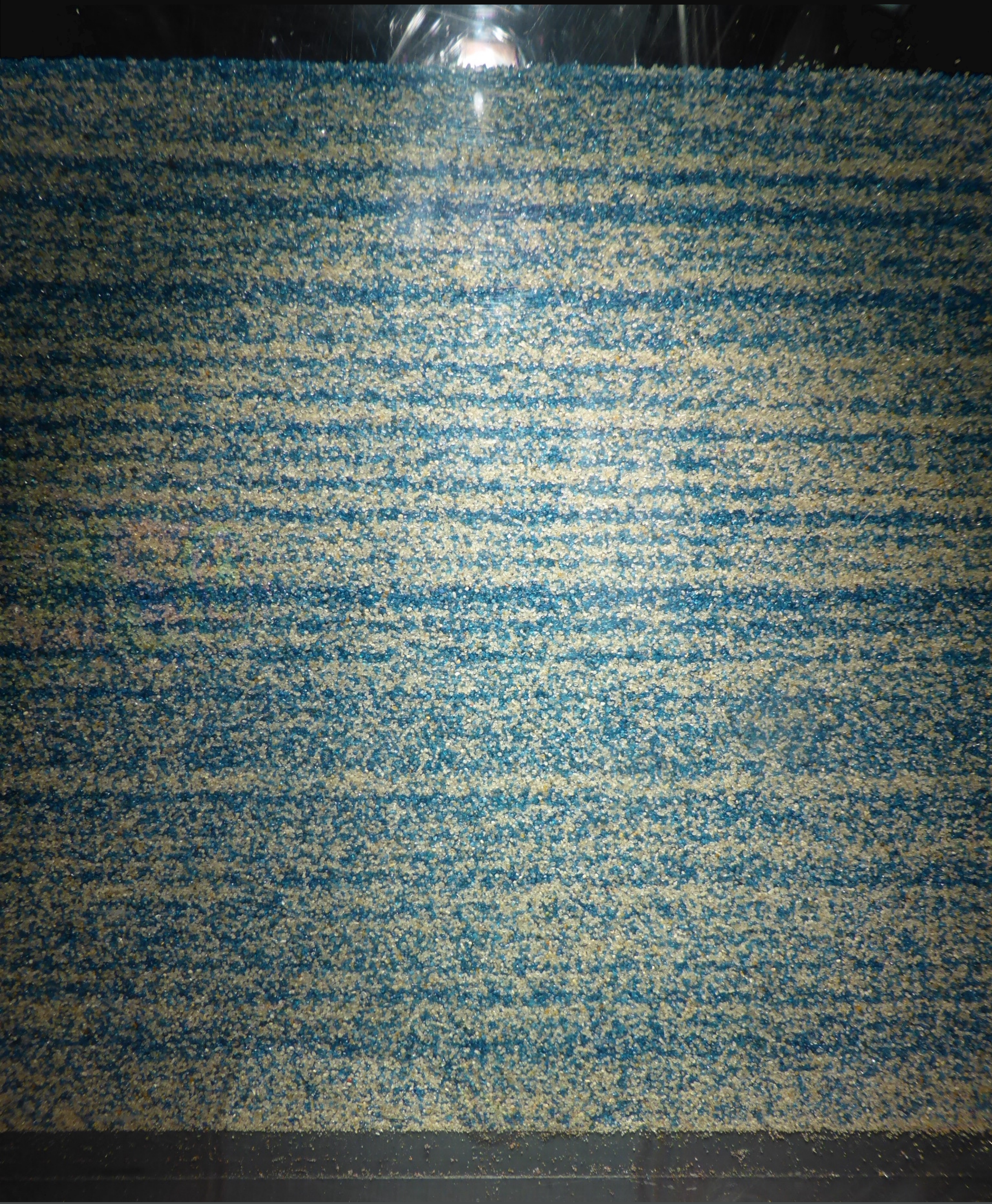

Strata emplaced by discrete avalanches of a mixture of large, blue-dyed and small, undyed grains of sand. Grains were permitted to flow, slowly, into a channel 2.5 m long, 5 cm wide and inclined at 32.3°. The image, taken with a Panasonic DMC-TZ40 camera, is centred 1.3 m downslope (left) of the supply of grains and is 18 cm wide.

Chapter 3

The emplacement of strata by avalanches

‘To see a World in a Grain of Sand...’

William Blake, *Auguries of Innocence*

Abstract

In sedimentary rocks formed from aeolian dunes, internal layers are often used to interpret the paleoenvironment in which the rocks’ sediment grains were deposited. These layers most commonly take the form of inversely-graded cross-strata, emplaced by avalanches on the ancient dunes’ slip faces, but from such cross-strata it is difficult to interpret those dunes’ heights, which have implications for paleowind conditions and paleoclimate. I review the literature on granular size-segregation and stratification. Then, noting some implications of chapter 2’s results, I propose that the mean width $\bar{Y}$ of cross-strata is proportional to the downslope distance X at which they are emplaced, and so that the height of a dune is proportional to the mean width of the cross-strata in the rock it forms. I test the first hypothesis in the experimental channel described in chapter 2, dyeing the largest grains of a volume of sand so that cross-strata may be photographed through the channel’s sidewall. Analysing such photographs, I verify that $\bar{Y} \propto X$, at least for large X, and discuss the implications for the interpretation of dune height.

3.1 Introduction

3.1.1 Avalanche-emplaced cross-strata

On the surface of grain piles such as sand dunes, an important consequence of the avalanches discussed in chapter 2 is the emplacement of successive layers, lying at the grains' angle of repose. In each angled layer, known as a cross-stratum, large grains overlie smaller grains, a property referred to as inverse grading [261, 285]. Noted in sedimentary rocks as early as 1859 [274], these inversely-graded cross-strata were linked to surficial avalanches on aeolian sand dunes by Bagnold in 1941 [22]. Since then, geologists have used the properties of such avalanche-emplaced cross-strata, preserved in certain sedimentary rocks, to identify the sediment as having been deposited by avalanching on dunes and to interpret properties of those dunes (e.g. [180, 189, 214, 228, 230, 276, 277, 312]). For the purposes of identification, Hunter introduced a systematic classification of structures visible within dunes, including cross-strata [163][a], whilst Brookfield classified a hierarchy of the bounding surfaces between cross-strata [55]. In this hierarchy, a first-order bounding surface arises from the migration of a large dune, a second-order surface from the migration of smaller dunes on the surface of the larger, and a third-order surface from reworking of the material forming a dune's leeward face, due to external, environmental change (see Fig. 3.1). Kocurek slightly modified this hierarchy of boundary surfaces [190] and wrote a review [188] on their interpretation, as well as on that of the cross-strata they bound.

Of those properties interpretable from cross-strata, dune height is of particular interest. Since a dune's slip face lies at the angle of repose of its constituent grains, it is clear that the length of the slip face will be proportional to its height. Similar arguments explain the observation that, among dunes of a particular form, dune heights scale with their lateral extent [22, 113, 154, 205], so that an ancient dune's height can be used to infer its morphology (e.g. [27]). Meanwhile, the rate of sediment transport over a dune's slip face is the product of its height, its width, its migration rate, and an estimable, non-dimensional constant reflecting the proportion of sediment captured by the dune [22, 113, 259]. If migration rates are calculable, for example via repeated third-order bounding surfaces reflecting seasonal reworking of dunes, an estimate for dune height therefore permits calculation of the rate of sediment transport,

---

[a] Hunter's classification is summarised in chapter 4, section 4.1.

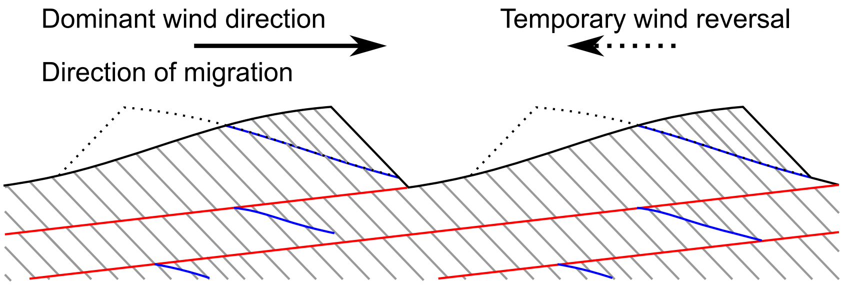

Figure 3.1: Schematic of bounding surfaces (vertically stretched). Avalanches on the leeward face of aeolian dunes emplace inversely-graded cross-strata (grey) at the constituent grains' angle of repose. The migration of dunes in a situation of net sediment deposition results in the emplacement of first-order bounding surfaces (red), typically at angles of less than a degree. The reworking of previously-emplaced material, for example by temporary, seasonal reversals of wind direction (surface immediately after reworking dotted), results in third-order bounding surfaces (blue).

providing insight into ancient wind conditions. Furthermore, in a given dune field, the maximum attainable dune height has been linked to the height of the atmospheric convective boundary layer [13], which has a significant role in paleoclimate modelling [125, 175]. However, most aeolian sandstones preserve only a fraction of the height of the original dunes, which cannot, therefore, be estimated from bed-scale properties without multiple approximations [189, 259].

The first quantitative relation between the properties of cross-strata and the size of dunes was developed by Allen in 1970 [10]. From work on subaqueous dunes, he noted that the flux of grains settling on a dune's slip face decreases as some negative power $-n$ of distance downslope [8, 9]. Therefore, unless grains are redistributed, the top of the slip face will steepen over time until it yields, grains avalanche, and the slope adopts a constant, residual angle. Introducing the 'angle of initial yield' and the 'residual angle after shearing' (equivalent to the maximum slope angle θ_m and the angle of repose θ_r, respectively, that I defined in chapter 2), he predicted that avalanching will either be continuous or quasi-periodic. The majority of the paper considers the case of grains in a rotating cylinder and compares predictions of the avalanche period to experimental measurements. In the discussion, however, Allen considers the width of cross-strata emplaced by avalanching on dunes, in the case of an infinite separation of timescales between fast avalanching and slow deposition of grains. He derives an expression for this width Y that may, after a sign error is corrected and an integral calculated, be written in terms of n, θ_r, θ_m, the distance downslope at which the yield occurs x, and the slip face length

L:

$$Y = \frac{\theta_m - \theta_r}{n(n-1)} \left(\frac{x}{L}\right)^2 \left[1 - n\left(\frac{x}{L}\right)^{n-1}\right]. \tag{3.1}$$

Since dune height $H = L \sin \theta_r$, this expression should allow calculation of H from Y. However, Allen's previous experiments demonstrated that the values of n and x depend strongly on the rate of sediment transport, so that, in practice, H is incalculable for paleodunes. Furthermore, Allen's derivation assumes that each avalanche redistributes grains over the entire length of the slip face, which he notes is unphysical unless the predicted width $Y \gg d$, grain size. Therefore, his expression cannot be assumed for $x/L \ll 1$, the case of large dunes with long slip faces.

In this case of long slip faces, a different relation between stratum width and dune height is proposed by Kocurek and Dott [189]. Hunter having noted wider strata on higher dunes [163, 164], Kocurek and Dott proposed on the basis of field measurements that the width of cross-strata on a dune of height H is bounded above by $A \log H$, for some constant A. However, Kocurek notes that 'data have not been published that demonstrate this relationship for a large, varied dune population, nor has the theoretical basis for this relationship been established' [188].

I seek to use the results of chapter 2 to link the width of cross-strata to the height of the dunes on which they are emplaced, in a more general case than that considered by Allen and with a firmer basis than Kocurek and Dott. To do so, I first consider the mechanism by which detectable cross-strata are formed: the avalanche-induced segregation of grains by size.

3.1.2 Granular size segregation

Such granular size-segregation is an effect so long known that on its earliest apparent description in the scientific literature it was stated as established fact [126]. When a mixture of grains is disturbed, large grains tend to become concentrated in certain regions, while small grains become concentrated in others. Early authors were primarily concerned with the different, industry-specific problems in which this results, from low quality ceramics due to an inconsistently-sized supply of clay [126, 127] to unexpected explosions of excessively fine coal [56, 158]. However, they shared a focus on the case of grains supplied to a fixed location, resulting in the formation of a pile along which large grains tend to propagate further than small grains. This case, of segregation via gravity-driven, surficial avalanching on an erodible bed, continued to be significant for industry [62, 202, 305, 306], with the dominant mechanism considered to be either ‘kinetic sieving’ [240, 270] or the differential capture of avalanching grains by the bed [56, 224].

The ‘kinetic sieving’ framework conceives of the surficial granular flow as consisting of vertically stacked layers of grains moving relative to one another and suggests that, of the particles within a given layer, the smallest are most likely to fall into the void spaces of the layer below (see Fig. 3.2a). In an avalanche on a grain pile, where grains closer to the static bed move more slowly, this downwards segregation of small particles slows their downslope motion along the pile, resulting in the concentration of large grains further downslope. Quantitative studies of kinetic sieving initially considered the case of spherical particles with diameter ratio > 6.47, so that small particles may freely percolate through the voids between large particles even in the absence of strain [50, 51, 234], but insight into the case of shear-induced percolation accumulated through experiments in shear channels and boxes [49, 59, 76, 119, 266, 278], on vibrated beds [307], on grain piles [93, 149, 224, 270], and in rotating drums [74, 89, 153, 179, 239, 240].

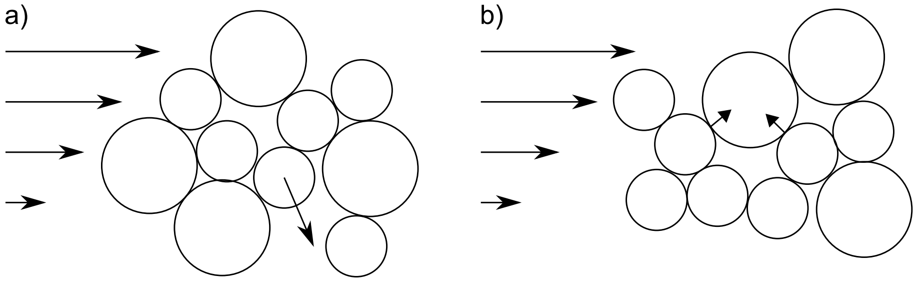

Figure 3.2: Mechanisms for the segregation of grains under gravity-driven shear. Kinetic sieving refers to the downwards migration of small grains, relative to larger grains, due to their higher likelihood of moving into the fluctuating void spaces below them (a). The concentration of grains is equilibrated in the flow by squeeze expulsion, in which higher pressures in regions of high concentration force grains into regions of lower concentration (b). The combination results in the segregation of small particles downwards and large particles upwards.

Insight from such experiments permitted the development of theoretical models, including those of Shinohara et al. [249, 270, 271], Savage and Lun [263], Dolgunin and Ukolov [88], and Gray et al. [140, 142]. Shinohara et al.’s model captures the essential mechanism of small-particle motion through the voids between large particles, but uses unphysical assumptions to derive the size of these voids and is sensitive to three empirical parameters that can be calculated only by fitting. Savage and Lun introduced the concept of ‘squeeze expulsion’, a size and direction-neutral mechanism equilibrating volume fraction within the flow (Fig. 3.2b), and their model uses entropic arguments to link easily-estimable packing parameters to the size distribution of the voids between particles, but they assumed the motion of overlying particles into these voids is instantaneous whenever such motion is possible and so their model has no dependence on gravity. Dolgunin and Ukolov simply assumed a reasonable form for the segregation flux of small particles, while Gray et al. noted that kinetic sieving is associated with smaller particles bearing a disproportionately small proportion of the overburden pressure, including the effect of gravity at the cost of having no explicit dependence on shear rate, while introducing an empirical parameter. Writing the concentration of small particles c, Savage and Lun derived in the limit as $c \to 0$ a downwards segregation flux of small particles proportional to $c(1-c)$, and this was assumed for all c by Dolgunin and Ukolov and by Gray et al., both noting that it is the simplest form satisfying zero flux when $c = 0$ or $c = 1$.[b]

3.1.3 Stratification on grain piles

Despite this work on kinetic sieving, stratification on grain piles received attention as a result of the work of Makse et al., for whom the only important mechanism was the differential capture of avalanching grains by the underlying bed [219–221]. Considering the inflow of large grains onto an existing, channelised pile, at a rate sufficient to maintain continuous flow of grains down the pile, these authors observed stratification only when larger grains had a higher angle of repose than small grains. Otherwise, large grains simply became concentrated at the bottom of the pile. Makse et al. [221] initially modelled this process by considering the addition of grains individually, in a cellular automaton, and followed Brown [56] and Matthée [224] in suggesting that small grains, being more likely than large grains to settle into small irregularities on the pile's surface, would become concentrated upslope. To form a stratum, however, the automaton enacted an unphysical redistribution of these smaller grains on top of the larger grains further downslope. A subsequent paper [220] refined this automaton and

---

[b] It should be noted that such models for segregation predicted the results of subsequent experiments well [155, 156], though improvements continue. Experiments in an annular shear cell [135, 226] and in a channel [102, 301] indicated that the downwards flux of small particles is not symmetric in c and $1-c$, reflecting asymmetry in the mechanisms by which small and large particles migrate, and this led to the modifications of Gajjar and Gray [123], tested in a shear box by van der Vaart et al. [287]. Further insights on asymmetry have been attained through discrete particle modelling (e.g. [172]). Currently unexplained are observations that a sheared mixture of particles relaxes exponentially to a segregated state, rather than segregating in finite time [99, 135, 226], and an observation, for large size ratios, of slower migration upwards of large particles [135], or even migration downwards [282]. Gray provides a review [138].

introduced related, partial differential equations of motion, in the spirit of the BCRE model discussed in chapter 1 [40, 41], but now in three variables representing the height of the static bed and the heights above it of avalanching grains of each species. In both the automaton and the continuous model, avalanching grains are advected downslope at a constant, uniform speed, and deposited when the local slope angle falls below an angle of repose dependent on the size of both the avalanching grains and the surficial, static grains. In contrast, Boutreux and de Gennes [43] used the BCRE framework to consider two species of particle with different angles of repose, but assumed those angles of repose to be independent of the static bed and instead permitted interactions between the two species of avalanching grains. As a result, Boutreux and de Gennes recovered only segregation downslope of the particles with the lower angle of repose, whilst Makse et al. recovered stratification, through the mechanism of successive, upslope-propagating ‘kinks’: small-particle-dominated regions between upper and lower slopes that were surfaced with large particles and at their steeper angle of repose. In each ‘kink’, the local slope angle was sufficiently low for grains to be deposited, the smaller grains first and then the larger, which would therefore overlie previously-deposited small grains (Fig. 3.3a). This mechanism was further explored in a paper by Makse alone [219], which integrated the interspecies interactions of Boutreux and de Gennes but continued to neglect kinetic sieving and to relate ‘stratification to the difference in repose angles of the two pure species’.

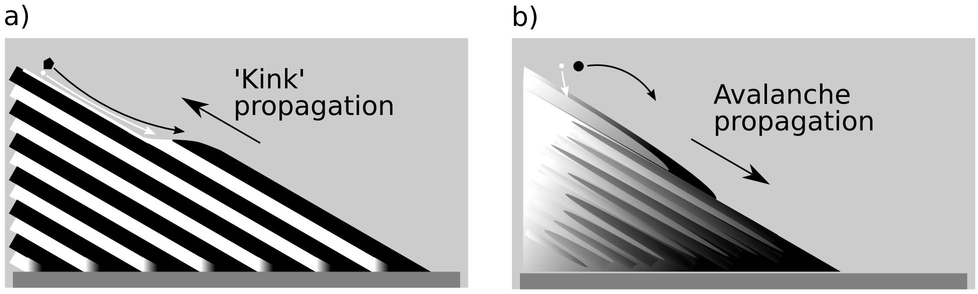

Figure 3.3: Mechanisms for stratification of large (black) and small (white) grains. For continuous avalanching of large, frictional and small, smooth grains (a), the system supports a ‘kink’ on which smaller grains come to a rest earlier than large grains. For discrete avalanches of equally frictional grains (b), kinetic sieving causes large grains to become concentrated at the surface and front of each avalanche, and this segregation is preserved when the avalanche comes to a rest.

Whilst these papers brought stratification to the attention of physicists, a difference in angle of repose was shown to be inessential to strata formation by the experiments of Gray and Hutter [141], using a rotating drum, a silo, and a channel, of Baxter et al. [31], using a conical pile, and of Koeppe et al. [191], using a channel of adjustable width. These experiments investigated the case in which the process initiating avalanches is sufficiently slow that avalanches are discrete. In that case, the superposition of large grains on small, induced in each avalanche by kinetic sieving, is preserved in the successive avalanches' static deposits (Fig. 3.3b). This mechanism, rather than Makse et al.'s, produces strata similar in appearance to those depicted without comment by Williams in 1968, yet it was Makse's paper rather than Williams' that resulted in extensive study of stratification by physicists.

Further study of the two different mechanisms of stratification led to a better understanding of the widths of strata. Grasselli and Herrmann [137] widened the parameter space of Makse's experiments, while keeping larger grains more frictional, and found that stratum width Y increases linearly with inflow rate Q in the regime of continuous avalanching, but tends to a finite value as the inflow rate tends to zero and avalanches become discrete. The linearity of Y with Q was recovered by Cizeau et al. [72], who did not investigate discrete avalanching. Instead, they responded to Baxter et al. by introducing versions of Makse's models with kinetic sieving ('percolation') and by showing that, in a version of the continuum model assuming continuous flow in a single layer, stratification could arise without differences between grains' repose angles, through entrainment of static, small grains by moving, large ones. An alternative approach to continuum modelling was followed by Gray and Ancey [139], who depth-averaged mass and momentum balances of each species to consider the front of a single, discrete, 2D avalanche and noted that large grains are not only supported above small grains within the avalanche, but are also deposited by the avalanche front, leading to wider strata. However, continuum models struggle to capture the initiation and cessation of discrete avalanches, so that experiments are vital to gaining insight.

3.1.4 'Trapped kinks' in stratification

A recent such insight from experiments is the existence of 'trapped kinks' in the regime of discrete avalanching. Shimokawa and Ohta [268, 269] introduced the term to describe avalanche fronts that they observed stopping, partway down a short (< 60 cm), 5 mm wide channel, and they noted that since approximately half of the avalanches in the channel stopped partway down, and since each avalanche emplaced an inversely-graded stratum along its length, there were approximately twice as many strata at the top of the channel as at the bottom.

Consequently, the average width of strata at the bottom of the channel was approximately twice that at the top. Because they used large grains that were more frictional than their small grains, they reasoned that avalanches stopped due to the concentration of large, frictional particles at the avalanche's front, increasing the local angle of repose until flow couldn't be sustained. However, similar behaviour was later observed by Fan et al. [108], in a system of glass beads with equal angles of repose. Varying channel length, inflow rate, and the size ration between large and small particles, they recovered stratification whenever the inflow rate was sufficiently low for avalanches to be discrete and the size ratio was sufficiently high for kinetic sieving to occur, with the mechanism for stratification being the formation of the trapped kinks described by Shimokawa and Ohta. Since Fan et al. used a longer channel, two trapped kinks could even exist simultaneously. Trapped kinks also explain the 'pairing' observed by Koeppe et al. [191] at very low inflow rates. In Koeppe et al.'s channel, each avalanche that stopped partway down the channel emplaced a stratum that was partially eroded by the subsequent avalanche, which travelled to the channel's end. Therefore, narrow and wide strata alternated in the deposit, leading to strata appearing in pairs.

The existence of trapped kinks implies a relation between the height of a sandstone-forming paleodune and the width of the cross-strata it emplaces. The uniformity of aeolian dune sand ensures no significant difference between grains in angle of repose [22, 230], and so it is stratification by discrete avalanching that dominates on aeolian sand dunes [10, 22, 242, 279], as well as on subaqueous deltas [8, 184–186]. On high dunes, with long slip faces, many avalanches will stop partway down the slope, and in fact this was suggested by Allen [10] and has been well-documented using terrestrial laser scanners [238, 242, 279]. The time intervals between avalanches will increase with distance downslope and, translating the stratification observed in experiments to this context, the widths of cross-strata will increase proportionately. Since only the base of paleodunes is preserved in the aeolian record, larger dunes will emplace wider cross-strata, as observed by Hunter [163, 164]. However, this provides only a qualitative relation between dune height and stratum width.

The results discussed in chapter 2 imply the possibility of a quantitative relation between dune height and the width of cross-strata. A dune's slip face can be considered a three-dimensional equivalent of the channelised grain pile on which experiments were conducted, in the time in which the grain pile is being emplaced. When the grain pile is being emplaced, it is bounded, with no opportunity for grains to flow out the bottom of the channel. Grain outflow being the mechanism by which system-spanning avalanches steepen the grain pile's slope, there is consequently no possibility of the pile's slope being sufficiently steep in a zero-front state for the system to switch into the quasi-periodic regime. Therefore, the system will stay in the irregular regime. In this irregular regime of discrete avalanching, multiple stopped avalanche fronts can exist on the grain pile simultaneously, with the frequency of avalanches passing a point at distance X downslope decaying as X^{-1}. The trapped kink mechanism implies that the mean width of avalanche-emplaced cross-strata, at a given point, scales with the mean time interval between avalanches passing that point and hence implies that, in this irregular regime, the expected width of cross-strata at a distance X downslope $Y(X) \sim X$.

Before testing this hypothesis, the utility of consulting a wide literature should be noted. Reference to the sedimentological literature would have permitted the physics community to identify much earlier that kinetic sieving in discrete avalanches is a mechanism for stratification, since it is the primary mechanism for the formation of inversely-graded cross-strata in the sedimentary record. Likewise, the recognition that avalanches can stop partway down slopes was delayed by a failure to consult the relevant geomorphological literature. At the same time, sedimentologists have missed relevant literature on granular flows. For example, Hunter and his antecedents explained size segregation through the shear segregation remarked upon by Bagnold [23] rather than through kinetic sieving. Despite granular physicists having long established kinetic sieving as the dominant segregation mechanism in the gravitational flows relevant to sedimentology, the sedimentological community apparently identified it as the mechanism responsible for inverse grading in cross-strata only in 2011 [84]. Where the same problem arises in multiple fields, progress can be made much more quickly by reading the work of researchers from more than one of those fields.

3.2 Methods

I conduct experiments in the 2.5 m long, 5 cm wide channel described in chapter 2 and use the angular construction sand described in the same chapter, with the grain size distribution depicted in figure 3.4, a mean particle diameter $\bar{d} = 0.47$ mm, and a standard deviation in particle diameter of 0.10 mm. However, I now use a test sieve, with aperture size 0.6 mm, to separate this sand into small grains and large grains, the latter of which I dye blue with fluid Layout Ink from ROCOL, Leeds. The small, undyed grains have an angle of repose of $\theta_r^S = 32.3 \pm 0.3°$ and a maximum slope angle of $\theta_m^S = 34.4 \pm 0.3°$, while the large, blue-dyed grains have an angle of repose of $\theta_r^L = 30.8 \pm 0.2°$ and a maximum slope angle of $\theta_m^L = 34.6 \pm 0.2°$. Since the maximum slope angles are identical, within error, while the angle of repose of the large grains is smaller than that of the small grains, the mechanism for stratification cannot be the differential capture of grains described by Makse et al..

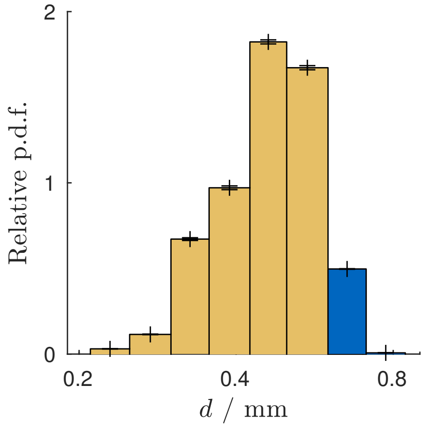

Figure 3.4: Original size distribution of sand used in experiment. I measure the mass-weighted distribution of grain diameters using test sieves. The large, blue-dyed grains are indicated by colour, while error bars indicate the standard error over five repeats.

Inclining the channel at θ_r^S, to within 0.03°, and inclining the plate at its bottom at $0.000 \pm 0.017°$ to prevent outflow of grains, I induce stratification by permitting 7.5 l of the small, undyed grains and 2.5 l of the large, blue-dyed grains to flow, via separate nozzles, into the top of the channel. The flux of the small, undyed fraction of sand is $Q^S = 2.03 \pm 0.07$ cm^3 s^{-1}, while that of the large, blue-dyed fraction is $Q^L = 0.69 \pm 0.08$ cm^3 s^{-1}, and these fluxes are directed to the same point by a V-shaped mixer with vertical outflow. The experimental apparatus is depicted in Fig. 3.5. The total inflow rate is sufficiently small for discrete avalanches to propagate down the channel from its top, on the surface of the pile emplaced by previous avalanches, in the same manner as described in chapter 2.

While grains are flowing into the channel, I measure the approximate size distribution of these avalanches. Before the experiment, I mark a channel sidewall at 150 ± 2 mm intervals downslope, with the first mark 73.0 ± 1.0 mm downslope of the point at which the supply of grains reaches the channel's base. Then, following the establishment of a 15 mm-deep pile

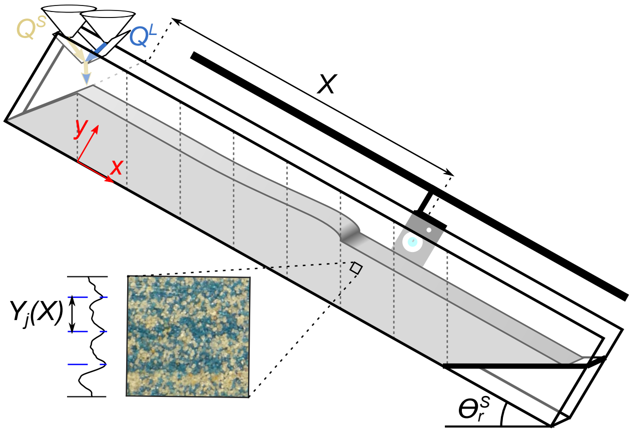

Figure 3.5: Schematic of apparatus used in the experiment. Large, blue-dyed and small, undyed grains flow vertically into an inclined channel, at slow rates Q^L and Q^S, respectively, forming a pile of grains. The sizes of the resulting discrete avalanches are approximated using vertical marks on the channel's sidewall, following which the strata that the avalanches emplace are photographed at distances downslope X, using a camera fixed to a motorised traverse. Stratum widths $Y_j(X)$ are extracted from these photographs, as illustrated.

of grains over the channel's entire length, I record for 150 avalanches the last mark that each avalanche's front passes before stopping. Writing X_k for the distance downslope of the kth mark and $N_j(X_k)$ for the number of avalanches that occur between the jth avalanche to pass the kth mark and the $(j+1)$th such avalanche, I calculate the mean number $\bar{N}(X_k)$ of avalanches to occur between consecutive avalanches of length greater than X_k. This is expected to be directly proportional to the mean width of strata at a distance X_k downslope.

Once the inflow has ceased and the pile is fully developed, I measure mean stratum width by photographing strata through one of the channel's transparent sidewalls. A Panasonic DMC-TZ40 camera is fitted to a computer-controlled motorised traverse, facing the channel and with its short axis downslope. It is aligned with the channel to within 1.0° about each axis. The centre of the camera's aperture is 196.0 ± 2.0 mm from the inner face of the channel's sidewall and a perpendicular distance of 143.0 ± 1.0 mm above the channel's base, so that its field of view encompasses the entire depth of the grain pile and spans 180.0 ± 0.5 mm along its length. The grain pile is lit with a halogen light, fixed on the traverse above the camera, to prevent reflections appearing on the outer face of the channel's sidewall. Using the traverse and controlling the camera via a wireless local area network, images are taken at 50.0 ± 0.2 mm intervals downslope, with the centre of the channel's base in the first image 159 ± 2 mm downslope of the point at which grains are supplied to the channel. Images are processed to estimate the volume fraction ϕ^L of large, blue-dyed grains at different regions of the deposit, and so to extract the widths Y_j of avalanche-emplaced strata. This processing is described and illustrated in Appendix B, section B.1.

3.3 Results

In each avalanche, large and small grains segregate in all three directions: vertically, along the channel, and across the channel. Kinetic sieving and squeeze expulsion result in the preferential migration of large grains to the top of the flow, whence vertical shear transports them towards the front of the flow. At the front, the slower motion of grains at the channel's sides results in cross-channel flow that preferentially deposits large particles along the sidewalls. In trial experiments, discussed in Appendix E, section E.2, these effects decreased the concentration of small grains at the sidewalls and at large distances downslope, to the extent that too few were visible at certain points for strata to be distinguishable.

Such segregation, of large grains downslope and towards sidewalls, is evident when considering the depth-averaged volume fraction of large grains $\bar{\phi}^L$, among those grains visible in photographs of the sidewall (Fig. 3.6). At the sidewalls, $\bar{\phi}^L$ increases by a factor of 5 with distance downslope, while the mean of $\bar{\phi}^L$, along the entire sidewall, is approximately twice the bulk volume fraction of large particles, over all those grains that have entered the channel (equal to $Q^L/(Q^S + Q^L)$).

However, under the experimental conditions described in section 3.2, the extent of along-channel and cross-channel segregation is sufficiently small for each avalanche to deposit both small and large grains at the sidewall, along the avalanche's entire length. In each of these deposits, large grains overlie small, so that strata are clearly visible through the channel's transparent sidewalls (Fig. 3.7).

As a result, the automated extraction of strata widths is reasonably accurate along most of the channel's length. For $X \leq 300$ mm the paucity of large grains prevents the detection of sufficiently many strata for the data to be unusable, but for 350 mm $\leq X \leq$ 600 mm approximately two thirds of strata are continuous and hence detectable; for 650 mm $\leq X \leq$ 1050 mm only one or two visually apparent strata are not detected in each image; and for $X \geq 1100$ mm all apparent strata are detected. Consequently, the mean stratum widths $\bar{Y}$ that I calculate

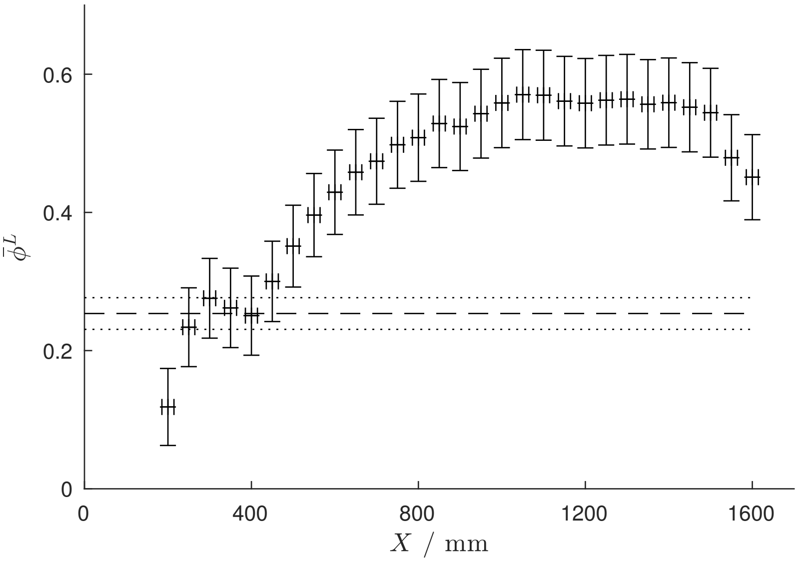

Figure 3.6: Mean volume fraction of large particles at the channel's sidewall, $\bar{\phi}^L$, as a function of distance downslope. Processing photographs through the channel's sidewall, as described in Appendix B, section B.1, I calculate for each $\bar{\phi}^L$ over a window spanning 50 mm downslope and the full depth of the pile, excluding points less than 15 mm from the channel's base or 50 mm upslope from the channel's end. $\bar{\phi}^L$ increases with distance downslope and is higher, on average, than the bulk volume fraction within the entire channel, $Q^L/(Q^S + Q^L)$ (dashed, black line). Error bars and black, dotted lines represent the standard deviation inferred from uncertainty in parameter measurements.

for $X \leq 1050$ mm should be regarded as upper bounds on the true values, rather than the true values themselves, whilst for $X \geq 1100$ mm, my calculated values of $\bar{Y}$ can be used for quantitative comparisons to theory.

Section 3.1's review of stratification suggests that $\bar{Y}$ should be proportional to the value of $\bar{N}$, calculated as described in section 3.2. In previous work, each avalanche emplaced a single stratum, of length equal to that of the avalanche, so that the number of strata at a given point downslope was equal to the number of avalanches that passed that point. Under this assumption, the mean width of strata $\bar{Y}(X)$ at a given distance X downslope should be proportional to the mean waiting time between subsequent avalanches that pass that distance, recorded in terms of the number of avalanches that occur in that time. This value is precisely $\bar{N}(X)$.

Both $\bar{Y}(X)$ and $\bar{N}(X)$ are plotted in Fig. 3.8, which offers mixed support for such a hypothesis. The qualitative behaviour of $\bar{Y}$ is similar to that of $\bar{N}$: increasing between $X = 350$ mm and $X = 600$ mm; remaining approximately constant between $X = 650$ mm and $X = 1050$

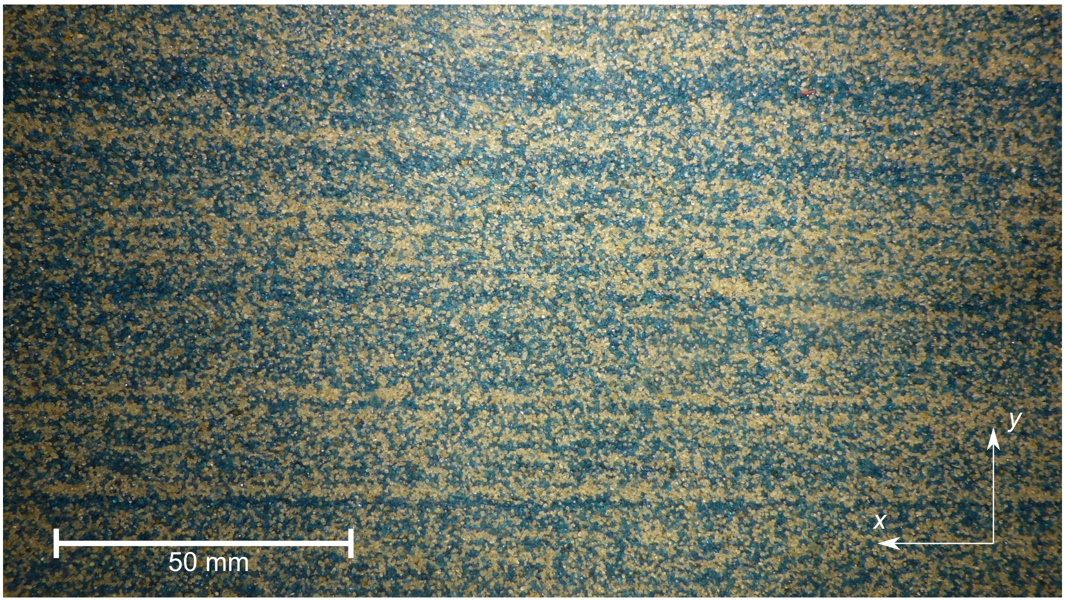

Figure 3.7: Photograph illustrating avalanche-emplaced strata. The centre of the base of the image is 15 mm above the base of the channel and 659 ± 2 mm downslope of the point at which grains are supplied to the base of the channel.

mm; and increasing approximately linearly for $X \geq 1100$ mm. However, $\bar{Y}$ exhibits two significant decreases with X, at around $X = 625$ mm and $X = 1075$ mm. By contrast, $\bar{N}$ is and must be monotonically increasing, because all avalanches start from the top of the channel. Since the minimum number of grains across an experimentally-observed stratum is three, I choose axes such that $N = 1$ corresponds to $\bar{Y}/\bar{d} = 3$. Then, the discrepancies between $\bar{Y}$ and $\bar{N}$ for $X < 1100$ mm are in the direction associated with failures in stratum detection, even if they cannot be attributed with certainty to those failures. For $X \geq 1100$ mm, $\bar{Y}$ coincides with N exactly, so that, in this region, $\bar{Y}(X)$ is inversely proportional to the frequency with which avalanches pass X.

Given this inverse proportionality, I test, for $X \geq 1100$ mm, the implication of chapter 2 that I discussed in section 3.1, that the expected mean stratum width $Y(X) := \mathbb{E}\left[\bar{Y}(X)\right] \propto X$, distance downslope. I consider the hypotheses $H_0 : Y(X) = \beta X$, for some constant β, and $H_1 : Y(X)$ is an arbitrary function of X. In conducting the experiment and measuring, at each value of X, $n(X)$ stratum widths $Y_j(X)$ with unbiased sample variance $s^2(X)$, $\bar{Y}(X)$ is taken from a probability distribution that, by the central limit theorem, is approximately normal with expectation $Y(X)$ and variance $s^2(X)/n(X)$. Assuming that these approximations are exact, I calculate the maximum likelihoods of measuring mean stratum widths $\bar{Y}(X)$ under H_0

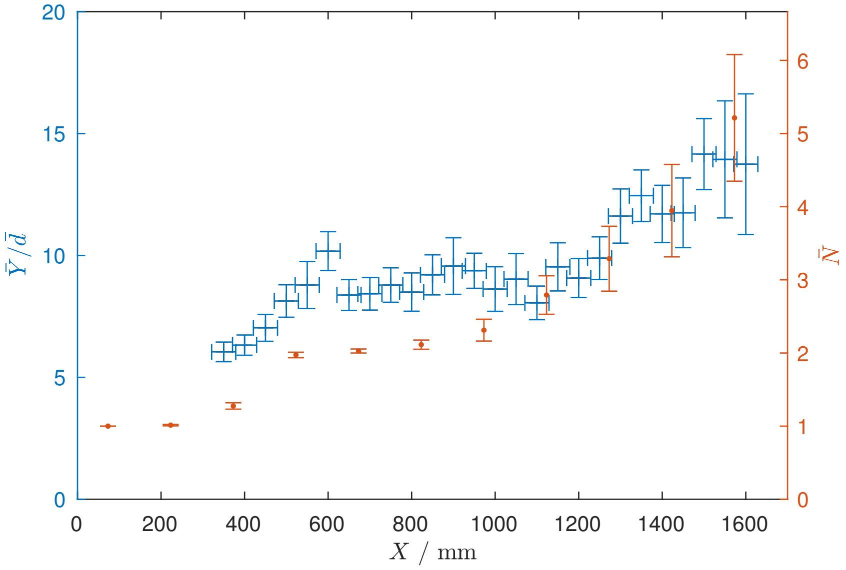

Figure 3.8: Mean layer width $\bar{Y}$ and number interval between avalanches $\bar{N}$ as a function of distance downslope X. $\bar{Y}$ and $\bar{N}$ are calculated as described in Appendix B, section B.1, and in section 3.2, respectively. Error bars represent the standard error over observations, with raw data in Appendix B, section B.2.

(permitting variation of β) and under H_1 (permitting variation of the 11 values of $Y(X)$ that correspond to the 11 values of X at which I take measurements). The likelihood ratio test statistic Λ, equal to the ratio of the maximum likelihood under H_0 to that under H_1, is then 0.025. The parameter space corresponding to H_0 lies in the interior of that corresponding to H_1 and the difference in the dimensionality of the parameter spaces is 10, so Wilk's theorem [303] states that, if H_0 is true and certain regularity conditions are satisfied, then $-2\log\Lambda$ is taken from a distribution approximately equal to a χ^2 distribution with 10 degrees of freedom[c]. Therefore, under H_0, the probability of having measured a more extreme value of Λ is $p \approx 0.68$. This being large, my data are consistent with H_0.

For a more intuitive demonstration of this consistency with H_0, I conduct a least squares linear regression of $\bar{Y}$ against X. Restricting to a $\bar{Y}$ intercept of zero, the coefficient of determination $R^2 = 0.82$. Therefore, for $X \geq 1100$ mm, the strata widths I measure are consistent with the hypothesis that $\bar{Y}(X) \propto X$.

---

[c] An heuristic justification of Wilk's theorem is found in Williams [304]. If the measured values $\bar{Y}(X)$ were taken from a normal distribution, then the approximation implied by Wilk's theorem could easily be shown to be exact.

3.4 Discussion

Observing that $\bar{Y}(X) \propto X$ for $X \geq 1100$ mm, it is important to discuss the discrepancies between $\bar{Y}$ and $\bar{N}$ for $X \leq 1050$ mm. Some proportion of these discrepancies can be explained by the difficulty of detecting every stratum at low X and I note that the same reason exists for this difficulty and for any discrepancies unexplained by it: overrunning avalanches can mobilise static grains. Under the experimental conditions that I have described, each avalanche emplaces an inversely-graded stratum when it stops. However, this stratum's static grains can be remobilised by a subsequent avalanche and this is particularly likely for large grains in thin strata, emplaced by those avalanches that stop near the top of the channel. Being near the top of the channel, the stopped avalanche front is very likely to be overrun and may well have stopped on the surface of another stopped avalanche, leading to a deeper yield surface that mobilises more grains. Surficial grains are more accessible to remobilisation and, once a large grain is remobilised, it will rise to the surface of the overrunning avalanche and is unlikely to be deposited close to its original position. Therefore, the mobilisation of grains by overrunning avalanches may, rarely, remove entire strata or, more frequently, it will deplete the large, surficial grains of a stratum, increasing the difficulty of detecting it.

This explanation implies stronger correlation between $\bar{Y}$ and $\bar{N}$ in aeolian sandstones. As sandstones form from basal deposits of aeolian dunes, the strata emplaced in their deposition are less likely to have been overrun by subsequent avalanches and so grains are less likely to be remobilised, with the original stratum widths preserved in the final sandstone. Having been deposited a large distance downslope, strata will be wide, so that, if grains of a stratum are remobilised, a smaller proportion of the stratum is removed. Finally, geologists distinguish adjacent aeolian cross-strata by substrata referred to as 'pinstripes', composed of the smallest grains [188, 228]. Since these grains will have been emplaced at the bottom of avalanche deposits, they will be the least accessible to remobilisation, and since they will settle the base of any flow, any remobilisation is unlikely to transport them far. Consequently, each stratum is likely to remain distinguishable even if some proportion of its grains are remobilised by a subsequent, overrunning avalanche.

However, there are two barriers to applying this work directly to the interpretation of aeolian sandstones: the difference between considering $\bar{Y}(X)$ on the single slipface examined in experiments and $\bar{Y}(L)$ on different slipfaces of lengths L; and the difference between the quasi-two-dimensional channel used in experiments and the fully three-dimensional slip faces of physical dunes.

Extending my results to slip faces of different lengths L requires the assumption that near-source behaviour is independent of L. This appears reasonable, since information propagates from the end of the channel to small X only when an avalanche stops upon reaching that end. In this case, a granular bore propagates upslope, of the type discussed by Edwards and Vriend [102]. Further experiments are required to consider the behaviour of this bore, but it seems unlikely to change the behaviour of $Y(X;L)$ at small X and hence to change the behaviour of $\bar{Y}(L)$.

Of greater concern is the three-dimensional nature of dune slip faces, complicating the relationship between $\bar{N}$ and X. In a channel, all avalanches are constrained to have the same cross-slope extent and to follow the same path downslope, so that the overrunning-mobilisation mechanism discussed in chapter 2 implies that the lengths of overrun avalanches contribute additively to the length of the overrunning avalanche. This results in the relation between $\bar{N}$ with X seen in Fig. 3.8, in which $\bar{N} \sim X$ for $X > 1000$ mm[d]. However, on a dune's slip face, avalanches have different source positions and different cross-slope extents [238]. Consequently, the implication of the overrunning-mobilisation mechanism for the function $\bar{N}(X)$ is unclear.

Further experimentation is therefore required to investigate the effects of varying slipface length and of higher dimensionality, to test the implication of this work: at the end of a dune's slip face, length L, the mean width of the cross-strata emplaced by avalanches, $\bar{Y}(L)$, is proportional to L.

---

[d] The behaviour of $\bar{N}$ for $X < 900$ mm is controlled by a) near-source effects and b) the constraint that N is an integer.

3.5 Recommendations

I recommend the following extensions to this work:

- Conduct experiments with different sand, to verify the robustness of my results.
- Divide the volume of smaller grains of sand into two fractions by size, dyeing the larger grains a new colour, and repeat experiments. This would allow more robust detection of strata, decreasing the number of cases in which a stratum is denuded of all grains except those that are small and undyed.
- Conduct experiments in channels of different lengths L, to investigate whether near-source behaviour is independent of L.
- Conduct experiments with a line source at the top of a slope of greater width, to investigate three-dimensional effects.

Avalanche-emplaced cross strata in a dune, visualised by the preferential permeation of water along stratigraphy. Water, added to a dune's surface 10 m upwind of its peak, causes cohesion in regions of sand into which it has permeated. On exposure of a vertical face, parallel to the dune's migration, such regions appear in relief. The image, taken with a Sony RX100 camera, is 21.5 cm wide.

Chapter 4

Observations of strata in sand dunes

> *‘Ce qui embellit le désert, ... c’est qu’il cache un puits quelque part...’*
>
> Antoine de St. Exupéry, *Le Petit Prince*

This work was conducted as part of a large, interdisciplinary collaboration, led by Prof. Michel Louge of Cornell University. Practical and theoretical contributions to this work were made by Prof. Louge and Prof. Anthony Hay, also of Cornell University.

Abstract

In many desert regions, the migration of sand dunes poses problems for infrastructure and agriculture. The pattern of water permeation within these dunes often determines whether interventions to stop this migration are successful and this permeation of water is affected by the avalanche-emplaced strata discussed in chapter 3. However, previous work has not linked the permeation of water to quantitative measurements of grain size on the scale of individual strata. In this chapter, I describe fieldwork conducted on Qatari barchan dunes, extracting samples to measure grain-size distributions across individual strata. The results are frequently unclear, but indicate that the widths of strata increase with the distance downslope X at which they were deposited; that sorting improves with increasing X; and that water preferentially permeates along the regions of strata in which smaller grains are concentrated. This suggests that water will permeate to and reside within defined regions of dunes’ interiors, where it will be available for bacterial or vegetative dune stabilisation.

4.1 Introduction

4.1.1 Motivation

The impacts of sand dunes are not limited to the sandstone emplacement which I discussed in chapter 3, and are also evident while they are active. For example, over 239,000 km^2 of land in Northern China underwent desertification between 1955 and 2005 [281], 5.5% of which was due to the encroachment of sand dunes[317]. The motion of dunes threatens roads, homes, and other infrastructure [53, 57, 80, 91] and since dunes may contain over a million tonnes of sand [22, 154], and will engulf barriers placed in their path [7, 146], this infrastructure is difficult to protect.

It is therefore desirable to stabilise certain sand dunes, stopping their migration. In coastal areas and semi-arid regions, temporary stabilisation is achieved by coating dunes with mulch, geotextiles, or chemical sprays, allowing the planting of vegetation that will stabilise dunes permanently [2, 68, 91, 146, 210]. In desert regions, however, successful planting is often impossible, due to the aridity of the environment and the continued transport of surficial sand [7, 34]. In Saudi Arabia, long-lived oil-based coatings have been used with some success [7, 297], but these have negative impacts on wildlife and hinder vegetation, and less environmentally-damaging approaches are increasingly sought. One promising such approach is the facilitation of grain cementation by bacterial action.

Certain species of bacteria cause the precipitation of calcium carbonate as a byproduct of their respiration [26, 159] and, on the surfaces of sand grains, this precipitate acts as cement, introducing cohesion to otherwise uncohesive sands [86, 235, 264]. First used to plug pores in oil reservoirs [111, 178], this ‘biocement’ shows promise in the stabilisation of sand, allowing soil improvement and subsequent revegetation [275]. An example of biocement-forming bacteria has successfully been isolated on a barchan sand dune in Qatar [1], but the viability of these bacteria depends on the presence of water.

As a result, the hydrology of desert dunes is important not only for considering the viability of dune vegetation, but also for predicting exactly where and under what conditions bacterial life can exist within dunes, for the purposes of soil improvement and sand cementation. If water is unable to propagate beyond a dune’s surface, then few bacteria will survive their residence in the dune’s interior and there will be insufficient bacterial life for biocementation to be feasible.

At the same time, if water is highly localised within the dune, then any cementation and soil improvement will also be localised and dune stabilisation is unlikely to succeed. I therefore consider the permeation of water within a sand dune.

4.1.2 Water permeation within dune sand

The permeation of water in dune sand is a complex process. In an unsaturated granular medium, the capillary potential $\varPsi$ is akin to a pressure, expressing the local rate of increase, with volumetric water content, of the surface energy arising from the attraction of water molecules to the grains and to other water molecules[a]. Water of density ρ_w therefore experiences a conservative body force $\boldsymbol{F} = \rho_w \boldsymbol{g} - \nabla_{\boldsymbol{x}} \varPsi$, for gravitational acceleration $\boldsymbol{g}$. However, water's viscosity μ impedes its motion within the tortuous network of narrow pores between grains, so that Darcy's law [83] describes the flux of water: $\boldsymbol{q} = (K/\mu)\boldsymbol{F}$ for some local permeability K. By mass conservation, the rate of change of volumetric water content w is therefore captured by the Richard's equation [253, 255][b]:

$$\frac{\partial w}{\partial t} = -\nabla_{\boldsymbol{x}} \cdot \left[\frac{1}{\mu} K \left(\rho_w \boldsymbol{g} - \nabla_{\boldsymbol{x}} \varPsi \right) \right]. \tag{4.1}$$

In this equation, both K and $\varPsi$ depend on w. A higher volumetric water content connects more paths through the pore network and increases these paths' cross-sectional areas, increasing permeability. However, such increases in w fill the sites at which additional water can most quickly decrease surface energy density U_{surf}, decreasing the (negative) capillary potential's magnitude $|\varPsi| = -\partial U_{\text{surf}}/\partial w$ (Fig. 4.1). The relation is complicated by hysteresis in K and $\varPsi$ with w, since both variables depend not only on the volume of water within a pore network, but also on its distribution [245, 310]. As water is imbibed, it is concentrated in those areas most accessible to it, whilst following drainage it is concentrated in those areas least accessible to air. Much work has been done in hydrology, soil science, plant science, and geotechnical engineering to calculate the functions K and $\varPsi$ for different mixtures of grains, as reviewed by Masrouri et al. [223], Leong and Rahardjo [208], Whalley et al. [299], and Patil and Singh [241]. Meanwhile, Farthing and Ogden [109] review the work done to solve Richard's equation in specific cases.

---

[a] Since water molecules are attracted to the grains, the surface energy associated with any volume of interstitial water is negative, and so $\varPsi$ is also negative.

[b] While this equation was first noted by Richardson, in his grand proposal for meteorological forecasting [255], I abide by convention in its naming.

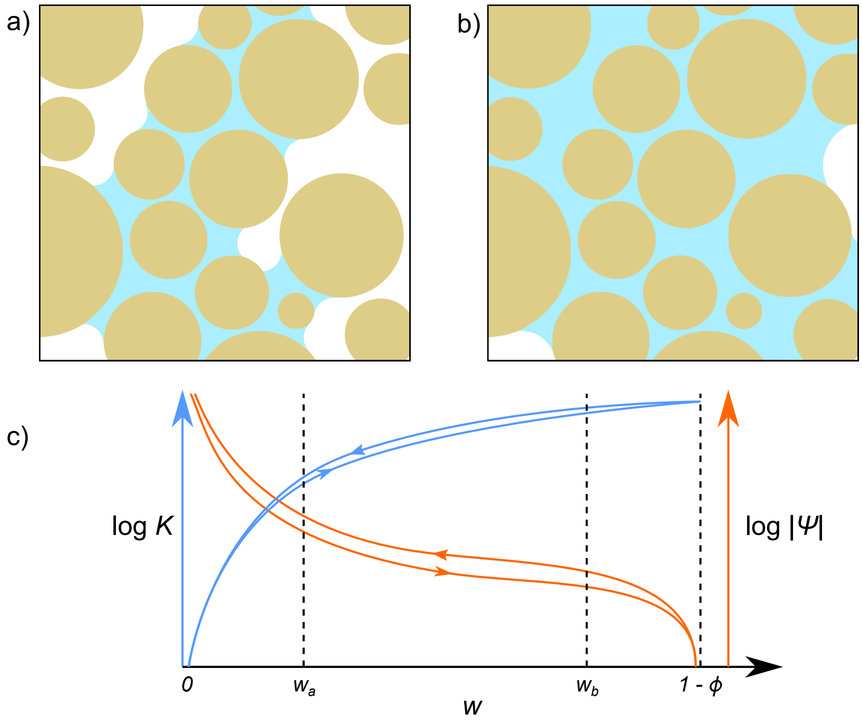

Figure 4.1: Schematic demonstrating dependence of permeability K and capillary potential Ψ on volumetric water content w. In a pore throat of effective radius r, a small volume δw of additional water wets a surface area $\delta A \approx 2\pi r(\delta w/\pi r^2)$, decreasing surface energy U by $\approx 2\gamma_{sl}\delta w/r$ for solid-liquid surface tension $\gamma_{sl} > 0$. Consequently, pores of smaller effective radius are preferentially filled. At low w (a), water fills the pores of small effective radius (say $r \leq r_1$), so that permeability is low ($K \sim r_1^2$, by considering Poiseuille flow) and the capillary potential's magnitude is high ($|\Psi| = -\partial U/\partial w \sim 1/r_1$). At high w (b), since small pores are saturated, water fills larger pores, K is high, and $|\Psi|$ is low. This behaviour is sketched in c, with no connected fluid network as $w \to 0$, so that $K \to 0$ and $|\Psi| \to \infty$, and the medium saturated at $w = 1 - \phi$, so that $\Psi = 0$. Both K and Ψ are hysteretic due to hysteresis in the distribution of water within pores. Relations with pore radii r and r_1 are idealised and indicative, rather than realistic.

In such solutions of the Richards equation, heterogeneities in K and Ψ cause heterogeneities in water content, as observed within sand dunes by previous authors. McCord and Daniels [227] used tracer experiments and neutron probes to study the permeation of water on stabilised dune sand, following precipitation, and observed lateral permeation of water on scales of between 10 cm and 20 m. They hypothesised that water migrated along regions in which existing water content increased permeability, which mechanism was further investigated by Ritsema and Dekker [257] and Berndtsson et al. [34]. Ritsema and Dekker used steel core samplers to measure water content with 5 cm vertical resolution on five desert dunes and four coastal dunes, observing on the latter preferential permeation of rainfall along existing, vertical flow paths.

Berndtsson et al. observed similar behaviour on a stabilised dune by using neutron probes, but also noted higher water content at the crest and trough of the dune and linked this to strata visible within the dune.

However, none of these authors link variations in water content to the variation that makes strata visible: that in grain-size distribution. The stratification described in chapter 3 causes the distribution of grain sizes to vary between different regions of a dune, so that the pore network between grains has properties which are spatially heterogeneous. Larger pore throats impede the flow of water to a lesser extent than small pore throats, increasing K, and a greater volume of water is required within them for the same decrease in surface energy, decreasing $|\Psi|$. Consequently, in regions of larger grains, or narrower grain-size distribution and hence looser packing, K is higher and $|\Psi|$ lower for the same w [151, 208, 216]. This heterogeneity of K and Ψ implies heterogeneous permeation of water, associated with the internal structure of dunes.

4.1.3 The internal structure of dunes

The internal structures of dunes were classified by Hunter [163], who defined six types of strata in aeolian sand deposits, depicted in Fig. 4.2. ‘Planebed laminae’ are rare, forming on flat surfaces subject to high windspeeds, due to the tractional deposition, at different times, of grains with different properties. ‘Grainfall laminae’ are laid down in regions of flow separation, as decreasing wind speeds allow previously saltating grains to settle on existing topography, while the net deposition of saltating grains on the wavy surface of aeolian ripples leads to ‘ripple-form laminae’. Faster ripple migration, in relation to the net deposition rate, can result instead in ‘ripple-foreset cross-laminae’, parallel to the lee faces of ripples, but these cross-laminae are rarely visible due to the subtlety of the differences between grains deposited at slightly different times. In any case, the migration of sand ripples forms ‘climbing translatent strata’, in a manner analogous to the formation of first-order bounding surfaces, by dunes, that I introduced in chapter 3, section 3.1. These climbing translatent strata tend to be a few centimeters thick along most of the windward slopes of dunes and slightly thicker at the crests and toes of such slopes, where aeolian ripples migrate above sand deposited by slip-face avalanches. The strata emplaced by such avalanches, the subject of chapter 3, are referred to by Hunter as ‘sandflow cross-strata’ and are the most common structure in the interior of dunes. As discussed in chapter 3, avalanche-emplaced cross-strata are inversely-graded, with large grains overlying smaller grains in each stratum, and are most easily distinguished by thin basal layers of the smallest grains, often consisting of heavy minerals.

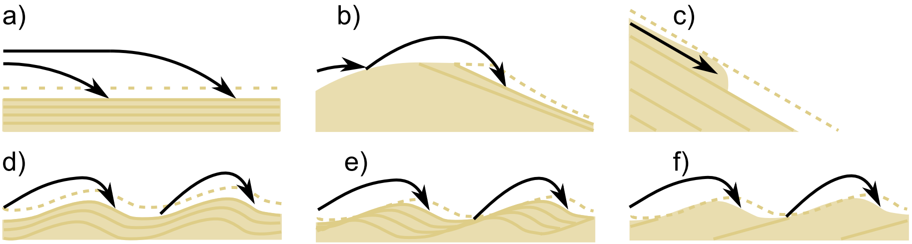

Figure 4.2: Varieties of strata within aeolian dunes. Hunter [163] classified aeolian strata into six categories, described in the text: planebed laminae (a), grainfall laminae (b), sandflow cross-strata (c), ripple-form laminae (d), ripple-foreset cross-laminae (e), and climbing translatent strata (f)

Whilst the strata identified by Berndtsson et al. appear to be Hunter's climbing translatent strata, a wider variety of structures have been revealed by McKee's excavation of trenches in active dunes. Studying gypsum dunes with cohesive interiors in 1966 [229], he excavated trenches through parabolic, barchanoid, and dome dunes and observed sandflow cross-strata through most of each dunes' interior, as well as ripple laminae and the third-order bounding surfaces described in chapter 3, section 3.1, arising from temporary changes in wind direction. He made similar observations in a wider range of dune types in 1982 [231], excavating trenches in dunes of uncohesive quartz sand by artificially adding water and interpreting strata to consider the migration of linear dunes. However, the excavation of trenches is time-consuming and expensive, leading to the use of ground-penetrating radar.

A ground-penetrating radar survey uses high-frequency electromagnetic radiation to non-destructively image the subsurface structure of a dune. A surficial transmitter emits waves, which propagate within the dune; are reflected by internal interfaces of electric permittivity; and are detected at a surficial antenna. The times between emission and detection are interpreted for a range of transmitter and antenna positions, in order to reconstruct the subsurface reflectors. The use of ground-penetrating radar in sedimentology and the interpretation of the resulting data were reviewed by Neal [237], who also lists work done with ground-penetrating radar on aeolian dunes.

Amongst such work, two early papers link water permeation to internal structure. Having surveyed a complex dune, Bristow et al. [52] compared reconstructed reflector positions with the internal structure observed through trench excavation, demonstrating that waves were reflected at the interfaces between avalanche-emplaced cross-strata and at the bounding surfaces between sets of such strata. They explained this by noting that significant variations in electric permittivity arise from variations in water content and that variations in water content are associated with variations in grain size within dunes. Harari [147] used these associations to interpret ground-penetrating radar surveys of a dome dune and a barchan dune, identifying cross-strata, groundwater, and regions of locally high water content to conclude that water preferentially permeates along stratigraphy.

The relevance of this preferential permeation to dune stabilisation is demonstrated by the association of water content with cross-strata and with calcium carbonate precipitate. Yang et al. [313] observed layers of calcium carbonate precipitate in dunes of the Chinese Badain Jaran and linked these layers to former dune surfaces and historical water content. Hunt and Vriend [162] went further, using ground-penetrating radar to detect cross-strata within a Californian dune, associating these strata with changes in water content, and linking this water content to calcium carbonate precipitate extracted from the dune. Qian et al. [247] made corresponding observations and considered a dune's large-scale hydrology. On the basis of simple hydrological calculations, they suggested that the preferential permeation of water along the dune's stratigraphy was sufficiently strong for the dune to be the main source of water recharge for a lake at the base of its slip face. The preferential permeation of water not only leads to the formation of biocement, but results in the concentration of water resources on a macroscopic scale.

Given the importance for dune stabilisation of preferential permeation along stratigraphy, as defined by differences in grain-size distributions, it is vital to understand the microscopic mechanisms at work. However, no quantitative measurements exist of grain size variation on the scale of individual strata, nor has such variation been linked to water penetration on the scale of centimeters, of which measurements are limited [215]. I therefore seek to measure grain-size distributions with substratum resolution and to link variation in these distributions to the permeation of water.

4.2 Methods

4.2.1 Field site

To investigate grain-size distributions, I conduct fieldwork at a dune field in Al Wakrah municipality, Qatar, 25.01° N, 51.34° E, with location within Qatar indicated in Fig. 4.3a. The site has a hot desert climate (BWh under the Köppen climate classification [194–196]), with annual mean temperature 28.08 ± 0.17°C and 60 ± 12 mm of annual precipitation. Mean temperature and total precipitation are plotted by month in Fig. 4.3b, demonstrating limited, highly-seasonal rainfall. Only very limited vegetation is viable, so that surficial, unconsolidated sediment is not stabilised and can be transported by the wind. This wind is predominantly from the north-west, with wind rose plotted in Fig. 4.3c, resulting in net sediment transport at a bearing of 155 ± 2 from true north. 'Downwind' will henceforth refer to this direction of sediment transport.

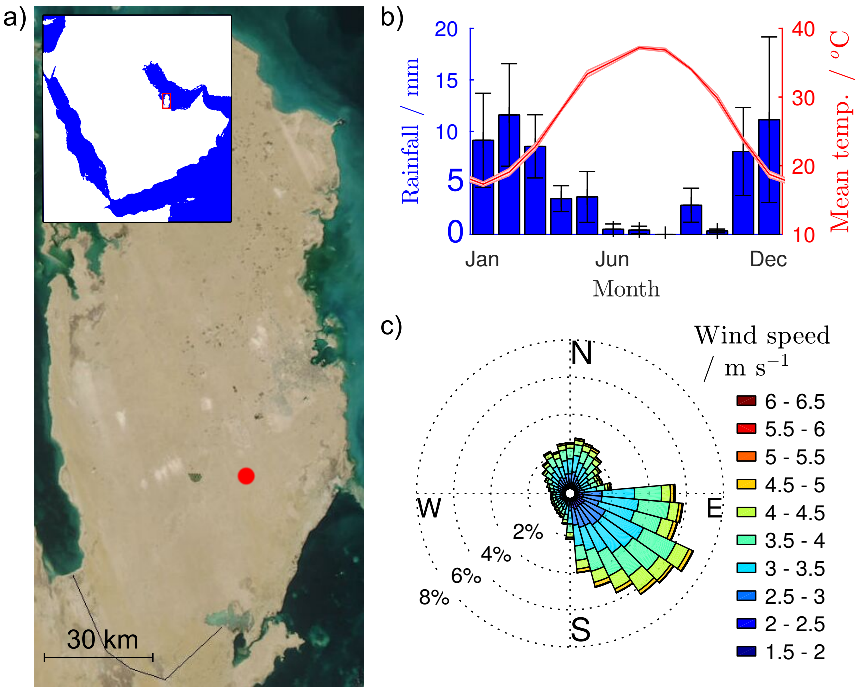

Figure 4.3: Location and climate of field site. The location of the field site within Qatar is indicated on a satellite image (a), courtesy of NASA. The site has a hot desert climate, as indicated by monthly average temperatures and total precipitation (b). Error bars and regions represent standard error over 6 years of meteorological measurements, conducted from 2010 to 2015 at Al Udeid Air Base, 5 km from the field site, and obtained courtesy of Weather Underground. A wind rose (c) indicates the distribution of 10-minute-averaged wind speeds and directions, measured at a height of 2.52 m above the desert floor, at a weather station on the field site, from November 2011 to April 2014. This data is courtesy of Michel Louge.

Sediment is supplied to the site from dunes further upwind, with quartz grains comprising 79 ± 6% by volume, calcium carbonate grains 8.9 ± 1.1%, and feldspar grains 7 ± 7% [4, 128][c]. Gypsum, chert, and trace quantities of heavy minerals are also present, predominantly in the form of small grains [236]. Most grains originate from the deposits of the Tigris and Euphrates rivers, which were accessible during the last glacial period due to lower sea levels [128, 203], and prolonged aeolian transport has resulted in these grains becoming well-rounded, with a narrow size distribution [22]. More angular grains originate from weathering of the exposed desert floor, which consists of dolomitic limestone from the mid-Eocene Dammam formation [6]. Due to the low supply of sediment and the predominantly unidirectional wind, the dune field consists of isolated barchan dunes, separated by this exposed, rocky desert floor.

I study four dunes, pictured in figure 4.4 and denoted A, B, C, and D. These dunes have been extensively studied by a multidisciplinary research group led by Prof. Michel Louge, thanks to whom all four dunes have been surveyed with a Leica TS02 theodolite. Dune A was surveyed repeatedly from 2011 to 2017 and dune B in January 2015 and January 2017, whilst dunes C and D were surveyed in January 2017. From these surveys, the heights of dunes can be calculated, with dune A having a height of 5.1 ± 0.3 m, B a height of 28 ± 2 m, C a height of 3.14 ± 0.06 m, and D a height of 6.0 ± 0.2 m. The repeated surveys also allow dune migration rates to be calculated, with A migrating at 18.4 ± 0.1 m yr^{-1} and B at 5.0 ± 0.5 m yr^{-1}.

This dune migration occurs through avalanches on the dunes' slip faces, as discussed in chapter 1, and it is the strata emplaced by these avalanches that I investigate. I extract sand samples during two field expeditions in January 2015 and January 2017. For each expedition, I spent four days in the field and extracted samples of sand in two ways. In 2015, I used an 'aquarium' device to extract volumes of sand from within the dune, while preserving their internal structure, as well as a 'comb' device to extract grains of sand from different depths within individual strata. In 2017, I used the comb device again, as well as a modified version that I'll refer to as the 'fine-toothed comb'. In addition to the samples I extracted, I analyse samples extracted by a collaborator, Anthony Hay, during a field expedition in January 2016. The positions on the dunes from which samples were extracted are indicated in Fig. 4.4 and listed in Appendix C, Table C.2, while the devices for sample extraction are described in sections 4.2.2, 4.2.3, and 4.2.4, below.

---

[c] Volumetric composition is estimated by averaging the measurements of Al-Ansary et al. [4], by X-ray diffractogram, and those by grain counting, of Garzanti et al. [128].

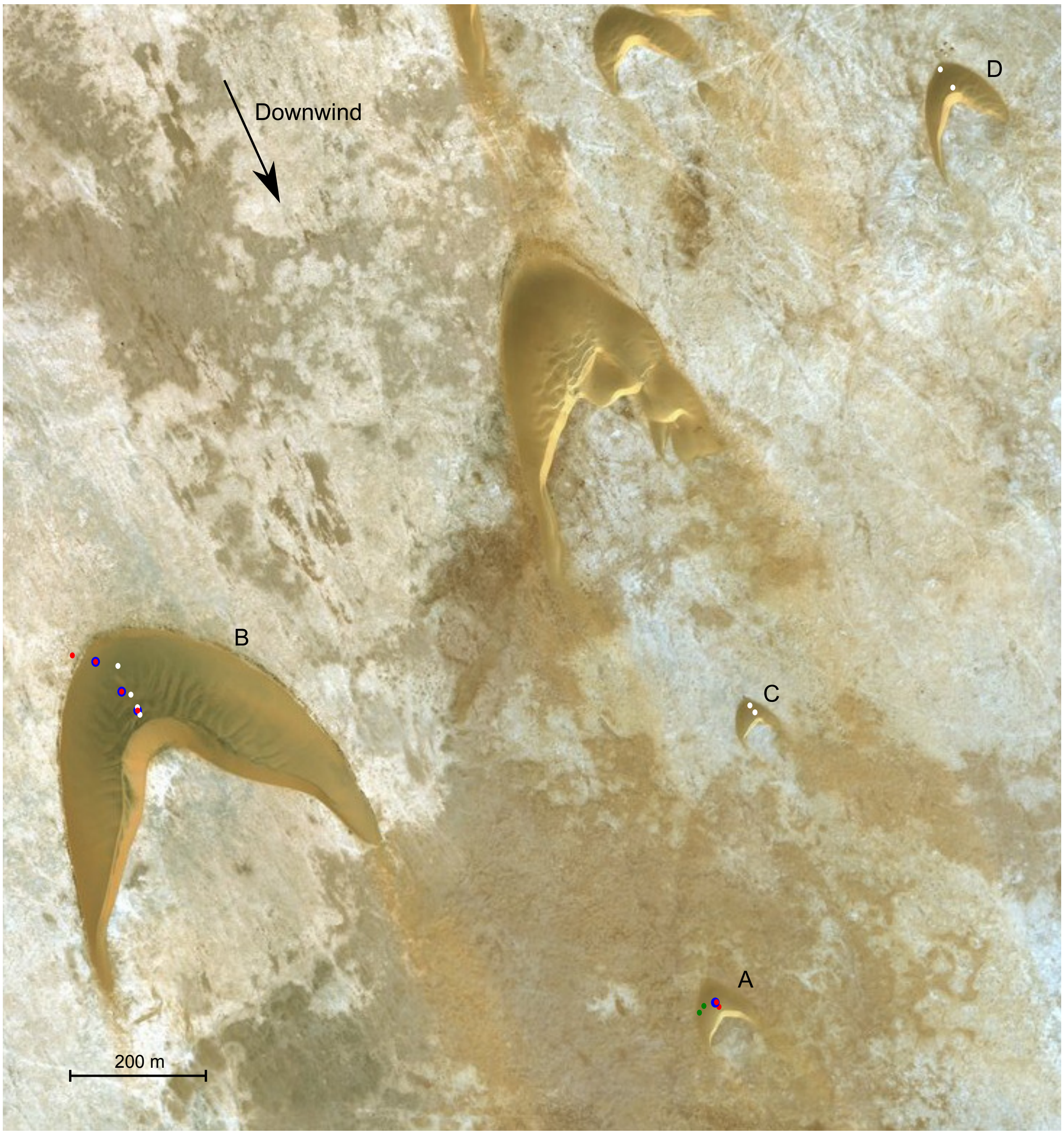

Figure 4.4: Annotated satellite image of field site. The four dunes that I study are visible at bottom-right, left, right, and top-right, and are labelled. An arrow indicates the direction of net sediment transport, downwind. The locations at which samples were taken on each dune, relative to that dune's brinkline's summit, are indicated with dots. These are coloured red for samples taken in 2015 with the 'aquarium' device, blue for samples taken with the 'comb' device in the same year, green for samples extracted with the 'comb' device in 2016, and white for samples taken in 2017, when both the 'comb' device and the 'fine-toothed comb' device were used at each location. The satellite image is a composite of two images, taken on the 3rd of June 2015 and the 1st of February 2016, and is courtesy of DigitalGlobe and Esri.

4.2.2 'Aquarium' device

The aquarium consists of a cuboidal box of 1 mm-thick steel sheet, with dimensions 300 mm by 150 mm by 20 mm and with removable top, bottom, and front panels (Fig. 4.5a). The top and bottom panels are silicone-coated, to allow a water-tight seal. In 2015, samples were taken from the locations indicated in red in Fig. 4.4 and listed in Appendix C, Table C.2.

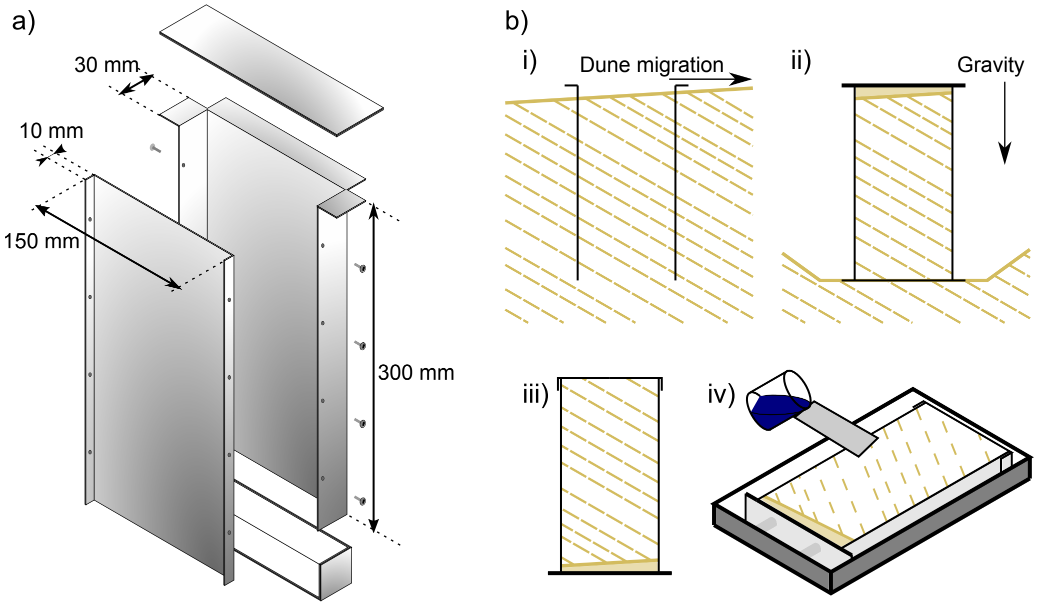

Figure 4.5: The 'aquarium' device (a) and its use (b). The aquarium is constructed from 1 mm-thick steel sheet, as presented in exploded, isometric view (a), and is used to extract samples with undisturbed internal structure (b) via insertion into the dune (i), sealing at top (ii) and bottom (iii), and resination in a custom-built jig (iv).

The process of extracting samples is schematically depicted in Fig. 4.5b. The top and bottom panels of the aquarium were removed and the aquarium was inserted vertically into the dune surface with its longest axis vertical and shortest axis perpendicular to the dune's migration, capturing a cuboidal sand core. After excavation of the sand surrounding the aquarium, a silicone-coated plate was inserted to cover the bottom opening; neutral sand was added via the top opening to ensure tight packing; and the top panel was clamped in place. The enclosure and tight packing of the sand sample permitted the aquarium to be overturned without loss or disturbance of sand, following which the bottom panel was put in place.

Once all panels were in place, the aquarium was laid in a custom-built jig, levelled so that the front panel faced exactly upwards and clamped in place to ensure a tight seal. The front panel was then removed. 450 ml of LR White acrylic resin was mixed with accelerator and poured over a three-minute interval into the aquarium. A metal plate was used as a channel for the resin, to ensure full infiltration of the sand core without formation of air bubbles or inertial disturbance of the sand surface. After 24 hours, the solid sand core was extracted from the aquarium and could be transported.

To analyse aquarium samples, they were first cut along their width into sixteen 9 mm-wide sections and an offcut, using a geological slab saw. Each 300 mm by 20 mm exposed face was then imaged using an Olympus BX51 microscope, at 5× optical magnification with reflected darkfield illumination, in a longitudinal strip 1.65 mm wide and the entire length of the section, consisting of 2080 × 1542 pixel images with a resolution of 1.073 pixels per micron. Grain cross-sections were clearly visible on the resulting images, indicating composition mainly of rounded but imperfect quartz grains, as in Fig 4.6.

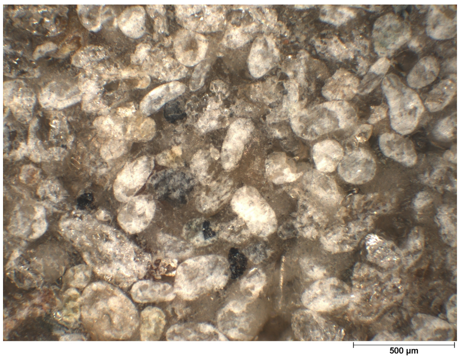

Figure 4.6: Microscope image of a section of a sample extracted using the aquarium device. Grain cross-sections are visible, but cannot be accurately segmented from the resin in which they are emplaced.

However, my attempts to automatically analyse images failed to effectively segment them into grain cross-sections and so failed to accurately extract the distribution of grain cross-sectional areas visible in such images. Details of this failure are in Appendix E, section E.3. The transformation from the distribution of visible grain cross-sectional areas to the distribution of grain diameters is highly sensitive to unidentified grain cross-sections, as described in section C.1 of Appendix C, and so I was unable to automatically extract grain-size distributions from the aquarium samples. At the same time, identification of grain cross-sections by hand is far too time-consuming for such analysis to be feasible. Possible paths forward are described in section 4.5.

4.2.3 ‘Comb’ device

The comb consists of 2 mm-thick acrylic plates, glued together to form seven adjacent sections of length 50 mm long, depth 50 mm, and width 5 mm (Fig 4.7a). The locations at which samples were taken in 2015, 2016, and 2017 are indicated in blue, green, and white, respectively, in Fig. 4.4 and are listed in Appendix C, Table C.2.

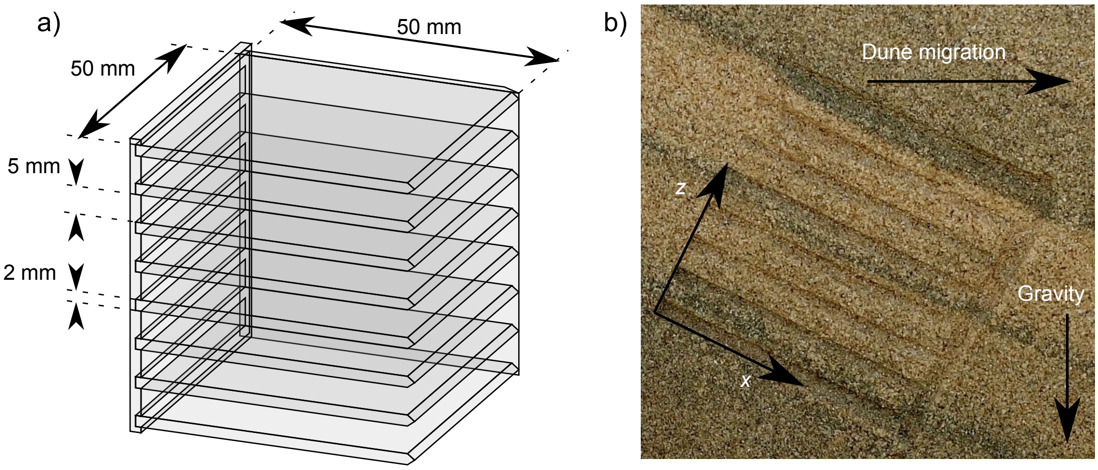

Figure 4.7: The ‘comb’ device (a) and its use (b). The comb is constructed from 2 mm-thick acrylic plates, as presented in dimetric view (a), and is used to extract unconsolidated samples from different depths within individual strata. The comb is inserted horizontally into a face exposed by excavation, aligned with strata that are made visible by the preferential permeation of blue-dyed water (b). I define coordinates x downwards along stratigraphy and z vertically across it.

To take samples with the comb, 8 to 12 l of water was dyed blue with food dye and slowly poured onto an area of approximately 0.1 m^2, on the surface of the dune. After 20 minutes, I excavated a pit adjacent to the wetted sand, with a vertical face parallel within 10° to the dune’s direction of migration. The blue-dyed water both increased the cohesion of the sand, permitting successful excavation, and marked the pattern of permeation within the dune. I used a metal plate to straighten this face, revealing clear penetration of water along stratigraphy. The comb was inserted horizontally into this exposed face, with section boundaries aligned with the visible cross-strata (Fig. 4.7b). Consequently, each of the seven comb sections was filled with a sand sample from a different depth within the stratigraphy, of volume approximately 12 ml. Having used metal plates to retain these samples within the comb during its extraction, I decanted these samples into sample tubes for analysis.

For those samples from 2015 and 2016, grain-size distributions were analysed using a

Malvern Instruments Mastersizer 2000, with wet dispersion. Assuming spherical grains, this calculated via laser diffraction the proportion by volume of grains in half ϕ intervals between -1ϕ and 15.5ϕ, or equivalently with diameter in geometrically-spaced bins with ratio $\sqrt{2}$ between 0.021μm and 2000μm. Aeolian dune sand is expected to have high smoothness and sphericity and to be well-sorted, with individual populations having approximately lognormal distributions[103, 316]. For such samples, the instrumentation calculated volume-weighted mean grain diameter $d_{4,3}$ to better than 1% [222].

The comb samples from 2017 have not been analysed, due in part to the equipment problems described in Appendix E, section E.3.

4.2.4 ‘Fine-toothed comb’ device

The fine-toothed comb consists of a solid steel base, into which six 1 mm-thick steel plates are fixed to form sections of length 300 mm, depth 30 mm, and width 2 mm (Fig. 4.8). Samples were taken in 2017, from the locations indicated in white in Fig. 4.4 and listed in Appendix C, Table C.2. The process of sample extraction was the same as that for the comb device, described in section 4.2.3.

For a selection of samples from the fine-toothed comb, grain-size distributions were measured by Jean-Luc Métayer at the Institut National des Sciences Appliquées de Rennes. Each sample was separated into five fractions by size, with each fraction deflocculated using sodium hexametaphosphate and an ultrasound bath, before the volumetric grain-size distributions of each fraction were measured using laser diffraction. This permitted measurement of the very low proportions by volume of the smallest-sized grains, which have a disproportionately large effect on the permeation of water. In addition, the resolution of measurements was higher than using the Mastersizer 2000, since the bins into which grains were divided by effective diameter had geometric ration ≈ 1.07. However, those grains that did not pass through a sieve of aperture 0.5 mm were not included in analyses.

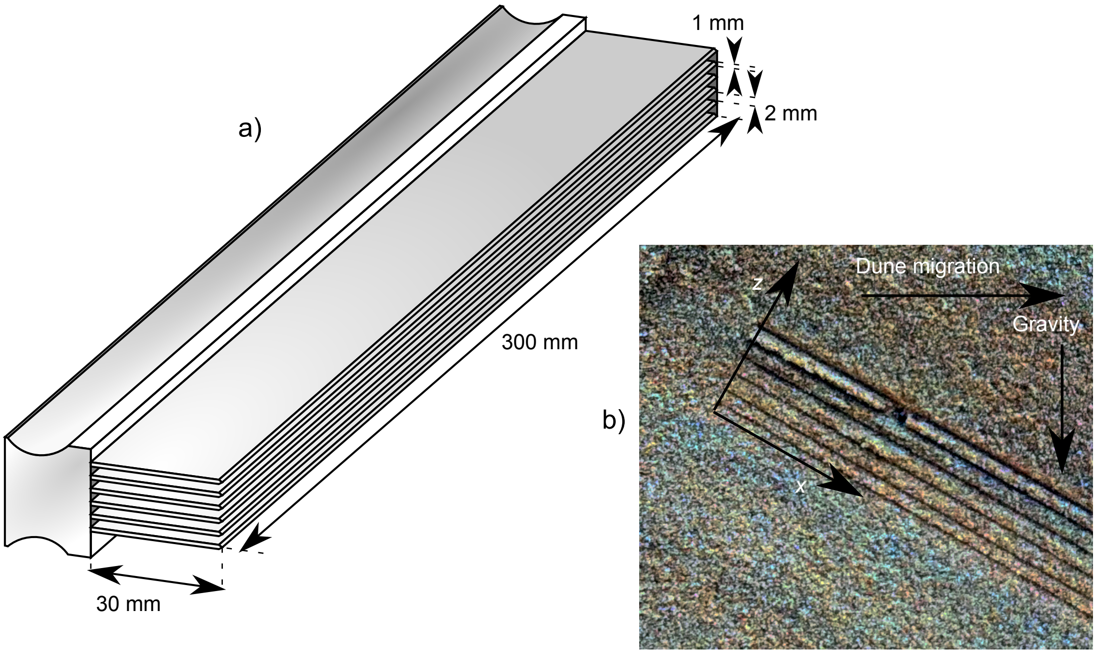

Figure 4.8: The 'fine-toothed comb' device (a) and its use (b). The fine-toothed comb is constructed from 1 mm-thick steel plates fitted into a steel baseplate, as presented in dimetric view (a), and is used to extract unconsolidated samples from different depths within individual strata, at high depth-resolution. The comb is inserted horizontally into a face exposed by excavation, aligned with strata that are made visible by the preferential permeation of blue-dyed water (b). I define coordinates x downwards along stratigraphy and z vertically across it. To illustrate strata in b, white balance is corrected, saturation increased, and brightness decreased.

4.3 Results

4.3.1 Qualitative results

On all the dunes that I study, the excavation of pits exposes strata which are associated with the differential permeation of water (Fig. 4.9). These strata are from two of the classes described by Hunter [163] and introduced in section 4.1.3: climbing translatent strata and sandflow cross-strata.

In a thin layer at the surface of each dune, excavation exposes climbing translatent strata, formed of grains that last moved as a result of aeolian transport between surficial ripples. Each stratum is approximately 1 mm thick and climbs at an angle of 5 to 10° with distance downwind, approximately parallel to the surface. The layer in which such strata are found is of an approximately constant thickness, of approximately 1 cm, over the majority of each dune's surface, but widens close to each dune's crest. In the two pits within 10 m of the crest of dune

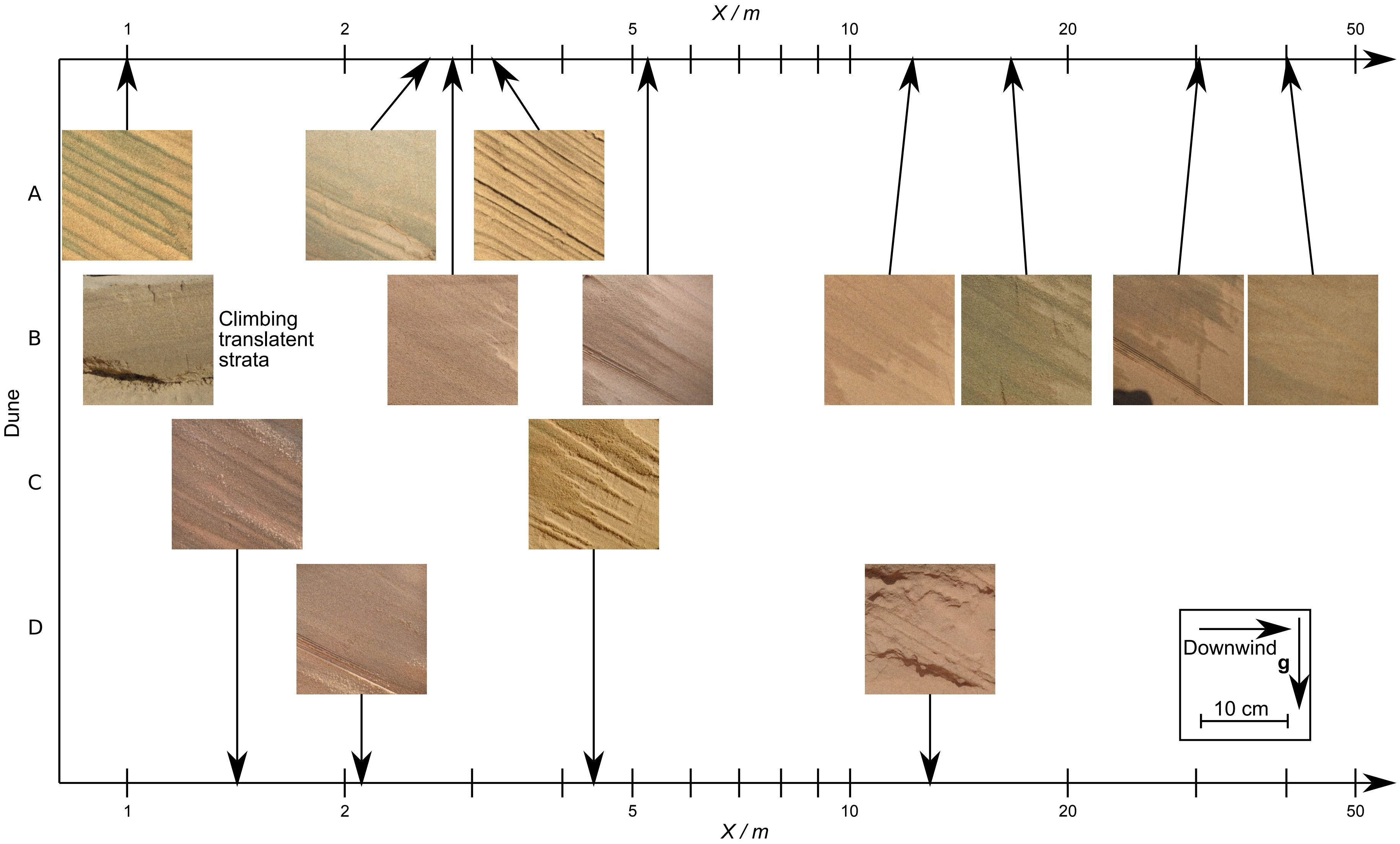

Figure 4.9: Examples of strata exposed in pits, corresponding to different downslope deposition distances X. Photographs are taken of the exposed vertical faces of pits, at locations detailed in section C.2 of Appendix C, using a Sony RX-100 camera, an iPhone 6, a Fairphone 2, and a Motorola MotoG3, all handheld and subject to errors in orientation. Scale, indicated in an inset at bottom-right, is inferred from metre rules included in the original photographs.

B, dug in 2015 and 2017, this layer was approximately 10 cm thick while, in the pit dug within 10 m of dune D's crest, the layer thickness was approximately 5 cm. Water tends to permeate along climbing translatent strata and so, being parallel to the dune's surface, they tend to inhibit the permeation of water to the dune's bulk.

Within this bulk, excavation exposes the sandflow cross-strata discussed in chapter 3. Having been emplaced by avalanches on former slip faces of the dunes, these strata dip at an angle of 30.0 ± 0.5° with distance downwind, consistent with the 30.1 ± 0.2° angle of repose of the current slip faces. Water preferentially permeates at this dip angle, along defined depths within each stratum, permitting deeper penetration into each dune and resulting in a pattern of water content determined by the widths of strata. These widths are of order centimetres and are variable within each pit.

Given the implications of chapter 3 for stratum width, I estimate for each pit the distance X that exposed grains avalanched down the former slip face before being deposited, with calculations described in section C.2 of Appendix C. At the same values of X, the pattern of stratigraphy appears to be the same on different dunes, supporting the suggestion in chapter 3 that the mechanism of avalanche-induced stratification on a slope is independent of the length of that slope. However, whilst stratum width appears to increase with X, this increase appears to be slower than the linear increase suggested by chapter 3. This may be a genuine effect, with grain-remobilisation or cross-slope variation preventing the results of chapter 2 from being directly applicable, or it may be an artefact resulting from the difficulty in identifying every stratum in photographs. For a more quantitative and more robust investigation of individual strata, I consider measurements of grain-size distributions.

4.3.2 'Comb' sample grain-size distributions

I first consider the shape of the grain-size distributions of those samples taken using the 'comb' device, in 2015 and 2016, on dunes A and B. Using a G-test at the 5% significance level, the measured grain-size distributions of samples from dune B are consistent with the underlying distributions being lognormal ($p = 0.173$). An example of this agreement is shown in Fig. 4.10a. For samples from dune A, however, grain-size distribution measurements are inconsistent with the underlying distribution being lognormal ($p < 10^{-10}$), with lack of agreement apparently due to the deficit of large grains exemplified in Fig. 4.10a.

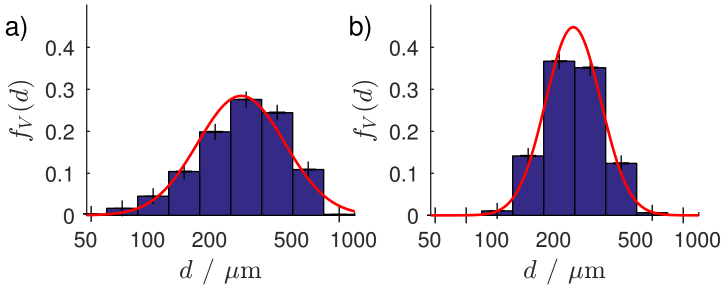

Figure 4.10: Typical grain-size distributions in comb samples from dune A (a) and B (b). The red curve represents the maximum-likelihood lognormal fit to the measured data. Errorbars correspond to standard error over three laser diffraction measurements of the same sample.

Despite this deviation from lognormality, grain-size distributions are typical for aeolian dune sand: narrow, with diameters centred around approximately 250 μm, unimodal, and approximately symmetrical. Using the Folk and Ward classification [116, 117], all samples consist of well-sorted or moderately-sorted fine or medium sand, with distributions near-symmetrical and mesokurtic. The important properties of each sample can therefore be described by two statistics, of location and shape.

The two statistics that I use to describe each grain-size distribution are the volume-weighted median grain diameter d_{50} and the ratio d_{84}/d_{16} between the 84th and 16th percentiles of the volume-weighted distribution of grain diameters. These statistics have clear physical relevance, with d_{50} being the typical diameter of a grain selected at random from a volume and d_{84}/d_{16} being the typical ratio between the diameters of a large grain and a small grain selected in the same manner. They are robust, easy to describe, and direct functions of the 'phi-value' statistics that are conventional in sedimentology [116, 117]. For a lognormal distribution of micron-expressed grain diameters, with location parameter μ and shape parameter σ, $d_{50} = \exp(\mu)$ and $d_{84}/d_{16} = \exp(1.99\sigma)$, respectively.

It is to be expected that, in each stratum, d_{50} will increase with cross-stratigraphy height z and with downslope deposition distance X, due to the size segregation discussed in chapter 3. d_{84}/d_{16} will decrease with X, as size segregation becomes more complete down former slip faces, and will be high both in the middle of each stratum, where segregation is incomplete, and wherever the comb has insufficient resolution to clearly separate strata.

Of the two hypothesised relationships with X, analysis of the data provides evidence only for the decrease of d_{84}/d_{16} with X (Fig. 4.11a). d_{50} varies significantly but inconsistently with X, indicating that the variation in typical grain size between different strata is larger than such variation along or within each stratum. This implies that, over large scales within a dune, variation in grain size is significant but arises predominantly through differential transport of grains to the dune, by the wind, rather than through differential transport of grains down the dune's slip face, by segregation in avalanches. However, this avalanche-induced segregation does affect grain-size distributions, with d_{84}/d_{16} negatively correlated with X. This decline suggests that segregation results in a significant narrowing of local grain-size distributions downslope and hence lower within dunes, relative to their brinklines.

No such segregation-induced trend is evident across strata. In Fig. 4.11b, I plot the typical grain size d_{50} of each sample against the height across stratigraphy z at which the sample was taken, for one example of sandflow cross-strata from dune A, one example of sandflow cross-strata from dune B, and one example of climbing translatent strata from dune B. Across the approximately 1 mm-wide climbing translatent strata, each sample consists of sand from multiple strata and so any variation of d_{50} between samples is due solely to variation in sand supply at different times of deposition. Across the sandflow cross-strata, measured values of d_{50} vary significantly with z, but the pattern of this variation is not that implied by avalanche-induced size-segregation: gradual increases with height within each stratum and sharp decreases between the top of one stratum and the bottom of another. Instead, such variation appears to be random, with a magnitude approximately that of the supply-associated grain-size variation between different climbing translatent strata.

Since systematic grain-size variation across sandflow cross-strata is well-attested in the literature (see section 4.1.3), I associate the failure to measure such variation with two methodological flaws: the use of a sampling device with insufficient vertical resolution and the failure to measure volumetric grain-size distributions more sensitively. As a result of the first flaw, many strata are under-resolved vertically (Fig. 4.12), so that the measured variation of d_{50} with z results from inter-stratum differences due to varying sand supply, rather than intra-stratum variation due to size-segregation in avalanches. As a result of the second, I am unable to measure the very small contributions to samples' volumes of the smallest grains, which are disproportionately important in distinguishing strata and in affecting the permeation of water.

For the next field expedition, I therefore designed the higher-resolution, fine-toothed comb

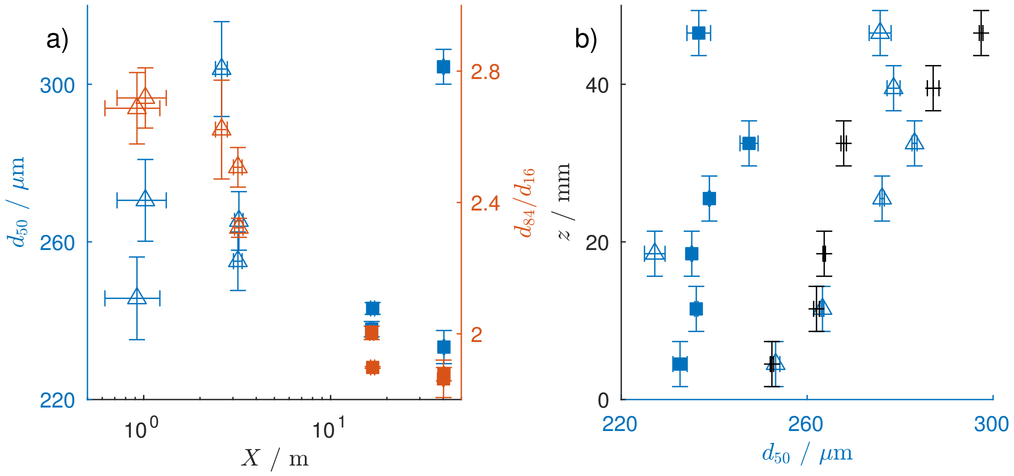

Figure 4.11: Variation of typical grain diameter d_{50} and typical large/small grain diameter ratio d_{84}/d_{16} with deposition distance downslope X (a) and height within stratigraphy z (b). In panel a, all samples are represented, from both dune A (△) and dune B (■), whilst panel b shows data from one sample extraction from sandflow cross-strata on dune A (△) and one extraction from sandflow cross-strata on dune B (■), compared to controls extracted from climbing translatent strata (+). Error bars in X correspond to uncertainty in my estimates and those in z correspond to the resolution of the comb device's sections. Error bars in grain size statistics represent standard error. In panel a this is calculated across all samples from each comb extraction, representing within-stratum variation, whilst in panel b error is calculated across three laser diffraction measurements of each sample, representing measurement error.

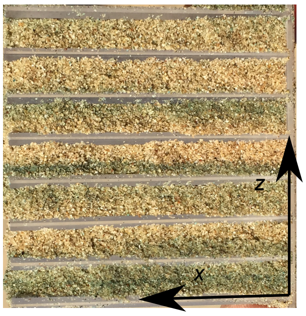

Figure 4.12: Photograph of samples after extraction but before decantation, demonstrating under-resolution. The samples were extracted and the photograph taken by Anthony Hay.

and arranged, with collaborators Michel Louge and Alexandre Valance, to have samples measured by Jean-Luc Métayer, who uses a measurement procedure able to detect the very small proportions of samples' volumes that consist of the smallest grains.

4.3.3 'Fine-toothed comb' sample grain-size distributions

For a sample extracted at position $\boldsymbol{x}$, I define $F_V(d;\boldsymbol{x})$ as the proportion of the sample's volume that consists of grains with diameter less than d and I let $f_V(d;\boldsymbol{x}) = \partial F_V/\partial d$ be the associated probability density function. As samples from the fine-toothed comb are measured by Jean-Luc Métayer using the procedure described in section 4.2.4, the measured distributions F_V are more precise and have higher resolution than the distributions discussed in the previous section, for $d < 500$ μm. The question is then what functional of $F_V(d)$ will be most closely associated with the permeation of water through the dune. Considering the sampling method discussed in section 4.2.4 and the analysis in section C.3 of Appendix C, I elect to use the Sauter mean diameter

$$D_{3,2}(\boldsymbol{x}) = \left[\int_0^\infty d^{-1} f_V(d;\boldsymbol{x})\mathrm{d}d\right]^{-1}. \tag{4.2}$$

To verify that estimates of the Sauter mean diameter are valid, I consider the relative contribution of differently-sized grains to its inverse, $D_{3,2}^{-1}$ (Fig. 4.13). Uncertainty is low for those grain sizes that significantly affect $D_{3,2}$ and, extrapolating from the observed decay in relative contributions at high d, the neglected grains of diameter greater than 500 μm have a negligible effect on $D_{3,2}$. Instead, the Sauter mean diameter is mainly determined by grains with diameters of order 1 μm and of order 100 μm, with the two different populations having approximately equal influence. It should be noted that the population of smaller grains will have a volume more than a hundred times smaller than that of the population of larger grains, so that the analysis of section 4.3.2 would entirely neglect the small-grained population's effects on water permeation.

Using $D_{3,2}$, instead, reveals an association between grain-size distributions and the permeation of water. From photographs taken immediately prior to the extraction of samples (e.g. Fig. 4.14a), I record the samples into which more water has permeated. Indicating these samples on plots of $D_{3,2}$ against z (Fig.s 4.14b-d) suggests that water preferentially permeates along regions of each stratum in which grain sizes are lower, as predicted by the analysis of section C.3 in Appendix C.

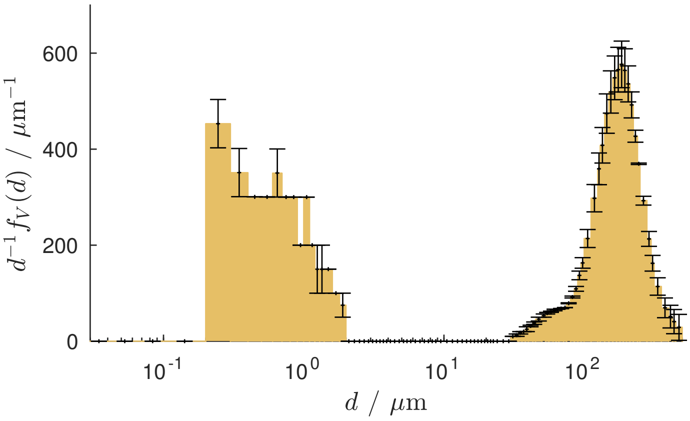

Figure 4.13: Example of relative contributions of grains of different sizes to the inverse of the Sauter mean diameter. The plot is produced for a position $\boldsymbol{x}$ on dune B with $X = 12.20 \pm 0.12$. Errorbars represent standard error between two samples from the same $\boldsymbol{x}$, from two extractions using the fine-toothed comb.

4.4 Discussion

The results from fieldwork are mixed and frequently unclear. On the exposed, vertical faces of pits, the visibility of strata varied, preventing anything more than qualitative speculation about the relationship between the mean widths of avalanche-emplaced strata $\bar{Y}$ and the distances down former slip faces X at which such strata were emplaced. Samples taken with the 'aquarium' device of section 4.2.2, which offered grain-scale resolution of grain-size distributions across 25 cm of stratigraphy, proved impossible to analyse. Those taken with the 'comb' device of section 4.2.3 proved to be spaced too widely across stratigraphy to resolve individual strata (Fig.s 4.11, 4.12), while the method chosen to analyse them was unable to detect the micron-scale grains that section 4.3.3 demonstrated to be significant for the permeation of water. Samples taken with the 'fine-toothed comb' device could not be compared to those taken with the comb device, as grains with diameters above 500 μm were neglected, and the number of samples that could be analysed was limited both by the expense of having measurements taken by Jean-Luc Métayer and by delays imposed by his limited availability.

However, this work strengthens the association between the preferential permeation of water along stratigraphy and variation in grain-size distributions within dunes, arising from size-segregation of grains within slip-face avalanches. By adding blue-dyed water to a range of positions on a variety of barchan dunes' surfaces and by subsequently excavating pits, I

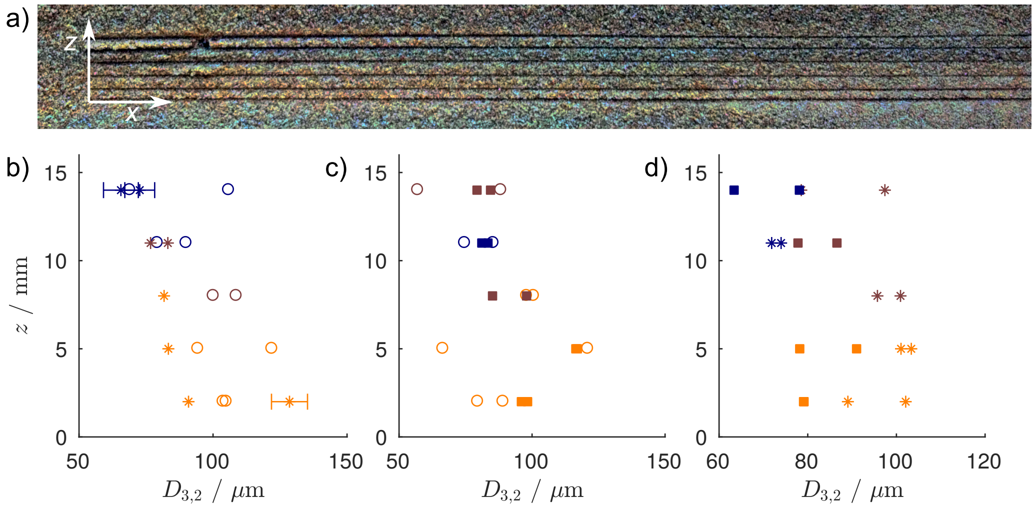

Figure 4.14: Photographs of strata sampled with the fine-toothed comb (a) demonstrate an association between water content and the Sauter mean diameter $D_{3,2}$ **(b).** Before the extraction of each set of samples, I use the fine-toothed comb to make an imprint of sample boundaries on the exposed, vertical pit face, which I then photograph. Panel a is an example of such a photograph, taken at $X = 5.25 \pm 0.10$ m on dune B and enhanced to allow wet, blue-dyed samples to be distinguished. These wet samples are indicated in blue in panels b to d, while dry samples are orange and intermediate samples brown. Symbols distinguish samples from dune B (■), C (○), and D (∗), while panels b, c, and d correspond to samples taken at $X \approx 2$ m, $X \approx 5$ m, and $X \approx 12$ m, respectively. Errorbars, where present, represent standard error between repeated measurements by Jean-Luc Métayer.

demonstrate clearly preferential permeation of water along certain heights within Hunter's avalanche-emplaced 'sandflow cross-strata'. As these cross-strata are present within the majority of each dune's bulk, this preferential permeation provides a mechanism for water to permeate deep into the dune, as suggested by previous authors.

Furthermore, I confirm the relations that previous authors have suggested between macroscopic position within a dune and grain-size distributions. Having extracted surficial samples from different areas of dunes, these authors have found that average grain-size increases with distance down a dune's slip face, while the width of grain-size distributions narrows [22, 204, 205, 215, 273, 298]. In dunes A and B, the latter relation holds. However, changes in the sand supplied to each dune result in variation in typical grain size between different strata that is larger than such variation along a single stratum. Consequently, median grain size d_{50} within a sand sample does not increase significantly with the distance downslope X at which that sand was deposited. Previous authors' samples were extracted from approximately equal depths and so will have consisted of sand deposited at approximately the same times, allowing significant downslope coarsening to be observed.

Finally, I provide quantitative evidence that water preferentially permeates along regions of strata in which grains are smaller. This is consistent with the observations of McCord et al. [227] and Berndtsson et al. [34], who suppose preferential permeation to be driven by increases in permeability K due to pre-wetting, because smaller grains are associated with higher capillary potential Ψ and so will have a higher water content even before I add blue-dyed water to the dune's surface. The concentration of water in regions in which grains are smaller and Ψ higher decreases the likelihood of water being displaced by evaporation, increasing its residence time within dunes.

These three effects indicate the viability of dune stabilisation by bacterial action and revegetation. Water is able to permeate within the dune, along the regions of avalanche-emplaced strata in which grains are smaller. That local grain-size distributions narrow with depth implies that such regions of small grains exist throughout the depth of the dune, so that water can reach significant depths within the dune. The concentration of water at regions of high capillary potential Ψ then decreases the likelihood of such deep water being displaced. Consequently, water will be available to bacteria in concentrated regions deep within the dune, permitting bacterial dune stabilisation.

4.5 Recommendations

I recommend the following extensions to this work:

- Find a more effective dye for the resin used in the extraction of samples with the aquarium device, so that grains can more easily be distinguished in cross-sections.
- Develop a more effective technique for extracting the cross-sectional areas of grains from cross-sections of aquarium device samples, since this offers the highest-resolution method for investigating grain-size distributions.
- Analyse grain-size distributions of the samples extracted in the 2017 field expedition with the comb device, to verify that the trends observed in Fig. 4.11a hold on different, individual dunes and are not an artefact of the small-X and large-X samples originating from different dunes.
- Analyse grain-size distributions of more samples extracted with the fine-toothed comb device and repeat more existing analyses, to verify the association between small grains and higher water content indicated in Fig. 4.14.
- Use a combination of the above to measure the widths of avalanche-emplaced strata within dunes, to test the implication of chapter 3.

Simulated surface-wave scattering by an isolated barchan dune
Surface waves propagate to the dune, are transmitted to its interior, lose coherence through internal reflections, and are reemitted. This process is demonstrated by surface plots of vertical displacement at times *t* = 0, 0.2, 0.6, and 2.4 s, in response to a point force centred at time *t* = 0 s.

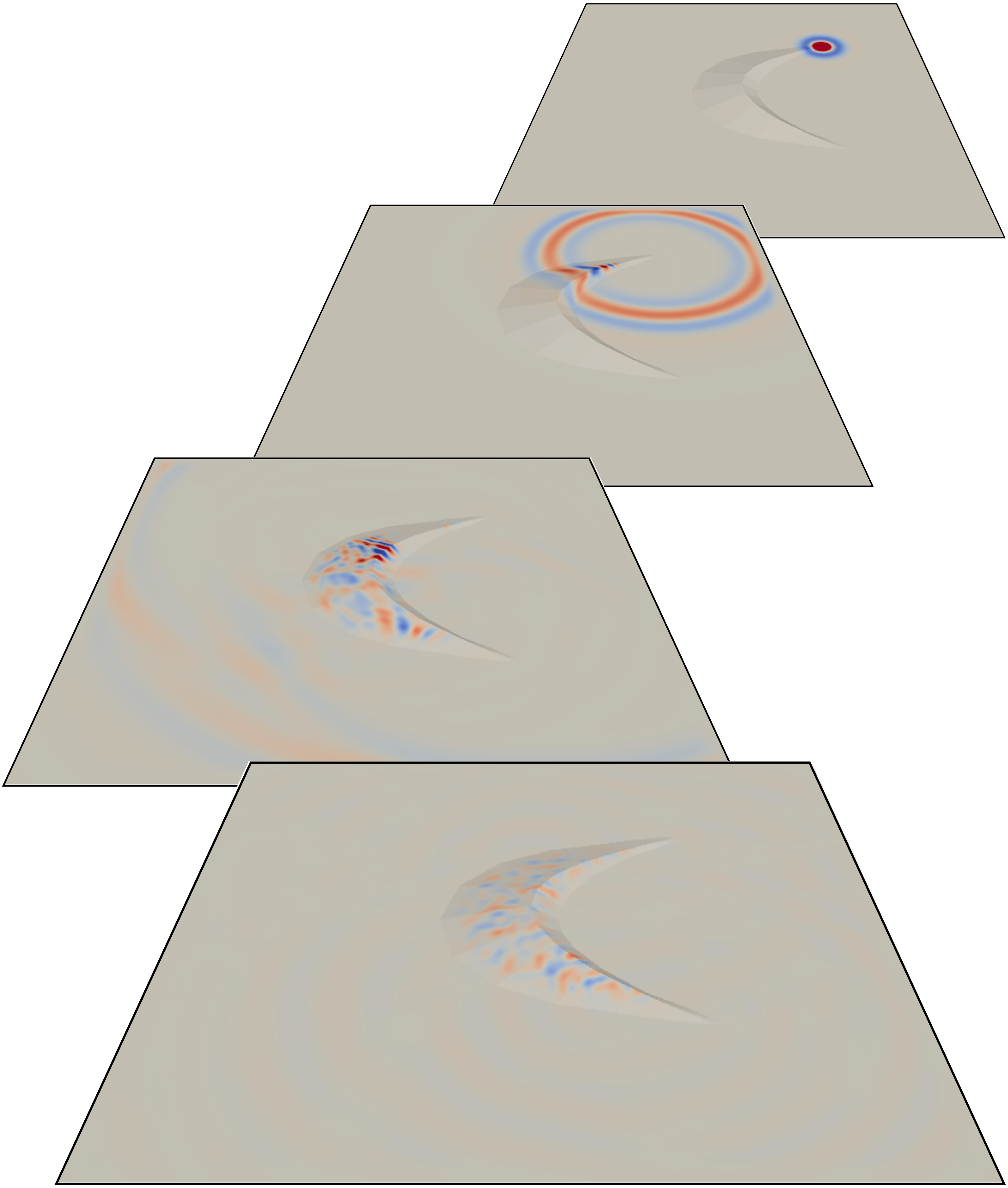

CHAPTER 5

The effect of sand dunes on seismic surveys

‘[A]lmost passing belief are the stories related of these spirits of the desert, which are said at times to fill the air with the sounds of all kinds of musical instruments...’

Marco Polo, *Il Milione*, tr. W. Marsden

Abstract

Ground roll is a significant source of noise in land seismic data, with crossline scattered ground roll particularly difficult to suppress. This noise arises from surface heterogeneities lateral to the receiver spread, and in desert regions sand dunes are a major contributor. However, the nature of this noise is poorly understood, preventing the design of more effective data acquisition or processing techniques. Here, I present numerical simulations demonstrating that a barchan sand dune acts as a resonator, absorbing energy from ground roll and reemitting it over an extensive period of time. I derive and validate a mathematical framework that quantitatively describes the properties of the emitted waves, and demonstrate that wave amplitude is estimable from easily-measurable bulk properties of the dune. Having identified regions in time, space, and frequency space at which noise will be more significant, I propose reducing dune-scattered noise through careful survey design and data processing. In particular, I predict that seismic noise will be lower upwind of barchan dunes, and at frequencies far from a ‘resonant’ frequency $2c_S/H$, for dune height H and typical seismic velocity within the dune c_S. This work is especially relevant to seismic acquisition in the vicinity of a dune field, where scattered noise appears incoherent and difficulties arise with alternative approaches to noise suppression.

The work described in this chapter was conducted at the Schlumberger Gould Research Center, Cambridge, UK, under the supervision of Dr. Everhard Muyzert, within the framework of a CASE studentship. Text and figures are substantially derived from a manuscript published in the Journal of Geophysical Research: Solid Earth 123, 5th June 2018, titled Seismic Ground Roll Absorption and Reemission by Sand Dunes and with the authors Matthew I. Arran, Nathalie M. Vriend, and Everhard Muyzert. DOI: 10.1029/2018JB015580.

5.1 Introduction

Seismic reflection surveys are a key tool in the exploration of the Earth's subsurface. Their use in inferring geology dates to the 1917 patent of Fessenden [112] and the current, annual value of the market for seismic surveys on the land surface has been estimated to be in excess of \$2 bn, mostly arising within the petroleum industry [291]. In such surveys, explosives, falling weights, or seismic vibrators generate seismic waves, which propagate through the Earth and are reflected by geological boundaries. By measuring surface motion and detecting these reflected waves, the subsurface geology can be inferred. However, seismic surveys in dune fields are susceptible to noise.

Sand dunes cause noise in seismic surveys by scattering surficial Rayleigh waves ('ground roll'). When surface sources are used in the acquisition of land seismic data, as in vibroseis and weight-drop surveys, approximately 2/3 of the energy delivered by the source propagates along the Earth's surface in the form of such waves [232, 256], which are reflected or refracted where topography or seismic velocity at the surface varies [161, 209]. Since desert sand dunes are associated with topographical variation of tens or hundreds of meters and with considerably lower seismic velocities than surrounding bedrock [11, 315], these dunes will reflect seismic signals on arrival, and absorb seismic energy that is subsequently reemitted over time [75, 95, 212]. This scattered energy will propagate to the seismic receiver spread as seismic noise, with again the preponderance of energy transmitted by surface waves. For distance traveled r, the amplitude of surface waves decays as $r^{-1/2}$ while the signal of interest is carried by body waves with amplitude decaying as r^{-1}, so the amplitude of this noise can be significantly higher than that of the signal, seriously degrading the quality of seismic data.

Established approaches often struggle to suppress this noise. Common workflows in hydrocarbon exploration include high-pass filters for frequency or apparent velocity, or multidimensional filters in frequency-wavenumber or 'τ-p' space, where p is the inverse of the apparent velocity and τ is the inferred time at which waves passing receivers would have been emitted at the source, assuming direct propagation [70, 105, 160, 183, 311]. These rely on the assumption that ground roll is much more strongly attenuated at high frequencies than the signal of interest, or that it propagates along the line of receivers as opposed to arriving at all of them almost instantaneously, or that it travels directly from the source and so has $\tau \approx 0$. However, there is significant overlap between the frequency range of industry-relevant signals and that of ground roll. Furthermore, a dune lateral to the principle direction of a receiver spread will scatter ground roll crossline, resulting in a high apparent velocity and non-zero τ, and hence poor noise suppression. 3D surveys permit removal of ground roll with a general direction of incidence [251, 290], but adequate suppression requires large receiver arrays, increasing financial costs, decreasing spatial resolution, and attenuating high-frequency components of the signal [77].

More recent approaches include interferometric ground-roll removal [90, 144, 145] and polarisation filtering [115, 198, 283], but these are also imperfect solutions. Successful interferometric noise suppression relies on an acquisition geometry adapted to the positions of scatterers, so that scattered surface waves pass through a 'boundary' of receivers before arriving at the receiver at which noise is to be suppressed [120]. Polarisation filtering, meanwhile, imposes the additional expenses associated with three-component receivers and loses effectiveness in the case of simultaneous arrivals [167, 283]. Both will, therefore, struggle to adequately suppress noise in the case of a complex geometry of multiple scatterers, such as a desert dune field.

With generic approaches to ground-roll suppression having difficulties in the case of scattering by dunes, the modelling of the scattering process has fundamental importance. Dune-scattered ground roll will contribute differently to recorded displacements in different regions of time, space, and frequency-wavenumber space, and such modelling will allow these different contributions to be quantified. This quantification is key to the design of surveys and to the interpretation of data. However, to successfully model scattering from dunes, I must first describe their attributes.

I focus on isolated crescentic barchan dunes, as introduced in chapter 1 and studied in chapter 4. These are both sufficiently simple in form to be amenable to analysis and sufficiently common for such analysis to have application in regions of potential hydrocarbon exploration. Chapter 1 discusses the variety of dune morphologies that can exist in different regimes of sediment supply and wind variability, but in many such regions the wind is approximately unidirectional, sand supply is limited, and barchan dunes predominate. Specific examples include Kuwait's major Al-Huwaimiliyah dune field [5], the Najaf and Nasiriyah dune fields of Iraq [171], both the Eastern and Western dune fields of Qatar [21], and the Northern portion of the UAE's Al Liwa basin [35]. Barchan dunes are characterised by a crescent-shaped brinkline, with height reaching a maximum at the crescent's centre and decreasing towards the downwind-facing horns either side. On the windward side, sand is transported by the wind up a shallow slope of approximately 10°, while, on the leeward side, grains avalanche down a steep slip face at the sand's angle of repose, approximately 30°. Between dunes lies the exposed desert floor. An example is shown in Figures 5.1a and 5.1b. Dune length, width, and height are in approximately constant proportion, with heights from 1 m to over 100 m [104, 113, 205] . With barchans displaying less variation in shape than is typical of other types of dune, a smaller parameter space need be explored for applicability, while dunes' separation by the flat, exposed desert floor permits consideration of each dune in isolation.

Dunes are associated not only with topographical variation, but also with varation in seismic velocities. In the field, Criswell et al. [79] measure a surface wave speed of 120 m s^{-1} on an aeolian desert dune, while, more recently, Vriend et al. [293] measure a P wave speed of 200 ± 20 m s^{-1} in a near-surface layer and 350 ± 30 m s^{-1} in the bulk, with corresponding S wave speeds of 130 ± 20 m s^{-1} and 180 ± 20 m s^{-1}. Seismic velocities within the desert floor vary significantly depending on pressure and geological composition, but are typically much higher. In California's Eureka dune field, for example, the near-surface desert floor is composed of quartzite, with 1000 m s^{-1} a representative speed of P waves (N.M. Vriend, unpublished data, 2007), and 600 m s^{-1} a reasonable speed of S waves, based on a Poisson's ratio of 0.2 [132].

In addition to varying between the dune and the desert floor, seismic velocities vary significantly within a dune. Vriend et al. [294] observed variation of P wave speeds by a factor of around three, and explain this by variation in pressure and in water saturation. In the unconsolidated sand that forms desert dunes, seismic velocities increase with effective pressure p, and hence with depth in the dune. Variants of Hertz-Mindlin theory, assuming spherical particles

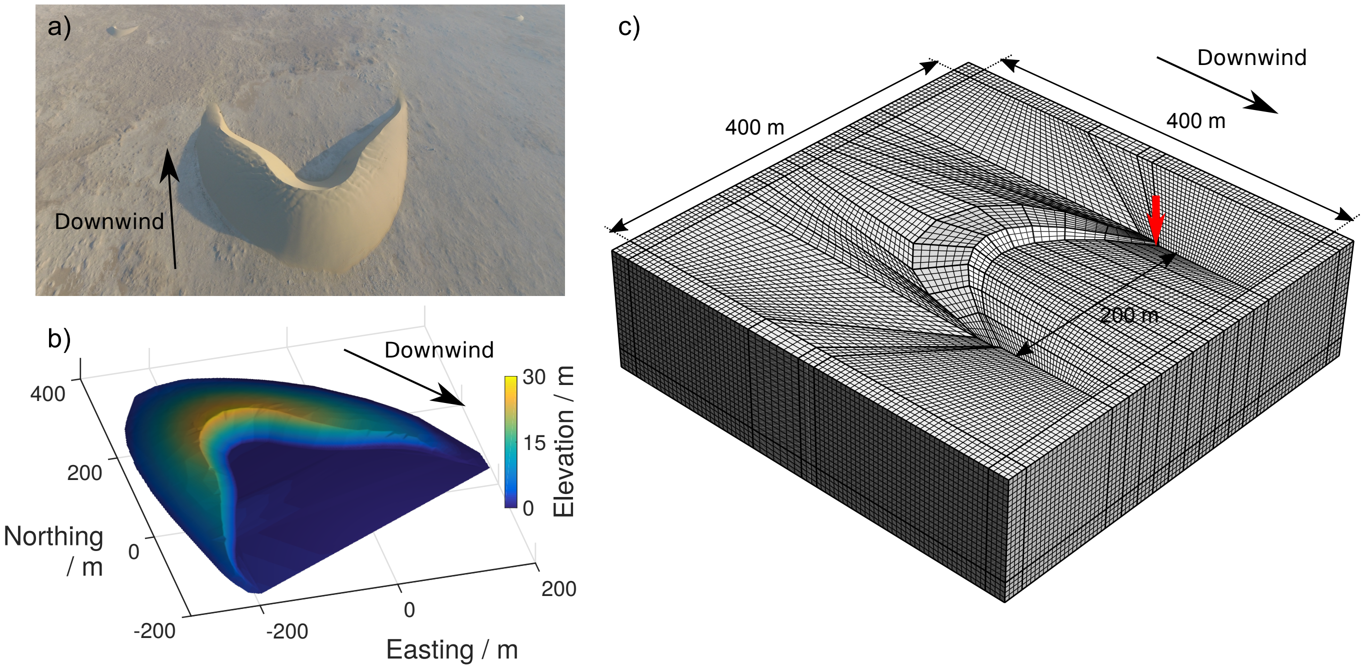

Figure 5.1: Barchan dune geometry, in reality (a, b) and my simulations (c). The features of an isolated barchan dune are indicated by an aerial photo (a) of the dune labelled B in chapter 4, courtesy of Sylvain Michel and with neighbouring dunes visible at top left and top right, while an elevation profile of dune B (b) depicts such dunes' typical topography, courtesy of data from Michel Louge. To mimic such a dune, I create a mesh with GMsh (c), as described in section 5.2.1. The red arrow indicates the location of the point force for the simulations described in section 5.2.2 and depicted both in Figure 5.2 and in the movies available online [18].

and a constant contact network, predict seismic velocities to increase as $p^{1/6}$ [96, 225, 295], while laboratory experiments instead find dependence of approximately $p^{0.25}$ or $p^{0.33}$ for S waves and $p^{0.23}$ or $p^{0.30}$ for P waves [37, 148, 314, 318]. Whilst pressure in a granular medium is not necessarily equal to the weight of the overburden, as demonstrated by Janssen pressure saturation in silos [170] and by the central pressure dip in sandpiles [272], it is standard in geophysics to assume, in a medium of constant bulk density, direct proportionality between pressure and depth.

The distribution of water saturation within a dune cannot be so easily approximated; as discussed in chapter 4, it depends on historical rainfall and structure formation within the dune. Berndtsson et al. [34] reported spatial varation of water content from 0.7% to 7.3% by volume, in a study area 3 m deep and 60 m wide on an unvegetated dune in Northwestern China, with rainfall preferentially permeating pre-existing layers. On a smaller scale, in 0.45 m by 2.5 m vertical sections on five dunes in southwestern North America, Ritsema and Dekker [257] reported variation from 2.0% to 12.6%, 2% to 8.3%, 0.6% to 11.1%, 0.6% to 11.1% and 0.6% to 5.3%, with wetter regions irregularly positioned at greater depth, representing “a residual stage from former rain events". Studies report similar orders of magnitude of variation in desert dunes in Saudi Arabia [87] and Algeria [118], and variation an order of magnitude smaller in Qatar [217]. The ground-penetrating radar studies discussed in chapter 4, section 4.1.3 show that this variation coincides with dunes’ internal structure at large scales, while the rest of the chapter demonstrates a mechanism by which this association arises at small scales. Consequently, variation in seismic velocities will be associated with the cross-strata discussed in chapter 3, emplaced by the avalanches discussed in chapter 2.

I structure this chapter in the following manner. Section 5.2 describes the development of a model for the scattering of surface waves by a solitary barchan dune, with an initial investigation, described in section 5.2.2, inspiring the development of an analytical model, in section 5.2.3. In section 5.3, I validate the model, confirming its assumptions and ascertaining the values of its parameters in section 5.3.1; and testing its predictions of the noise observed at receivers in section 5.3.2. In section 5.4, I examine the effect of varying the parameters of my system: dune geometry in section 5.4.1 and internal structure in section 5.4.2. Finally, in section 5.5, conclusions are drawn, future work discussed, and industry-relevant outputs assessed.

5.2 Model development

5.2.1 Numerical modelling

To examine the effect of a barchan dune on seismic propagation, I conduct numerical simulations using SPECFEM3D, a parallelised open-source software package which uses the continuous Galerkin spectral-element method, with Gauss-Lobatto-Legendre quadrature, to simulate the elastic wave equation [192, 243, 284]. I use spectral elements of degree 5, neglect attenuation and anisotropy, and simulate absorbing boundaries with convolutional perfectly-matched layers (CPML) [193]. Some details of these methods are provided in Appendix D, section D.1. GMsh, a three-dimensional finite-element mesh generator [133], is used to create structured hexahedral meshes for the desired geometry. A mesh refinement study is described in Appendix D, section D.2, demonstrating that a typical mesh spacing of half the dune height is sufficient for 10%

accuracy in displacement.

I construct meshes such as that shown in Figure 5.1c, with a crescentic brinkline achieving a maximum height H at its centre. All meshes are 400 m long, 400 m wide, and 100 m deep, with a typical mesh spacing of 5 m and CPML 4 grid points thick on each side, sufficient for over 99% of the energy reaching the mesh's boundaries to be absorbed (calculated as described in Appendix D, section D.3). The brinkline has coordinates $(X(\cosh(\alpha y/Y) - 1)/(\cosh(\alpha) - 1), y, H\cos(\pi y/2Y))$ in the range $|y| < Y$, for constants X, Y, H, and $\alpha = 1/2$, so that the horns are advanced a distance X downwind of the crest and have a separation of $2Y$. Tangential to the brinkline, angles of inclination on the windward and leeward faces are 10° and 30° respectively. This geometry reproduces the features of barchan dunes, while permitting the construction of structured meshes that satisfy the conditions of SPECFEM3D and are sufficiently regular for simulations to converge.

Throughout this work, I use point sources located at a depth of 1 m, to mimic the surface sources used in contemporary seismic surveys, while avoiding the numerical instability associated with simulating a source at the mesh boundary.

5.2.2 Initial simulation

To identify the processes that underlie the scattering of ground-roll by dunes, I conduct an initial simulation. I construct the mesh shown in Figure 5.1c, with geometry as defined in section 5.2.1 and parameters $H = 10$ m, $X = 100$ m, and $Y = 100$ m. I model both the dune and the desert floor as isotropic and homogeneous media. Within the desert floor, I model P and S wave velocities as 1000 and 600 m s^{-1}, respectively, whilst within the dune I model P and S wave velocities as $c_P = 350$ and $c_S = 180$ m s^{-1}, respectively. For simplicity, density is everywhere 2500 kg m^{-3}. I simulate a vertical point force of amplitude 10^3 N, 100 m downwind of the dune's crest and 100 m off its central axis, with time-dependency given by a Ricker function wavelet with central frequency 10 Hz. A movie showing vertical displacement at the surface is available online [18], with selected frames reproduced below in Figure 5.2, panel a. For comparison, I also conduct simulations of a model with identical topography, but with seismic velocities in the dune equal to those in the desert floor (panel b); and of a homogeneous halfspace of equal size (panel c).

I observe significant scattering by the sand dune over an extended period of time, with

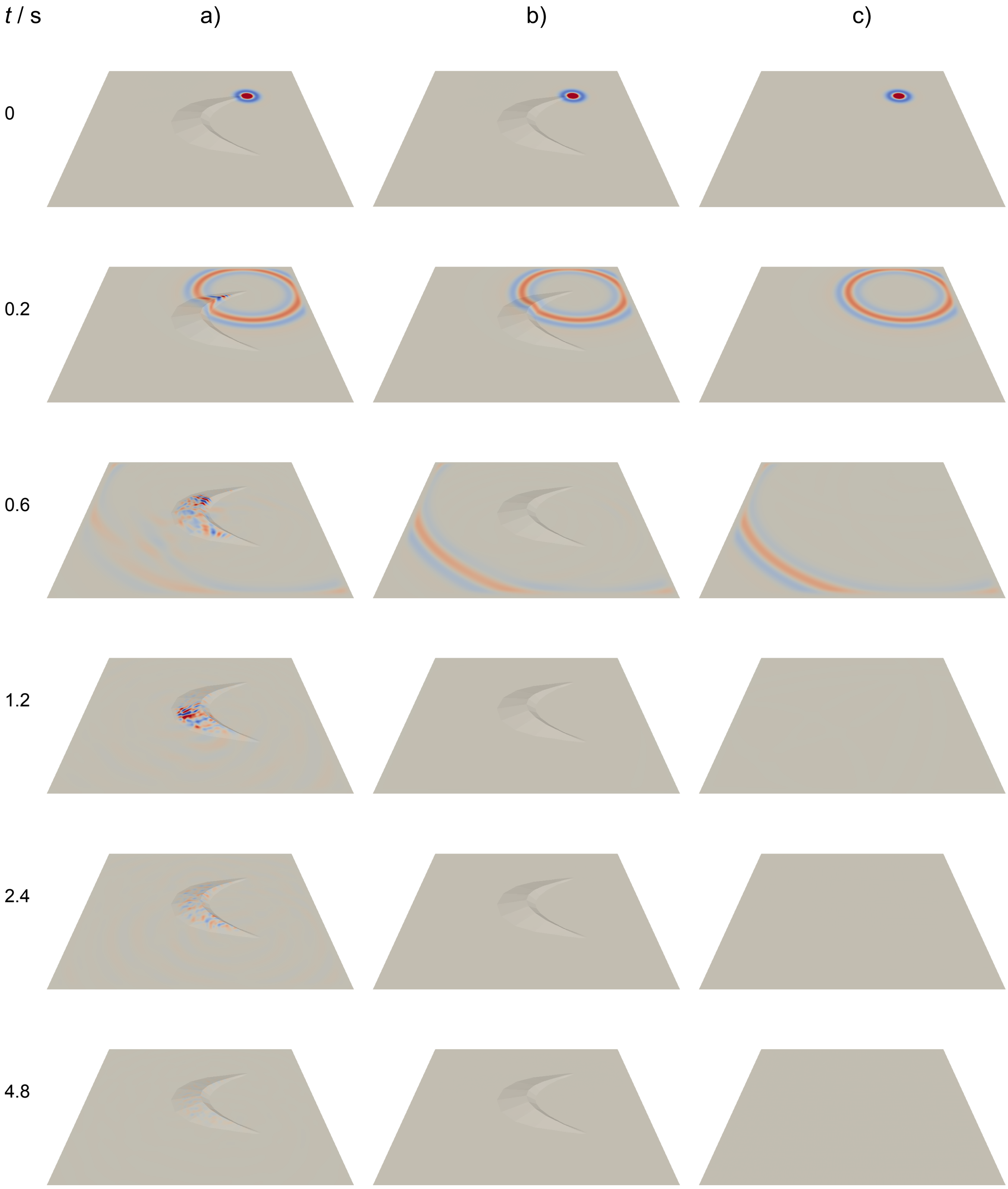

Figure 5.2: Simulated surface wave propagation in the vicinity of a dune. Colour maps of vertical displacement demonstrate surface wave propagation on the surface of a homogeneous halfspace, surmounted in turn by a dune with distinct seismic velocities (a), a dune having equal seismic velocities (b), and nothing (c). The halfspace has P and S wave velocities 1000 and 600 m s^{-1} respectively, whilst in panel a the dune has P and S wave velocities of 350 and 180 m s^{-1} respectively.

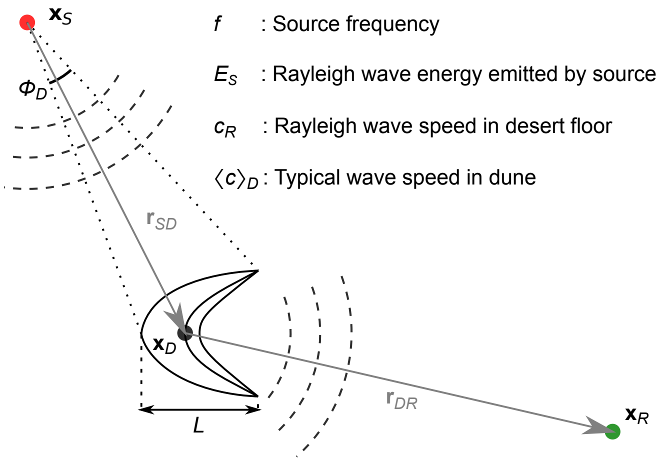

Figure 5.3: A schematic of wave scattering by a dune. I define variables $\boldsymbol{x}_S$, $\boldsymbol{x}_D$, $\boldsymbol{x}_R$, $\boldsymbol{r}_{SD}$, $\boldsymbol{r}_{DR}$, L, Φ_D, c_R, $\langle c \rangle_D$, f, and E_S.

the majority of this scattering related to the difference in seismic velocities between the sand dune and the desert floor. Considering individual wave packets over time, I see that those reaching the dune are either reflected from or transmitted through its boundary. Transmitted energy propagates within the dune, with a certain proportion emitted each time the boundary is reached. The complex geometry of the dune causes that proportion of the wave packet that is retained within the dune to lose coherence over time, resulting in a distribution of energy only weakly corresponding to initial conditions, decaying primarily through emission of surface waves.

5.2.3 Analytical model

Given the observations described above, I propose a highly simplified model for seismic propagation in the vicinity of a dune, illustrated schematically in Figure 5.3. I suppose that a source at position $\boldsymbol{x}_S$ emits surface waves of frequency f in some short time window about t_S, with total energy E_S emitted as Rayleigh waves.

Assuming isotropic radiation and no attenuation over a homogeneous desert floor with Rayleigh wave speed c_R, the energy reaching a dune subtending angle Φ_D, of lateral extent L and with crest position $\boldsymbol{x}_D = \boldsymbol{x}_S + \boldsymbol{r}_{SD}$, will be

$$\frac{E_S \Phi_D}{2\pi} \approx \frac{E_S L}{2\pi ||\boldsymbol{r}_{SD}||}. \tag{5.1}$$

The arrival time will be approximately $t_S + ||\boldsymbol{r}_{SD}||/c_R$, with approximations exact in the far-field limit $||\boldsymbol{r}_{SD}||/L \to \infty$. The transmittance T, defined as the proportion of energy transmitted to the dune, will be a nontrivial function of the dune's geometry and of the ratios of densities and seismic velocities between the dune and the desert floor. This will be governed by the Zoeppritz equations [3, 319], which describe the reflectance and transmittance of seismic waves incident upon a planar interface. For a given dune, T will be determined by the direction of arrival $\hat{\boldsymbol{r}}_{SD}$, governing the geometry encountered by the incident surface-wave, and f, governing the distribution with depth of the incident surface wave energy.

I assume that, once transmitted to the dune, the wave packet loses coherence, so that the seismic energy adopts a distribution among the available degrees of freedom that is independent of initial conditions. In this state, a constant proportion of energy will be lost over time to transmission through the dune's boundary, resulting in an exponential decay of energy density within the dune. Without attenuation, the decay timescale τ will be a nontrivial function of density and velocity ratios, but also of the distribution of energy within the dune and hence of f. The dune will support a spectrum of normal modes, at which resonance will be achieved and τ will be significantly larger. As τ has units of time, I expect it to scale with the timescale of energy propagation between internal reflections $L/\langle c\rangle_D$, for $\langle c\rangle_D$ a typical seismic velocity within the dune. Given this decay timescale, the total energy within the dune, at time t, will be

$$E_D(t) \approx \frac{E_S L T(\hat{\boldsymbol{r}}_{SD}, f)}{2\pi ||\boldsymbol{r}_{SD}||} \exp\left[\frac{-1}{\tau(f)}\left(t - t_S - \frac{||\boldsymbol{r}_{SD}||}{c_R}\right)\right]. \tag{5.2}$$

Being conserved, any energy lost in the dune will be emitted, propagating to the far field with a geometry, density, velocity, and frequency-dependent radiation pattern. I expect, again, the preponderance of energy to be transmitted by surface waves and so write $D(\boldsymbol{n})\mathrm{d}\theta/2\pi$ for the proportion of energy propagated to the far field within angle element $\mathrm{d}\theta$ about horizontal direction $\boldsymbol{n}$, referring henceforth to the function D as a directivity, analogous to the directive gain of an electromagnetic antennae. As a result, at a distant receiver location $\boldsymbol{x}_R = \boldsymbol{x}_D + \boldsymbol{r}_{DR}$ and at time $t > t_S + ||\boldsymbol{r}_{SD}||/c_R + ||\boldsymbol{r}_{DR}||/c_R$, the energy flux of arriving scattered surface waves, per unit distance in the azimuthal direction, will be given by

$$\mathscr{F} \approx \frac{E_S L T(\hat{\boldsymbol{r}}_{SD}, f) D(\hat{\boldsymbol{r}}_{DR}, f)}{4\pi^2 ||\boldsymbol{r}_{SD}|| ||\boldsymbol{r}_{DR}|| \tau(f)} \exp\left[\frac{-1}{\tau(f)}\left(t - t_S - \frac{||\boldsymbol{r}_{SD}||}{c_R} - \frac{||\boldsymbol{r}_{DR}||}{c_R}\right)\right]. \tag{5.3}$$

The resulting amplitude of vertical displacement was given by Rose in 1984 [258]. Dependence on dune geometry and the ratios of densities and seismic velocities is neglected in the above argument, but will enter into T, D and τ.

5.3 Model validation

5.3.1 Validation of assumptions

To examine the above assumptions and to quantify T, D, and τ, I analyse synthetic seismograms generated in further numerical simulations. Using the barchan dune model depicted in Figure 5.1c, I conduct simulations of four delta-function point forces, with positions illustrated in Figure 5.4a. I consider the system's response to sources localised about time $t = 0$ and about frequencies f_0, by convolving synthetic seismograms with Gabor wavelets, waveforms

$$F(t) = \exp(-f_0^2 t^2/4)\exp(2\pi i f_0 t). \tag{5.4}$$

These wavelets provide optimum time-frequency localisation, in the sense of minimising the product of time-domain and frequency-domain standard deviations. I approximate E_S in frequency space for each f_0, assuming surface forcing and using the work of Miller [232], and take L to be the distance between the horns, equal to 200 m. I first analyse displacements at locations below the dune's brinkline, to consider the increase and decay of energy density within the dune.

In accordance with my model, the transmission of energy to the dune is associated with the arrival of Rayleigh waves, and the subsequent decay of energy within the dune E_D is exponential (Figure 5.4b). I infer this from the exponential decay of the more-easily-measured energy density, $U = E_D/V$ for dune volume V, and conduct a least-squares best linear fit of $\ln(U)$ against t at each receiver within this dune. Using this regression and calculating constants E_S from the source waveform, L, $\boldsymbol{r}_{SD}$ and V from the simulated geometry, and c_R from the cubic equation for Rayleigh wave speed, I extract transmission and decay constants T and τ.

Extracted transmittance T and decay time τ scale appropriately with dune size and with seismic velocities within the dune (Figure 5.4c). In particular, T increases with source frequency, as Rayleigh wave energy is increasingly concentrated close to the surface, before decreasing sharply as self-interference at arrival becomes significant. Superimposed on these general trends are smaller variations, which I associate with the varying proportion of wave energy emitted as the wavepacket loses coherence within the dune. Dependence of T on the direction

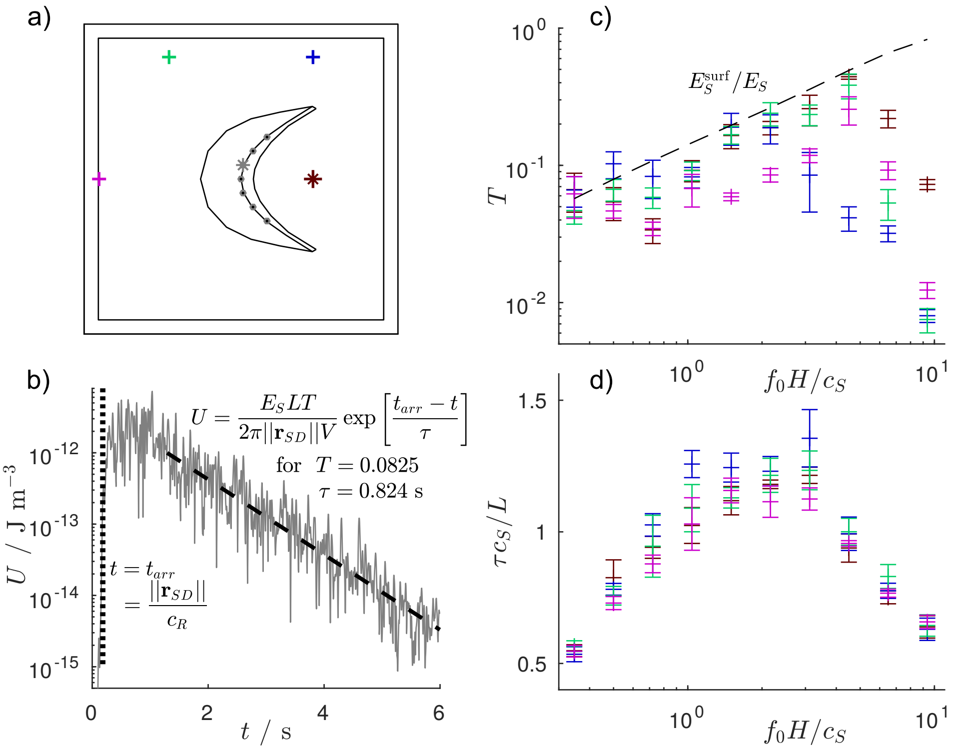

Figure 5.4: The evolution of energy density U within the dune and its associated decay constants, T and τ. A schematic of the mesh (a) indicates the locations of simulated sources (+) and receivers (•, level with the desert floor). A plot of energy density (b) exemplifies its sharp increase within the dune at a time associated with Rayleigh wave arrival, its adjustment over a timescale of approximately 1 s, and its exponential decay, for the source and receiver marked $*$ and with the source waveform a Gabor wavelet of centre frequency $f_0 = 168$ Hz. Decay constants T and τ are extracted by a least-squares best linear fit of $\ln(U)$ against t, and calculated given constants E_S, L, $||\boldsymbol{r}_{SD}||$, c_R, and dune volume V. Transmittance T (c) varies by up to an order of magnitude with source position and decreases rapidly at higher f_0. Decay time τ (d) is independent of source position, is of the same order as L/c_S, and is peaked at a frequency corresponding to shear wave resonance across half the height H of the dune. Colours correspond to sources in panel a, while error bars correspond to standard error over the seven simulated receivers. I non-dimensionalise with dune height H, lateral size L, and shear velocity c_S, and the dashed line indicates the proportion E_S^{surf}/E_S of Rayleigh wave energy above a depth of 1 m, acting as an upper bound for T.

of arrival is complex, corresponding to the non-trivial geometry encountered, with the range of variation approximately one order of magnitude. τ, meanwhile, is independent of the direction of arrival, indicating that the late-time distribution of energy within the dune is indeed independent of initial conditions. τ is of the same order as the timescale for shear wave propagation between internal reflections, and has a distinct peak corresponding to resonance, as suggested by [209] and as discussed in the case of subsurface heterogeneities by Korneev in 2009 [197]. I hypothesise that this 'resonant frequency' is associated with a wavelength of shear waves within the dune equal to the typical vertical thickness of the dune, $H/2$. Having established the values of parameters T and τ, equation 5.2 specifies the energy inside the dune over time and hence the rate at which it emits energy.

To investigate the transmission of energy emitted by the dune, I analyse synthetic seismograms in the far field, generated in the same simulations but corresponding now to surface locations a) at increasing radial distance from the dune centre, in the same direction, and b) at a constant radial distance of 180 m from the dune's centre and arranged around it. I again use the Gabor wavelets specified by equation 5.4. As expected, Rayleigh waves are predominantly responsible for transmitting energy to the far field, as demonstrated by the characteristic propagation velocity and elliptical displacement trajectories shown in Figure 5.5a. I calculate the relative Rayleigh wave energy flux at simulated receivers to extract directivities D, which are plotted in Figure 5.5b.

5.3.2 Verification of predictions

Having established the fundamental assumptions of my mathematical model, and extracted its parameters, I compare its predictions of ground-roll noise level with observations from simulations. I conduct a simulation with realistic receiver line in the vicinity of a dune, as depicted schematically in Figure 5.6a, and produce a synthetic seismogram (Figure 5.6b) in which the expected features can be observed: a direct Rayleigh wave, initial reflections from the dune, and subsequent arrivals of waves emitted from the dune following absorption and reverberation.

In Figure 5.6c, I compare the observed receiver displacements due to the latter to the amplitudes predicted by my model and note that my predictions represent a remarkably tight bound, over the entire receiver line and over a time in which the energy flux of passing waves decreases by a factor of 400. The only exception to this corresponds to waves emitted from the dune at early times (after a residence time within the dune of ≈ 0.4 s), when energy within the dune has not yet adopted a distribution independent of initial conditions. Over a duration of ≈ 0.4 s at each receiver, a coherent wavepacket passes receivers upwind of the dune, after having travelled through the dune, been reflected from its leeward face, and travelled back. Even at these times, the bounds established by my model are exceeded by a factor of only three.

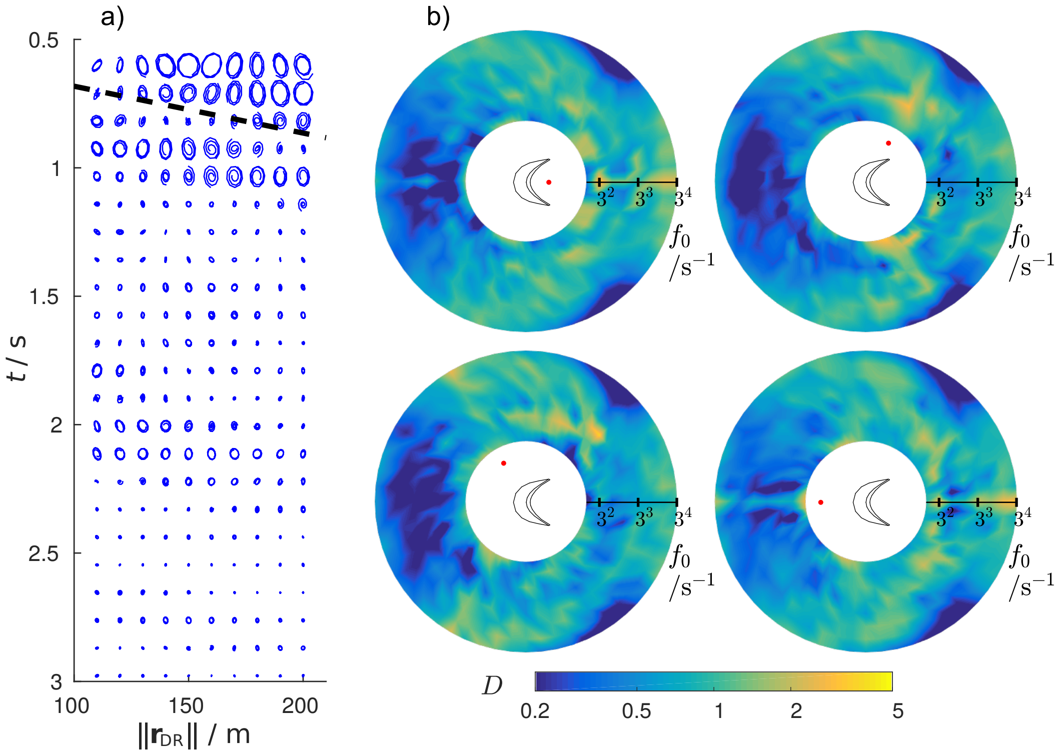

Figure 5.5: The emission of energy to the far field and its associated directivity D. On an illustrative hodogram of the real component of displacement (a), particles trace the elliptical trajectories characteristic of Rayleigh waves and disturbances propagate radially outwards at the Rayleigh wave velocity. The direction from the dune's centre to receivers is at 90° to the wind, and subplots are particle paths in the radial-vertical plane, over 0.11 s time windows, for a source 100 m downwind of the dune's centre and with a Gabor wavelet waveform of centre frequency 27 Hz. The dashed line indicates the Rayleigh wave propagation speed. From plots of directivity D (b), for varying source positions (●) relative to the dune, I observe that D is only weakly dependent on the source's position, as assumed by my model, and that D varies by over an order of magnitude, with little energy emitted upwind of the dune at a wide range of frequencies, or in the direction of the horns at high frequencies. For each source position, I consider 60 receivers, each 180 m from the dune's centre and with an azimuthal separation of 6° from its neighbours. I measure at each receiver, position $180\boldsymbol{n}$ relative to the dune's centre, the square amplitude $A(\boldsymbol{n}, t; f_0)$ of vertical displacement, in response to a source with a Gabor wavelet waveform of centre frequency f_0. I define $D(\boldsymbol{n}, f_0)$ as the median over late times, after the direct wave and initial reflections have passed, of $A(\boldsymbol{n}, t; f_0)/\langle A(\boldsymbol{n}, t; f_0)\rangle_{\boldsymbol{n}}$ and I represent D by colour in radial plots, with azimuth corresponding to that of $\boldsymbol{n}$ and radial distance to f_0.

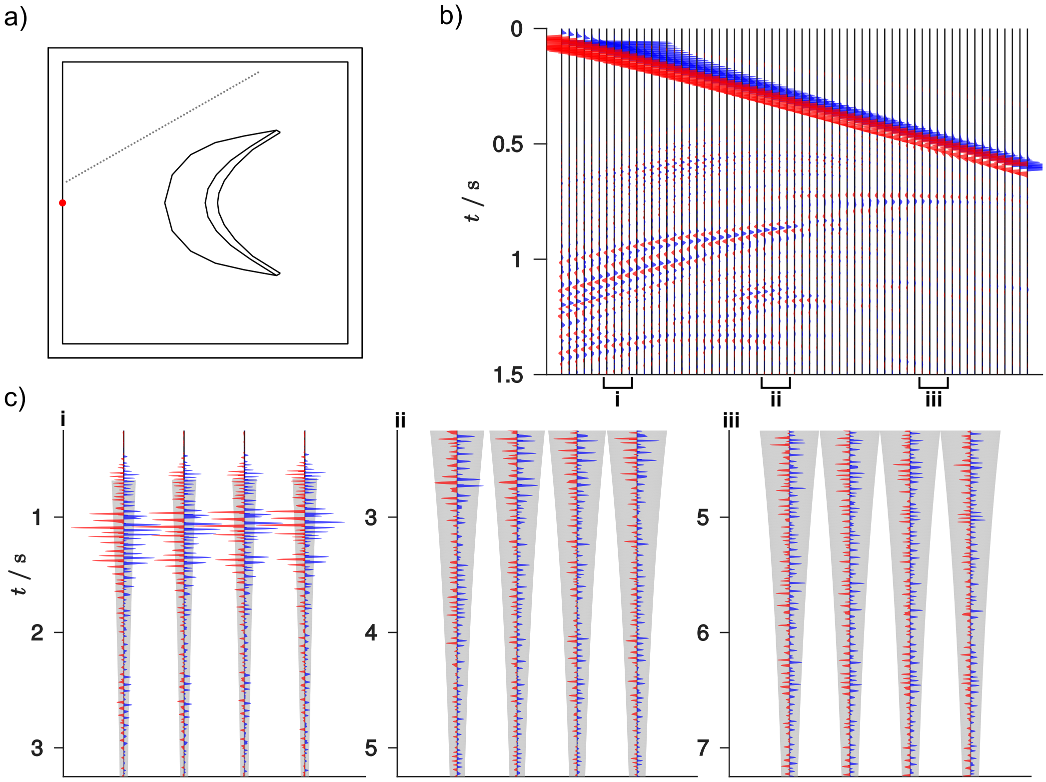

Figure 5.6: Verification of predictions. A schematic of the mesh (a) indicates the locations of a simulated source (•) and receivers (·). The source waveform is a Ricker wavelet of centre frequency $f_0 = 20$ Hz and the ground-level receivers have 5 m spacing between them. A synthetic seismogram (b) shows vertical displacement at the receiver locations, over time. The direct Rayleigh wave is at the top of the record, while the first arrivals of waves reflected from and emitted by the dune are at 0.5 s and 0.7 s, respectively. 12 receivers, in the three regions indicated by i, ii, and iii, are selected for model verification (c). Comparing observed displacements (trace) to amplitudes predicted by equation 5.3 (gray envelope), the model provides an excellent bound for displacement due to energy emitted from the dune, over a range of receivers and a factor 20 decrease in displacement magnitude over time. The exception is the wave in subpanel i arriving at $t = 1.1$ s, after a single internal reflection in the dune (for which the order of magnitude is correctly predicted). Parameter values are estimated by linear interpolation in $\log f_0$, $\arg \boldsymbol{r_{SD}}$, and $\arg \boldsymbol{r_{DR}}$, as appropriate.

5.4 Exploration of parameter space

5.4.1 Dune geometry

Whilst I have established my model's accuracy for the mesh hitherto discussed, its applicability to physical scenarios depends on the stability of its parameters to changes in dune geometry. I therefore examine the sensitivity of the parameters T, τ, and D to changes in dune length, width, and height. Specifically, I construct new meshes, each including a dune with the same

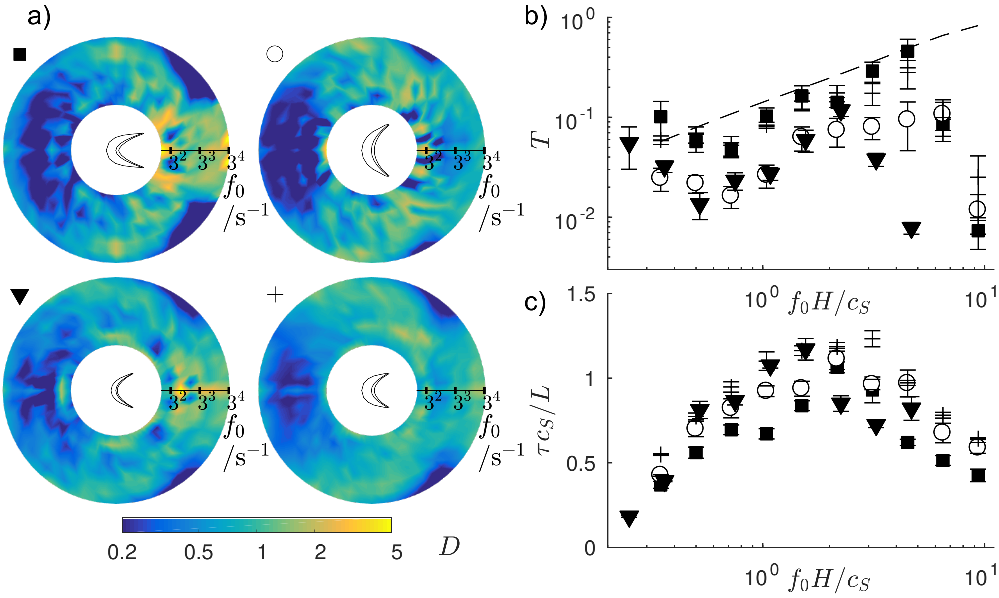

Figure 5.7: Variation of directivity D (a), transmittance T (b), and decay time τ (c), with dune geometry. I simulate ground-roll scattering by long (■, $X = 160$), wide (○, $Y = 150$), and short (▼, $H = 5$) dunes and compare to the dune described in previous sections (+, $X = Y = 100$, $H = 10$). D is calculated as described in Figure 5.5b and a schematic of the corresponding dune geometry is in the centre of each subplot. T and τ are calculated as described in Figure 5.4c.

hyperbolic crest line and angled faces discussed in Section 5.2.2, but with, in turn and with all else held constant in each case: length X increased by a factor of 1.6; width Y increased by a factor of 1.5; and height H reduced by a factor of 2. While these parameter values are unrealistic, they may be thought of as exaggerations of reasonable, realistic variations within the parameter space. I use the same methods to determine parameter values as described in Section 5.3.1, with the source 100 m downwind of the dune crest, except that I now define $L = 2\sqrt(XY)$, consistent with the above but taking into account the length of the dune's horns.

Figure 5.7 demonstrates that the model parameters display similar behaviour over a wide range of dune geometries. T, τ, and D vary under changes of X, Y, and H, but the magnitude of such variation is typically less than that achieved by a proportionate change in arg $\boldsymbol{r_{SD}}$, f_0, or arg $\boldsymbol{r_{DR}}$. In addition, not only are the parameters of the same order as predicted in Section 5.2.3 and measured in Section 5.3.1, but the frequency corresponding to resonance in the dune is approximately $2c_s/H$ for all dune geometries considered, as previously hypothesised.

5.4.2 Internal structure

Thus far, I have considered a highly simplified model of seismic velocities, assuming homogeneity in the desert floor and homogeneity within the dune. For the sake of continued simplicity and, in particular, so that Rayleigh waves remain non-dispersive, I maintain the assumption of homogeneity within the desert floor, with density 2500 kg m^{-3} and seismic velocities $c_P^f = 1000$ m s^{-1} and $c_S^f = 600$ m s^{-1}. However, to investigate whether dunes' internal structure has a significant effect on their absorption and reemission of ground roll, I now consider a more realistic model for the dune and allow seismic velocities to vary throughout its volume.

I use models for density and seismic velocities within the dune derived from existing literature, with the intention of calculating physically reasonable distributions of these quantities. On the basis of Logie [213] and Ritsema and Dekker [257], I take the bulk density throughout the dune to be 1600 kg m^{-3}. I assume pressure p to be lithostatic and use the empirical models proposed by [37] for seismic velocities in dry sand, with $c_P^{\mathrm{dry}} = 21p^{0.30}$ and $c_S^{\mathrm{dry}} = 8.2p^{0.33}$, for quantities measured in SI units. To include the effect of water saturation, as found to be significant by Vriend et al. [293], I use the results of Barrière et al. [30] and assume that seismic velocities decrease by 0.2% of their dry values for each 1% increase in water saturation, hence 0.5% of their dry values for each 1% increase in water content by volume. I suppose that within the dune, with upwind distance from the dune's slip face, 12 m thick layers in which water content by volume is 1.2% alternate with 4 m thick layers in which water content by volume is 6%. This corresponds to 9-month 'dry' seasons being followed by 3-month 'wet' seasons, for a dune migrating at a constant velocity of 16 m yr^{-1}; these conditions may be considered a physically reasonable idealisation of those observed by Louge et al. [217] and Berndtsson et al. [34]. Under these assumptions, seismic velocities within the dune will have the distributions represented in Figure 5.8a. I write $\langle c_S \rangle$ for the mean shear wave velocity within the dune.

Given this velocity structure, and the mesh geometry discussed in Section 5.2.2, I simulate a point force 100 m downwind of the dune's crest and extract parameters T, τ, and D as described in Section 5.3.1. The resulting parameter values are shown in Figures 5.8b and 5.8c.

Model parameters have similar behaviour to that noted in the case of a homogeneous dune, but differ significantly in their exact values. In Figure 5.8b, T is measured to be approximately an order of magnitude lower than in the case of a homogeneous dune, with the majority of the energy absorbed by the dune reemitted before the adoption of a time-independent distribution.

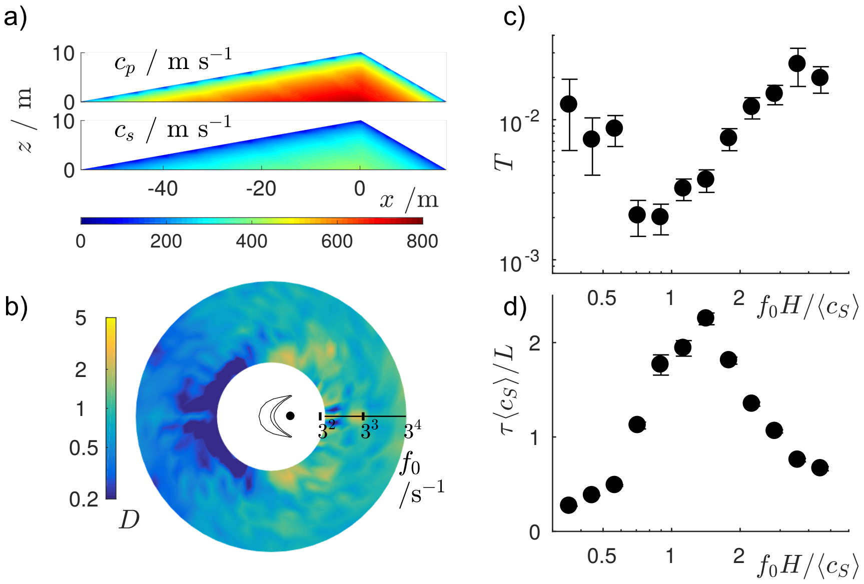

Figure 5.8: Directivity D (b), transmittance T (c), and decay time τ (d), in the case of internal velocity variation. Sections of c_P and c_S through the dune's $y = 0$ centreline (a) demonstrate variation in seismic velocities. D is calculated as described in Figure 5.5b, with the source position indicated in the centre of the subplot. T and τ are calculated as described in Figure 5.4c. I non-dimensionalise as previously, but now with $\langle c_S\rangle = 280$ m s^{-1}, the mean shear wave velocity within the dune.

However, T demonstrates the same increase with f_0 as previously noted, and the same decrease at high f_0. Similarly, τ demonstrates the same resonance-associated peak at $f_0 \approx 2\langle c_S\rangle/H$, but I note that the peak is significantly narrower and, when suitably non-dimensionalised, higher, indicating a stronger resonance. Considering D, Figure 5.8c demonstrates preferential energy emission in the direction of the dune's migration, as observed for a homogeneous dune. However, even at the highest centre frequencies investigated, I observe no deficit in the energy emitted in the direction of the dune's horns, and this is markedly contrary to results in the homogeneous case.

5.5 Discussion

I have demonstrated that, under reasonable physical assumptions, an isolated barchan sand dune will be a significant source of off-line scattered ground roll over a prolonged interval of time, as a result of the absorption and subsequent reemission of seismic energy. As depicted in the movie online [18], a significant proportion of the energy radiated by a seismic source will propagate in the form of Rayleigh waves, or ground roll, and some proportion of the energy reaching a dune will be transmitted through its boundary and absorbed by its interior. Internal reflection will lead to reverberation of this energy within the dune, with some proportion transmitted through the dune's boundary in each interval of time. It is this reemitted energy, propagating to the receiver spread in the form of Rayleigh waves, that will manifest itself as noise in seismometer traces.

I have developed and verified a simple analytical model for the process of energy absorption and reemission, providing a tight bound on the amplitude of noise due to reemitted ground roll. My assumptions, that Rayleigh waves are the dominant mechanism for energy transfer and that the energy absorbed by the dune quickly adopts a distribution independent of initial conditions, imply that energy density within the dune will display a characteristic sudden increase and exponential decay, which I observed in my simulations. Using one set of simulations to extract parameters of my analytical model, I verified that they take physically reasonable values, and successfully predicted the amplitude of noise at a realistic receiver spread in an independent simulation.

Under variations of dune geometry and internal structure, I have shown that the model's parameters have similar behaviour, estimable from easily-measurable properties of the dune such as height H, typical width L and typical shear wave velocity c_S. The proportion T of arriving energy transmitted to the dune increases with the typical frequency of the source's oscillations f_0, associated with the increasing proportion of the Rayleigh wave energy concentrated near the surface, before decreasing as self-interference becomes significant at $f_0 \sim c_S$. The decay time τ has a peak at $f_0 \approx 2c_S/H$, attaining a value $\tau \approx L/c_S$, associated with a half-height shear wave resonance within the dune, and decreases for greater and lesser f_0. Of the energy emitted from the dune, a lower proportion D is directed upwind of the dune, away from its horns, than is emitted in the direction of the dune's horns.

My results allow quantitative predictions of the seismic noise arriving at surficial receivers in the vicinity of an isolated barchan, which can be validated in field experiments. Field data can be examined for evidence of scattered ground roll arrivals associated with isolated barchan dunes, and for exponential decay of the amplitude of the noise associated with these arrivals.

For the sake of simplicity, some physical properties that are significant in the field have been neglected. In particular, I neglected attenuation, assumed constant seismic velocities in the desert floor, and assumed a single dune rather than considering multiple dunes. Neglecting attenuation will have a significant effect on the amplitude of dune-scattered ground roll, since uncohesive sand is strongly attenuative. However, isotropic, anelastic attenuation may easily be added to my work by adding a multiplicative term to the analytic model of equation (5.3), of the form $\exp\left[-f(t_{SD}+t_{DR})\ln(1-\alpha^f)\right]\exp\left[-f(t-t_{SD}-t_{DR})\ln(1-\alpha)\right]$ for intrinsic attenuation factors α^f and α, equal to the proportions of seismic energy absorbed in the desert floor and in the dune, respectively, per period of oscillation. Assuming constant seismic velocities in the desert floor will significantly change the arrival time of dune-scattered ground roll, since Rayleigh waves are dispersive in a heterogeneous medium, and the near surface is typified by significant increases in seismic velocity with depth. However, the effect of this change may also be included, by replacing the constant Rayleigh wave velocities in my analytic model with the frequency-dependent Rayleigh wave velocities of the region with which one is concerned. Finally, the effect of multiple dunes may be considered by considering the energy flux arriving at a receiver and conducting a perturbation expansion, in the geometric attenuation factor between dunes, analogous to that used for multiple scatterers. To first order in this factor, the contributions of each dune may be considered in isolation, and summed to calculate the total contribution of the dune field. To second order, each dune radiating ground roll must be considered as a source in relation to each other dune, and the related contributions again summed. Continuing this process would yield a noise estimate that takes into account an arbitarily large number of inter-dune interactions, making the effect of a dune field calculable.

Of perhaps more concern, a number of the properties I have used are poorly quantified in the field. The estimates used for seismic velocities within sand dunes are drawn from a limited number of studies, none of which have probed the entire depth of a barchan dune. Extrapolating the results of laboratory studies to the field, as I did in the case of seismic velocities' dependence on pressure and on water saturation in Section 5.4.2, is prone to error, and the results are often in conflict with data from the field. For example, Barrière et al. [30] suggested that seismic velocities should decrease with increasing water content, contrary to the observations of Vriend et al. [293]. The work done in chapters 2 to 4 requires extension, to be able to predict the internal structure of dunes and the associated variation in water content, in order to link this variation with that in seismic velocities.

However, given better quantification of system parameters, or the validation in the field of predictions made with existing estimates of such parameters, my work implies the possibility of tailoring survey design to minimise the deleterious effects of dune-scattered ground roll. The work I have presented suggests that, to minimise noise, receivers are best placed upwind of isolated barchan dunes, and that, in the vicinity of a dune of height H and typical shear wave velocity c_S, frequencies $f_0 \approx 2c_S/H$ are best avoided in analysis. Equation 5.3 also allows the establishment of a criterion for the necessary distance from a given dune to detect a signal of specified arrival time and amplitude, in a specified frequency range of analysis.

5.6 Recommendations

I recommend the following extensions to this work:

- Test the validity of this numerical study's results, by analysing real field data.
- Include realistic seismic attenuation in simulations.
- Explore the parameter space more widely, varying the ratios between seismic velocities in the desert floor and in the dune.
- Expore the effects of different internal structure within the dune.
- Explore the effects of dunes with different morphology: linear, star, &c.

Chapter 6

Conclusions

In the four preceding chapters of this dissertation, I have described my work on four, linked projects. My conclusions from each project are recorded in each chapter, in sections 2.3, 3.4, 4.4, and 5.5. Here, therefore, I limit myself to summarising these conclusions and discussing the implications of this work for the interdisciplinary study both of avalanching on dunes and of its effects.

In chapter 2, I described hitherto unrecorded behaviour of discrete avalanches on the surface of a channelised, unbounded, slowly-supplied grainpile, introducing simple models for this behaviour and verifying that these simple models capture important properties of the system. Without tuning of any external parameters and without selection of a particular grain type, the system spontaneously alternates between two regimes: one in which avalanches propagate quasi-periodically to the end of the channel and another in which the intervals between avalanches are irregular and most stop partway down. The second regime exists as a result of downslope variability in the pile's surface heights since, when high, such variability is capable of stopping avalanches, overcoming the hysteresis between static grains and flowing grains that explains the previously-documented first regime. Meanwhile, evolution of the pile's surface's mean slope angle controls the transitions to and from the irregular regime. While the system is in this regime, flowing grains can interact with the stopped fronts of previous avalanches, leading to complex behaviour and implying that, at points with distances X downslope, the mean waiting times between one avalanche and the next are proportional to X.

Chapter 3 described the implications of this relationship for the formation of layers within dunes and details an experiment confirming the equivalent result for layer formation within a channelised grainpile. Bounding the pile of chapter 2 at its bottom, I showed that such a system is confined to remain in the irregular regime. In this regime, stopped avalanche fronts can be equated with the 'trapped kinks' described by previous authors, with each avalanche emplacing, upon stopping, an inversely-graded cross-stratum as a result of within-avalanche size-segregation. Measuring the mean widths $\bar{Y}$ of these cross-strata at downslope distances X, I verified that $\bar{Y} \propto X$ near the pile's bottom, as longer waiting times between avalanches correspond to a larger net inflow of grains. Provided that avalanche initiation is independent of slip face length and that three-dimensional effects do not alter the underlying mechanisms, the mean width of cross-strata in an aeolian sandstone will be proportional to the height of the dune on which it was emplaced, suggesting the possibility of interpreting paleoclimate from such cross-stratum widths.

Informed by the background of chapter 3, the work described in chapter 4 sought to measure grain size distributions across individual cross-strata in active barchan dunes, measuring their widths and associating them to the permeation of water. Whilst I was able to consider cross-stratum widths only qualitatively, quantitative analysis of samples extracted from dunes at stratum-scale resolution supports previously-attested grain-size relations: improved sorting down the lengths of cross-strata and inverse grading across their widths. Photographs demonstrate clear permeation of water along cross-strata and particularly along the regions of such cross-strata with a high concentration of small particles. This is a consequence of higher capillary potential in those regions, so that such water will have a long residence time within the dune, increasing the viability of dune stabilisation through bacterial biocementation.

Finally, chapter 5 describes numerical and analytical modelling of an isolated barchan dune's effect on the propagation of surface waves. Such a dune absorbs surface waves, which propagate within their interior and are reemitted over time. For a dune of height H and width L, with typical internal shear wave velocity c_S, the amplitude of reemitted waves decays exponentially over time, with a frequency-dependent decay time τ that scales as L/c_S and is largest close to a 'resonant' frequency of the dune $f_0 = 2c_S/H$. The pattern of emission is directional, with less energy emitted upwind of the dune, and the amplitude of disturbances at surficial receivers can be accurately predicted by accounting for this directivity pattern, the decay time of energy within the dune, and the proportion of energy transmitted to the dune. Predictions are robust to variation of the dune's geometry, but are significantly affected by its internal seismic velocity structure, which is poorly constrained. The variations in water content discussed in chapter 4 appear to concentrate acoustic energy within the dune, resulting in a narrower but higher peak of τ around f_0. When designing exploratory seismic surveys for oil and gas, it is possible to predict regions of time, space, and frequency-space in which noise from dune-scattered surface waves will be problematic, either by using the analytical model proposed or by conducting new simulations. Furthermore, it is advisable both to place receivers upwind of dunes and to avoid analysis at frequencies close to f_0.

These recommendations for exploration geophysics, along with the success of the simple models described in chapter 2, demonstrate the utility of an applied mathematical approach in diverse fields. Significant progress can be made by considering only simple, essential features of a given scenario, even on real-world problems that are difficult due to complexity and non-linearity (as in chapter 2) or due to complicated geometry (as in chapter 5).

However, this dissertation also demonstrates another reason for working across different disciplines: effects studied in one discipline can be usefully linked to a problem in an entirely different discipline. The size-segregation within avalanches that I describe in chapter 3 results in the differential water permeation that I observe in chapter 4 and understanding the former allows explanation of the latter, as well as predictions of the viability of bacterial dune stabilisation. The process of stratification on dunes is complicated by the details of granular avalanches, with interactions between fluid-like avalanches and solid-like stopped avalanche fronts leading to a non-trivial probability distribution of avalanche sizes, but this complication is helpful. A better understanding of avalanches indicates a relation between dune height and cross-stratum width, while literature on sedimentary strata can provide insight into size-segregation in granular flows[a].

In other cases, the complication of one discipline's problem by another's effect is unhelpful. Due to the non-trivial relation between grain-size distributions and water permeation, the presence of the cross-strata introduced in chapter 3 prevents analytical calculation of water's distribution within dunes, in chapter 4. In addition, to select the appropriate resolution with which to extract samples from dunes, I needed insight on grain mobilisation by avalanches, from the work conducted in chapter 2. The clearest example of unhelpful complication is in chapter 5, in which I demonstrate that heterogeneous water content within dunes complicates

---

[a] That this link between fields was not utilised for 30 years is a sociological problem, rather than a physical one.

their effect on seismic surveys. Since distributions of water content are hard to measure and the effects of such water content on seismic velocities are poorly understood, this complication constrains the accuracy with which surface-wave scattering by a dune can be predicted.

In summary, there are three key reasons to work across disciplines. Firstly, progress can be made in many disciplines with a simplifying ‘outsider’ perspective. Secondly, links between disciplines can allow progress in one discipline to be transferred to another. Finally, a problem in one discipline can be complicated by effects studied in another, in a way that necessitates study of both disciplines for progress in one to be made. All three have been demonstrated within this dissertation.

Appendix A

Supplementary Material for Chapter 2: Intermittency between avalanche regimes on grain piles

A.1 Data processing for interval extraction

A.1.1 Experiments with continuous inflow and a fixed laser profile scanner

I distinguish avalanches by the value of the mean squared rate of change of height in the field of view of the laser profile scanner. The scanner, fixed at a distance X downslope, measures surface heights $h_{j,k}$ at $n = 512$ positions x_j in the channel's centreline, at times t_k separated by an interval $\delta t = 0.05$ s, and so this value may be expressed as

$$\langle \dot{h}^2 \rangle = \frac{1}{n} \sum_j \frac{(h_{j,k+1} - h_{j,k})^2}{\delta t^2}. \tag{A.1}$$

When no avalanching grains are in the field of view of the scanner, I expect that $h_{j,k}$ will be subject to independent, random measurement errors, approximately normally distributed, with standard deviation the measurement error of the scanner, $\epsilon = 0.09$ mm. Therefore, I expect that $n\delta t^2 \langle \dot{h}^2 \rangle / 2\epsilon^2 \sim \chi^2_n$. While an avalanche is in the field of view of the scanner, the time for each grain to move past x_j is approximately 0.005 s $\ll \delta t$, while the time for the surface height to vary substantially, after averaging over individual grains, is of the order of 1 s $\gg \delta t$. Therefore, I expect the standard deviation of $h_{j,k}$ over timescales of δt to be on the order of half the diameter of the largest grains, $d_{\max} = 0.71$ mm. Supposing $h_{j,k+1} - h_{j,k}$ to be normally distributed, I have that $2n\delta t^2 \langle \dot{h}^2 \rangle / d_{\max}^2 \sim \chi_n^2$.

I register grains to be moving (respectively, static) when, after smoothing, $\langle \dot{h}^2 \rangle$ has a value more than 10 standard deviations away from the value expected for static (respectively, moving) grains. Specifically, I smooth $\langle \dot{h}^2 \rangle$ with a locally-weighted least-squares quadratic regression, with time span 1 s, and register an avalanche to have started (respectively, stopped) when, after a period in which grains in the scanner's field of view were static (respectively, moving), the smoothed value first exceeds (respectively, falls below) a critical value C_{move} (respectively, C_{stop}). Critical values are given by

$$C_{\text{move}} = \frac{2\epsilon^2}{\delta t^2}\left(1 + \sqrt{\frac{2}{n}}\right), \qquad C_{\text{stop}} = \frac{d_{\max}^2}{2\delta t^2}\left(1 - \sqrt{\frac{2}{n}}\right). \tag{A.2}$$

I define the time interval between avalanches as the time between one avalanche being registered to have stopped, and the subsequent avalanche being registered to have started. To remove the effect of individual outlying measurements, arising from misidentification of the surface by the scanner at a given time t_k, I exclude time intervals with a duration of less than 2 s.

A.1.2 Experiments with interrupted inflow and full-length height profiles

I detect the position of a stopped avalanche front on a stationary pile by considering the changes in surface height between each pair of consecutive full-length height profiles. After each avalanche has come to a stop, the laser profile scanner is moved by an overhead traverse between 28 fixed positions at distances X_i downslope, 75 mm apart, and at each position the scanner measures surface heights 20 times along a 120 mm section of the channel's centreline, at distances downslope $x_{i,j}$, constant to within 1 mm between consecutive height profiles. I calculate the mean heights over these 20 measurements to obtain a full-length height profile, and subtract the mean heights from the previous full-length height profile to obtain the changes in surface height, $\Delta h_{i,j}$. Due to error in $x_{i,j}$, $\Delta h_{i,j}$ has random variation from 0 of the order of the grain size even in the absence of a physical change in surface height, but only where an avalanche has passed is there systematic variation of $\Delta h_{i,j}$.

I register a stopped avalanche front where the change in local gradient exceeds a critical value. I smooth $\Delta h_{i,j}$ as a function of $x_{i,j}$ with a robust locally-weighted least-squares linear regression of span approximately 40 mm, assigning lower weight to outliers and neglecting data points outside 6 mean absolute deviations, and I interpolate with a cubic spline the change in surface height $\mathit{\Delta} h$ at 1 mm intervals along the entire profile. I calculate the local gradient $\mathit{\Delta}\theta$ of $\mathit{\Delta} h$ and identify as the location of a new stopped avalanche front any peak of $\mathit{\Delta}\theta$ with a magnitude greater than the difference between the grains' angle of repose θ_r and their maximum angle of stability, θ_m. For the construction sand I use this is 4°, while for my glass beads this is 2°. If no such peak exists I conclude that the avalanche propagated the entire length of the channel, leaving no stopped avalanche front.

To calculate the effective time intervals between avalanches, I use the measured time intervals $T_j(0)$ between the resumption of inflow and the start of an avalanche, index j. For each X, I let $j_k(X)$ be the index of the kth avalanche that propagates a distance greater than X downslope, and I note that the kth effective time interval between avalanches passing X is

$$T_k(X) = \sum_{j=j_k(X)+1}^{j_{k+1}(X)} T_j(0). \tag{A.3}$$

A.2 Data

The following tables list summary data for the experimentally-observed time intervals between avalanches. At distances X downslope, I observe a total of n intervals between avalanches, of which n_{QP} and n_{IR} are classified in the quasi-periodic and irregular regimes, respectively. In these regimes, the mean time intervals between avalanches are $\bar{T}_{QP}$ and $\bar{T}_{IR}$ respectively, and the standard deviations of the time intervals between avalanches, from these means, are $\mathit{\Delta} T_{QP}$ and $\mathit{\Delta} T_{IR}$, respectively.

X / mm	n	n_{QP}	$\bar{T}_{QP}$ / s	ΔT_{QP} / s	n_{IR}	$\bar{T}_{IR}$ / s	ΔT_{IR} / s
186.0	304	253	4.58	0.98	36	4.96	2.41
306.0	273	102	6.49	0.61	130	8.45	4.81
394.0	272	105	7.71	0.98	131	11.44	7.94
514.0	232	49	8.61	1.37	144	14.43	10.81
634.0	179	0	-	-	130	18.63	13.79
754.0	155	55	9.12	1.56	82	17.93	13.98
844.0	143	66	12.21	2.47	40	25.03	19.97
964.0	163	60	10.45	1.93	64	30.50	21.06
1084.0	140	25	9.64	0.98	75	33.39	26.90
1204.0	134	25	14.12	2.79	65	36.14	30.88
1294.0	181	91	11.84	2.81	41	34.39	36.12
1414.0	156	70	9.88	1.48	50	40.21	42.09
1534.0	163	92	12.24	2.70	39	44.06	38.68
1664.0	144	75	11.24	2.01	17	51.15	41.67
1974.0	107	15	8.90	0.67	43	46.85	43.95
2054.0	94	0	-	-	44	52.14	34.80

Table A.1: Avalanche interval statistics for a constant inflow, flux $Q = 3.05$ cm^{3}s^{-1}, of angular construction sand, mean particle diameter $\bar{d} = 0.47$ mm.

X / mm	n	n_{QP}	$\bar{T}_{QP}$ / s	ΔT_{QP} / s	n_{IR}	$\bar{T}_{IR}$ / s	ΔT_{IR} / s
181.5	380	238	41.93	8.93	95	34.95	19.81
351.5	405	55	26.55	4.91	282	42.61	28.03
521.5	272	0	-	-	219	63.91	49.16
681.5	204	0	-	-	159	83.22	70.59
881.5	168	0	-	-	106	106.54	81.30
1031.5	162	37	31.51	3.96	83	132.03	90.67
1201.5	112	0	-	-	72	149.04	104.65
1371.5	96	0	-	-	50	176.61	129.32
1541.5	98	0	-	-	54	171.02	145.92
1711.5	83	0	-	-	37	219.54	164.61
1800.0	243	159	23.83	4.66	62	185.80	195.11
1881.5	122	22	23.47	3.27	53	195.67	174.83

Table A.2: Avalanche interval statistics for a constant inflow, flux $Q = 0.9$ cm^{3}s^{-1}, of angular construction sand, mean particle diameter $\bar{d} = 0.47$ mm.

X / mm	n	n_{QP}	$\bar{T}_{QP}$ / s	ΔT_{QP} / s	n_{IR}	$\bar{T}_{IR}$ / s	ΔT_{IR} / s
181.5	404	53	8.45	1.82	350	7.98	3.12
186.0	404	53	8.45	1.82	350	7.98	3.12
306.0	354	52	8.61	2.28	301	9.26	3.77
351.5	331	52	8.61	2.28	278	10.03	4.54
394.0	308	52	8.61	2.28	255	10.94	5.63
514.0	257	52	8.61	2.28	204	13.67	8.71
521.5	253	52	8.61	2.28	200	13.94	9.14
634.0	216	52	8.61	2.28	163	17.11	12.75
681.5	206	52	8.61	2.28	153	18.23	14.12
754.0	193	52	8.61	2.28	140	19.92	15.54
844.0	174	52	8.61	2.28	121	22.94	19.20
881.5	166	52	8.61	2.28	113	24.57	20.56
964.0	159	52	8.61	2.28	106	26.01	22.49
1031.5	152	52	8.61	2.28	99	27.85	24.12
1084.0	147	52	8.61	2.28	94	29.33	25.15
1201.5	136	52	8.61	2.28	83	33.22	29.57
1204.0	136	52	8.61	2.28	83	33.22	29.57
1294.0	128	51	8.78	2.34	76	36.28	35.80
1371.5	123	51	8.78	2.34	71	38.83	36.32
1414.0	117	51	8.78	2.34	65	42.42	39.52
1534.0	110	51	8.78	2.34	58	47.54	45.68
1541.5	109	51	8.78	2.34	57	48.37	45.65
1664.0	101	51	8.78	2.34	49	56.27	48.56
1711.5	99	51	8.78	2.34	47	58.66	49.67
1800.0	97	51	8.78	2.34	45	61.27	51.90
1881.5	95	51	8.78	2.34	43	64.12	52.99
1974.0	93	50	8.96	2.52	42	65.64	52.98
2054.0	93	50	8.96	2.52	42	65.64	52.98

Table A.3: Avalanche interval statistics for an interrupted inflow, flux Q = 3.05 cm^{3}s^{-1}, of angular construction sand, mean particle diameter $\bar{d}$ = 0.47 mm.

X / mm	n	n_{QP}	$\bar{T}_{QP}$ / s	ΔT_{QP} / s	n_{IR}	$\bar{T}_{IR}$ / s	ΔT_{IR} / s
181.5	813	7	2.41	0.88	806	2.77	1.59
186.0	807	7	2.41	0.88	800	2.79	1.61
306.0	622	7	2.41	0.88	615	3.62	2.53
351.5	593	7	2.41	0.88	586	3.80	2.96
394.0	565	7	2.41	0.88	558	4.00	3.41
514.0	505	7	2.41	0.88	498	4.47	4.06
521.5	501	7	2.41	0.88	494	4.50	4.35
634.0	455	7	2.41	0.88	448	4.96	5.59
681.5	435	7	2.41	0.88	428	5.20	5.97
754.0	403	7	2.41	0.88	396	5.62	7.14
844.0	360	7	2.41	0.88	353	6.30	8.66
881.5	347	7	2.41	0.88	340	6.54	9.02
964.0	318	7	2.41	0.88	311	7.15	10.07
1031.5	295	7	2.41	0.88	288	7.72	11.21
1084.0	275	7	2.41	0.88	268	8.30	11.79
1201.5	244	7	2.41	0.88	237	9.38	13.05
1204.0	242	7	2.41	0.88	235	9.46	13.26
1294.0	222	7	2.41	0.88	215	10.34	14.54
1371.5	211	7	2.41	0.88	204	10.90	14.97
1414.0	205	7	2.41	0.88	198	11.23	15.34
1534.0	183	7	2.41	0.88	176	12.64	16.89
1541.5	183	7	2.41	0.88	176	12.64	16.89
1664.0	164	7	2.41	0.88	157	14.17	17.99
1711.5	162	7	2.41	0.88	155	14.35	18.10
1800.0	155	7	2.41	0.88	148	15.03	18.56
1881.5	149	7	2.41	0.88	142	15.66	19.05
1974.0	147	7	2.41	0.88	140	15.89	19.16
2054.0	145	7	2.41	0.88	138	16.12	19.21

Table A.4: Avalanche interval statistics for an interrupted inflow, flux Q = 1.22 cm^{3}s^{-1}, of spherical glass beads, mean particle diameter $\bar{d}$ = 0.22 mm.

A.3 Statistical tests

A.3.1 R^2 value

Considering the quasi-periodic (respectively, irregular) regime, I conduct a linear regression of the non-dimensionalized mean intervals between avalanches $Q\bar{T}(X)/d^3$ on distances downslope X. I consider those values of $X \in [400, 2000]$ for which quasi-periodic (respectively, irregular) avalanches were observed in an experiment with a constant inflow of construction sand and with the laser profile scanner fixed at position X, whether with $Q = 3.05$ cm^{3}s^{-1} or with $Q = 0.9$ cm^{3}s^{-1}. For each X, I use the values of $Q\bar{T}/d^3$ arising from the experiments with a) a constant inflow of grains, b) an interrupted inflow of sand, and c) an interrupted inflow of glass beads. $\bar{T}$-values are listed in section A.2.

For the quasi-periodic regime, the 98% confidence interval for the best-fit gradient is $[-49, 28]$ mm^{-1} (under the assumption of independent, normally-distributed errors) and the coefficient of determination $R^2 = 0.011$, demonstrating that the data are consistent with $Q\bar{T}/d^3$ being constant within the considered range of X. For the irregular regime, the 98% confidence interval for the $Q\bar{T}/d^3$-intercept is $[-1.7 \times 10^5, 0.14 \times 10^5]$ and, restricting to an intercept of 0, the coefficient of determination $R^2 = 0.93$, demonstrating that the data are consistent with the model $Q\bar{T}/d^3 \propto X$ within the considered range of X.

A.3.2 Hypothesis tests

I conduct likelihood ratio hypothesis tests to determine whether my observations $Q\bar{T}/d^3$ of the non-dimensional expected intervals between avalanches, QT/d^3, are consistent with the hypotheses that the underlying probability density of avalanches stopping a distance X downslope is zero in the quasi-periodic regime and proportional to X^{-2} in the irregular regime. Under these hypotheses, QT/d^3 will be constant in the quasi-periodic regime and proportional to X in the irregular regime. As the probability density must be non-negative, the probability of a given avalanche stopping before X must monotonically increase with X and so, since all avalanches propagate from the top of the channel, the frequency with which avalanches pass X must monotonically decrease with X. Therefore, my alternative hypotheses are that the non-dimensional mean intervals between avalanches are monotonically increasing functions of X.

As in section A.3.1, I consider those values of $X \in [400, 2000]$ for which relevant data exist from an experiment with a constant inflow of grains, and consider all available data for each such X (see section A.2). I assume that, for a given X, the non-dimensional intervals observed in different experiments have equal means, as justified by Welch's tests on the data. Motivated by the central limit theorem, I further assume that the observed means are normally distributed about the underlying expectation, with variances given by $Q_\alpha^2 \mathrm{Var}_k(T_{\alpha,k}(X))/d_\alpha^6 n_\alpha(X)$ for indices α and k corresponding to different experiments and different intervals observed within an experiment, respectively.

For the quasi-periodic regime, I consider the hypotheses $H_0 : QT(X)/d^3 = A$, for some parameter $A \geq 0$, and $H_1 : QT(X)/d^3$ is a monotonically increasing function of X, taking otherwise-arbitrary values $QT(X_j)/d^3$ at the 14 distances downslope X_j at which measurements are taken. Calculating the maximum likelihoods of measuring the observed values $Q\bar{T}/d^3$ under each hypothesis, the ratio of the maximum likelihood under H_0 to that under H_1 is $\Lambda = 0.37$. Since a constant function is at the extreme of monotonicity, the one-dimensional parameter space of H_0 lies on the boundary of the 14-dimensional parameter space of H_1. In this situation, Chernoff's extension [71] of Wilk's theorem states that, if H_0 is true, the approximate distribution from which $\lambda = -2\log\Lambda$ is taken is given by a 50% chance that $\lambda = 0$ and a 50% chance that $\lambda \sim \chi^2_{13}$[a]. Under H_0, the probability of having obtained a more extreme value of λ is therefore $p = 0.5$, and so my data are consistent with H_0.

For the irregular regime, I consider the hypotheses $H_0 : QT(X)/d^3 = BX$, for some parameter $B \geq 0$, and $H_1 : QT(X)/d^3$ is a monotonically increasing function of X, taking otherwise-arbitrary values at the 22 values of X at which measurements are taken. Using the same framework as above, I find that the likelihood ratio of H_0 to H_1 is equal to $\Lambda = 7.5 \times 10^{-5}$. This time, however, the parameter space corresponding to H_0 lies in the interior of that corresponding to H_1 and the difference in the dimensionality of the parameter spaces is 21. Therefore, Wilk's theorem states that, if H_0 is true, the distribution of Λ over multiple experiments would be $\lambda = -2\log\Lambda \sim \chi^2_{21}$[303]. Under H_0, the probability of a more extreme value of Λ than that I observed is therefore $p = 0.59$, and so my data are consistent with H_0.

---

[a] Heuristically, if H_0 is true, there is a 50% chance of a monotonically decreasing function $QT(X)/d^3$ being a better fit than a monotonically increasing function, in which case the constraint of H_1 would force $QT(X)/d^3 =$ const. to maximise likelihood under H_1, so that $\lambda = 0$. Otherwise, the logic of Wilk's theorem applies, as described in section 3.3.

Appendix B

Supplementary Material for Chapter 3: The emplacement of strata by avalanches

B.1 Image processing

Stratum widths are extracted from each 1536 × 2048 pixel RGB image by converting each to a greyscale image in which blue-dyed grains are distinct; cross-correlating this greyscale image with a kernel corresponding to an idealised stratum; taking a vertical intensity profile across the convolution product; removing any lighting-related linear trend; and calculating the distance between local maxima in this detrended intensity profile.

First, I convert each image to greyscale. Writing $I^A_{j,k}$ for the intensity of channel $A \in \{R, G, B\}$ at the jth pixel downslope and kth pixel normal to the channel's base, I define the binary image B as the intensity of the blue colour channel, as a proportion of total luminosity,

$$B_{j,k} = \frac{I^B_{j,k}}{\sum_A I^A_{j,k}}. \tag{B.1}$$

With B having mean $\bar{B}^L = 0.230 \pm 0.012$ in regions of solely small, undyed grains and mean $\bar{B}^S = 0.429 \pm 0.011$ in regions of solely large, blue-dyed grains, the greyscale image may be used to estimate the local concentration of large grains $\bar{\phi}^L$. Packing fraction doesn't change significantly throughout the image, so the mean of B in a given region is expected to be linear in the visible area of large, blue-dyed grains within that region, and hence in the local volume fraction of large grains. We can therefore make the approximation

$$\bar{\phi}^L = \frac{\bar{B} - \bar{B}^S}{\bar{B}^L - \bar{B}^S}. \tag{B.2}$$

The segregation of large grains to the channel's sidewalls prevents me from calculating an exact calibration curve for this volume fraction.

Calibration of image scale, using a metre rule within the channel, shows the image's scale to be uniform in the image to within 2%, consistent with the precision of the camera's rotational alignment and its distance from the channel, while the angle in images of the channel's base demonstrates photographs to be inclined $\theta_{\mathrm{err}} = 0.74 \pm 0.07°$ more steeply about the cross-channel axis than the channel's inclination θ_r^S. Each pixel is, therefore, 0.117 ± 2 mm wide and high and I may define coordinates $x_{j,k}$ and $y_{j,k}$ that are aligned with the true channel inclination and perpendicular to it, respectively, at θ_{err} to the primary axes of the image. With respect to these coordinates, I define a 2-dimensional kernel K with a rectangular profile in x, of width $\mathit{\Delta} X = 100$ mm, and a parabolic profile in y, of width the mean grain size $\bar{d}$:

$$K_{j,k} = \max\left(\left[1 - H\left(|x_{j,k} - \mathit{\Delta} X/2|\right)\right]\left[1 - \left(y_{j,k}/\bar{d}\right)^2\right], 0\right). \tag{B.3}$$

Using this kernel, I detect strata. Calculating the cross-correlation matrix $C = K \star B$, I linearly interpolate an intensity profile $c(z)$ along a line at $\theta_r^S + \theta_{\mathrm{err}}$ to the original image's long axis, corresponding to a vertical line of points at equal distances downslope from the supply of grains. I perform a least squares linear regression of c against z, excluding points in the basal 15 mm of the deposit or within $\mathit{\Delta} X/2$, along the slope, of the image's boundary or the channel's end. Removing this linear trend, I find local maxima $(z_n^{\max})_n$ of the detrended intensity profile $\hat{c}(z)$ with a prominence greater than one third of the standard deviation of $\hat{c}$. These correspond to the layers of large, overlying grains of the avalanche-emplaced strata, and I calculate the perpendicular widths between these layers

$$Y_n = \left(z_{n+1}^{\max} - z_n^{\max}\right)\cos\theta. \tag{B.4}$$

This process is illustrated in Fig. B.1.

B.2 Data

The following tables list summary data for the experiment on stratification described in chapter 3, section 3.2.

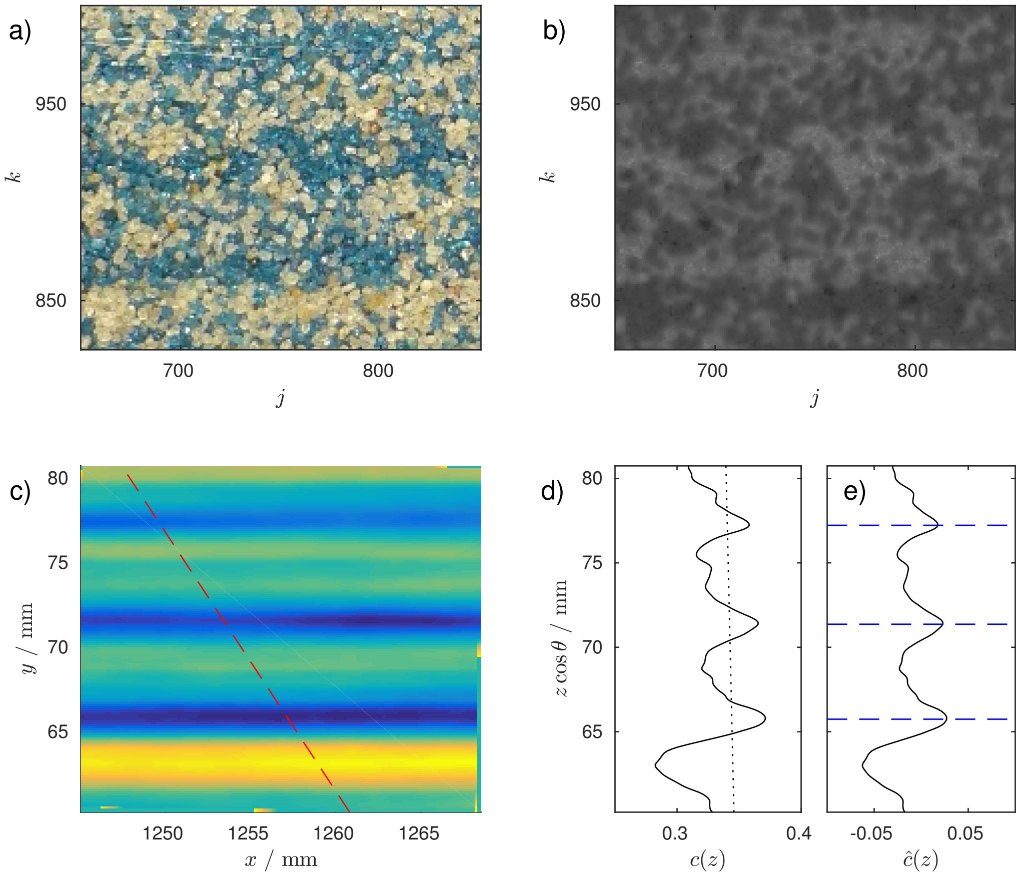

Figure B.1: Illustration image processing for extracting stratum widths. From the initial RGB image (example section shown in a), a greyscale image is produced in which large, blue-dyed grains are distinct (b). Cross-correlating this greyscale image with a kernel corresponding to an idealised stratum, the cross-correlation matrix (c) is linearly interpolated along a vertical line (red, dashed line) to extract a one-dimensional profile (d). Removing from this profile any linear trend resulting from variation in lighting (black, dotted line), strata are associated in the detrended profile (e) with prominent local maxima (blue, dashed lines).

X	n	$\bar{Y}$ / mm	$\mathit{\Delta}Y$ / mm
350	36	2.84	1.14
400	36	2.97	1.20
450	30	3.30	1.42
500	26	3.82	1.58
550	24	4.13	2.20
600	22	4.78	1.74
650	25	3.94	1.50
700	25	3.96	1.55
750	25	4.13	1.65
800	24	3.99	1.81
850	23	4.33	1.87
900	22	4.50	2.53
950	22	4.41	1.59
1000	24	4.05	2.11
1050	23	4.24	2.35
1100	26	3.79	1.63
1150	22	4.48	2.16
1200	23	4.26	1.82
1250	21	4.65	1.88
1300	17	5.46	2.14
1350	16	5.85	2.00
1400	17	5.50	2.27
1450	17	5.52	2.76
1500	14	6.65	2.54
1550	11	6.55	3.75
1600	8	6.46	3.82

Table B.1: Stratum width statistics. At distances X downslope, the image processing described in section B.1 detects n strata, of mean width $\bar{Y}$ and standard deviation in widths $\mathit{\Delta}Y$.

X_k	n	$\bar{N}$	ΔN
73	149	1.00	0.00
223	147	1.01	0.12
373	116	1.28	0.47
523	75	1.97	0.33
673	73	2.03	0.23
823	70	2.11	0.53
973	64	2.31	1.19
1123	53	2.79	1.92
1273	45	3.29	2.97
1423	37	3.95	3.84
1573	28	5.21	4.58

Table B.2: Approximate avalanche statistics. I record the avalanches passing marks at distances X_k downslope, as described in chapter 3, section 3.2. At each mark, the number of intervals between passing avalanches is n, the mean number of avalanches to occur in those intervals is $\bar{N}$, and the standard deviation of that number is ΔN.

APPENDIX C

Supplementary Material for Chapter 4: Observations of strata in sand dunes

C.1 Calculation of grain-size distribution from a cross-sectional-area distribution

To the best of my knowledge, it was Wicksell [300] who first solved the problem of calculating the distribution of sizes in a sample of spheres, from the distribution of cross-sectional areas visible in a section taken through that sample. Wicksell was concerned with follicles in the lymphatic tissue of the spleen, but his solution is equally applicable to sand grains. Here, I present this solution and show that the transformation between distributions is sensitive to error in the measurement of the cross-sectional-area distribution.

I assume a 3D sample consists of spherical grains, with probability density function for actual grain radii f_{R_A}. On taking a 2D section, a random set of grains will be cut and hence visible on the section and each such grain will be cut at a random perpendicular distance from its centre (Fig. C.1a). I assume that these processes are uncorrelated over a length scale significantly smaller than the size of the section and that the sample is homogeneous in the direction normal to the section.

The probability that a grain is cut is proportional to the length it presents in the direction normal to the section plane, so that, for expectation of actual grain radius $\mathbb{E}[R_A]$, the actual

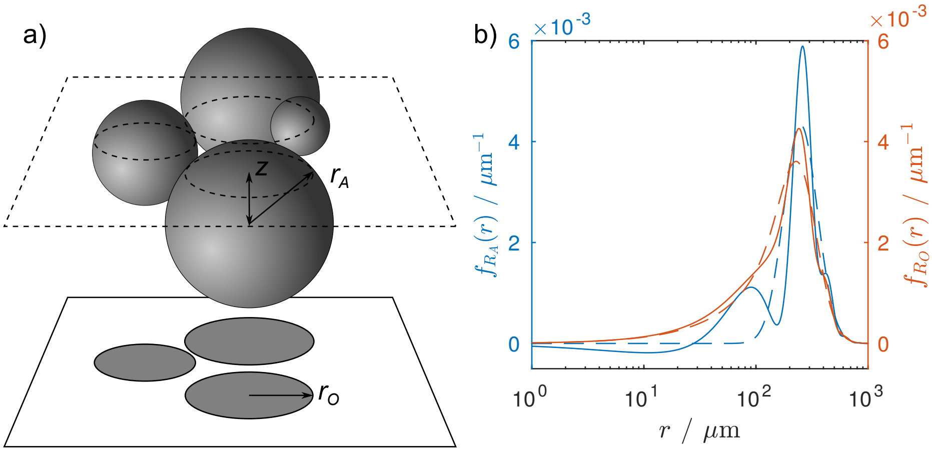

Figure C.1: Illustrations of the transformation between actual grain radii and observed cross-sectional radii, by schematic (a) and probability functions (b). In taking a planar section through a sample (a), any grain with radius r_O cut at a perpendicular distance z from its centre will have observed cross-sectional radius $r_O = \sqrt{r_A^2 - z^2}$. The probability density function of actual grain radii f_{R_A} is therefore transformed into a significantly different probability density function of observed cross-sectional radii f_{R_O}. The inverse transformation is sensitive to noise, so that any significant error in measuring f_{R_O} causes substantial error in the inferred f_{R_A}. An example is presented for a lognormal distribution, with dashed lines representing the underlying probability density functions and solid lines the measured/inferred functions.

distribution of radii of those grains visible on the section is

$$\hat{f}_{R_A}(r_A) = \frac{r_A f_{R_A}(r_A)}{\mathbb{E}[R_A]}. \tag{C.1}$$

Given that a grain, say with actual radius r_A, is visible on the section, its centre will be some minimum distance z from the plane, and so it will appear as a circular grain cross-section with observed radius $r_O = \sqrt{r_A^2 - z^2}$ for $0 \le z < r_A$. By homogeneity, over all grains of radius r_A, the minimal distances z are uniformly distributed between 0 and r_A, so the proportion of grains with observed cross-sectional radius greater than r_O is therefore

$$1 - F_{R_O}(r_O) = \int_{r_O}^{\infty} \frac{\sqrt{r_A^2 - r_O^2}}{r_A} \frac{r_A f_{R_A}(r_A)}{\mathbb{E}[R_A]} \mathrm{d}r_A. \tag{C.2}$$

Hence, the probability density function of observed cross-sectional radii f_{R_O} satisfies

$$\frac{2 f_{R_O}(r_O)}{r_O} = \int_{r_O}^{\infty} \frac{2 r_A}{\sqrt{r_A^2 - r_O^2}} \frac{f_{R_A}(r_A)}{r_A \mathbb{E}[R_A]} \mathrm{d}r_A. \tag{C.3}$$

Equation (C.3) is an Abel transform, so the distribution of actual grain radii may be reconstructed from the distribution of observed cross-sectional radii using the inverse Abel transform:

$$f_{R_A}(r_A) \propto r_A \int_{r_A}^{\infty} \frac{1}{\sqrt{r_O^2 - r_A^2}} \frac{d}{dr_O} \left[\frac{2 f_{R_O}(r_O)}{r_O} \right] \mathrm{d}r_O. \tag{C.4}$$

However, this inverse Abel transform is sensitive to noise (Fig. C.1b), so that significant error in the estimation of the cross-sectional area distribution will result in the inferred original grain-size distribution being entirely incorrect.

C.2 Locations of samples

Over three field expeditions, samples are extracted from four isolated barchan dunes, with heights H and widths between horn tips L. Dune heights, at the times of sample extraction, are calculated from theodolite surveys led by Michel Louge, in the same weeks that samples were extracted. Widths and geographical coordinates are extracted using satellite imagery from 2015, courtesy of Esri and DigitalGlobe. Data are presented in Table C.1.

Dune	H / m	L / m	Latitude / °	Longitude / °
A	5.1 ± 0.3	80 ± 2	25.009	51.341
B	28 ± 2	438 ± 3	25.012	51.332
C	3.14 ± 0.06	56 ± 2	25.010	51.341
D	6.0 ± 0.2	110 ± 2	25.021	51.344

Table C.1: Properties of the dunes studied in the field. I present heights H, widths L, and geographical coordinates of the dunes from which samples were extracted during fieldwork.

Samples were extracted in January 2015, January 2016, and January 2017, using the ‘aquarium’, ‘comb’, and ‘fine-toothed comb’ devices described in sections 4.2.2, 4.2.3, and 4.2.4, respectively, on dunes A, B, C, and D. For each field expedition and for each dune, the positions at which samples were taken are recorded relative to the midpoint of the brinkline of that dune during that field expedition, as calculated from theodolite survey data taken in the same week as the samples’ extraction, courtesy of Michel Louge. Cardinal directions are relative to true north.

For each sample taken from avalanche-emplaced cross strata, I estimate the distance X that the sand in that sample was transported by an avalanche, down the dune’s slip face, before its deposition. I assume that the sand remained in the same location after its deposition, while the dune migrated in the same downwind direction and maintained the same shape. For a sample extracted from the dune's wind-aligned centreline, at elevation $\varDelta z$ relative to the midpoint of the dune's brinkline, I therefore have $X = |\varDelta z| / \sin\theta_r$, for θ_r the angle of repose of the dune's slipface. For a sample extracted a perpendicular (crosswind) distance y from the dune's centreline, $X \approx \left[|\varDelta z| - \varDelta h(y)\right] / \sin\theta_r$, for $\varDelta h(y)$ the decline in height of the brinkline a distance y crosswind. I take downwind to be at a bearing of $\varPhi = 155 \pm 2°$ from true north; extract $\theta_r = 30.1 \pm 0.2°$ from the theodolite surveys led by Michel Louge; and take the approximation $\varDelta h = H\left[1 - \cos(\pi y / L)\right]$, for H and L defined above. This approximation agrees closely with the survey data and with the parametrisation of barchan dune shape suggested by Kroy et al. [200]. Errors in the estimation of X are calculated by carrying through standard errors in the measurement of H, L, $\varPhi$, θ_r, and extraction position.

Data are presented in Table C.2.

C.3 Selection of a mean diameter appropriate to water permeation

I wish to consider the association between spatial variation in the permeation of water and that in the grain size distribution, within a volume of sand. I therefore seek a statistic of the grain size distribution that is likely to be correlated with volumetric water content, in the form of a mean diameter.

I assume that the continuum approximation may be used and that I have flow at zero Reynolds number in a connected network of fluid, confined to the pores of a given volume of sand. I denote local volumetric water content w; time t; spatial position $\boldsymbol{x}$; water density ρ_w and dynamic viscosity μ; gravitational acceleration $\boldsymbol{g}$; and the hydraulic parameters permeability and capillary potential K and $\varPsi$, respectively, both assumed functions only of w and local volume-weighted particle size distribution $f_V(\boldsymbol{x})$, and therefore non-hysteretic. This is a strong restriction, since infiltration is isotropic and K increases strongly with w, implying preferential permeation to those regions into which permeation was originally fastest. Hysteresis in $\varPsi$ would result in these regions retaining more water than can be accounted for by a single-valued function $\varPsi(w)$. However, under this assumption, I may write the Richards equation [253, 255]

			Position relative to brinkline midpoint / m			
Year	Device	Dune	North	East	Elevation	X / m
2015	Aquarium	B	78.5 ± 0.5	−60.7 ± 0.5	−20.23 ± 0.08	39.7 ± 0.3
2015	Aquarium	B	13.7 ± 0.2	−6.6 ± 0.2	−2.50 ± 0.05	4.99 ± 0.10
2015	Aquarium	B	38.5 ± 0.8	−29.1 ± 0.8	−8.5 ± 0.2	16.7 ± 0.4
2015	Aquarium	B	88.4 ± 1.0	−90.6 ± 1.0	−25.6 ± 0.2	48.1 ± 0.7
2015	Aquarium	A	12.2 ± 0.2	−8.6 ± 0.2	−1.14 ± 0.05	2.22 ± 0.10
2015	Aquarium	A	6.2 ± 0.2	−5.3 ± 0.2	−0.44 ± 0.05	0.84 ± 0.10
2015	Comb	B	78.8 ± 0.2	−59.8 ± 0.2	−20.45 ± 0.05	40.2 ± 0.3
2015	Comb	B	78.8 ± 0.2	−59.8 ± 0.2	−20.55 ± 0.05	40.4 ± 0.3
2015	Comb	B	14.0 ± 0.5	−5.6 ± 0.5	−2.52 ± 0.08	-
2015	Comb	B	39.5 ± 1.1	−26.3 ± 1.1	−8.4 ± 0.2	16.6 ± 0.4
2015	Comb	B	39.5 ± 1.1	−26.3 ± 1.1	−8.5 ± 0.2	16.8 ± 0.4
2015	Comb	A	11.5 ± 0.5	−10.5 ± 0.5	−1.39 ± 0.09	2.61 ± 0.19
2016	Comb	A	18.1 ± 0.2	−20.6 ± 0.2	−2.09 ± 0.05	3.23 ± 0.17
2016	Comb	A	18.1 ± 0.2	−20.6 ± 0.2	−2.07 ± 0.05	3.19 ± 0.17
2016	Comb	A	7.6 ± 0.2	−26.6 ± 0.2	−2.08 ± 0.05	0.9 ± 0.3
2016	Comb	A	7.6 ± 0.2	−26.6 ± 0.2	−2.13 ± 0.05	1.0 ± 0.3
2017	Both combs	B	9.0 ± 0.2	−2.9 ± 0.2	−1.42 ± 0.05	2.82 ± 0.10
2017	Both combs	B	18.7 ± 0.2	−7.0 ± 0.2	−2.63 ± 0.05	5.25 ± 0.10
2017	Both combs	B	36.0 ± 0.2	−14.8 ± 0.2	−6.12 ± 0.05	12.20 ± 0.12
2017	Both combs	B	73.0 ± 0.2	−31.0 ± 0.2	−15.26 ± 0.05	30.4 ± 0.2
2017	Both combs	C	18.7 ± 0.2	−13.6 ± 0.2	−2.31 ± 0.05	4.42 ± 0.12
2017	Both combs	C	8.7 ± 0.2	−6.3 ± 0.2	−0.73 ± 0.05	1.42 ± 0.10
2017	Both combs	D	33.5 ± 0.2	−21.2 ± 0.2	−6.53 ± 0.05	12.90 ± 0.14
2017	Both combs	D	8.5 ± 0.2	−5.5 ± 0.2	−1.06 ± 0.05	2.11 ± 0.10

Table C.2: Positions of samples during fieldwork. For each set of samples, I list the year in which they were extracted, the device with which they were extracted, and the dune on which they were extracted. The position of extraction is recorded relative to the highest point on that dune's slipface and from this position I estimate the distance downslope X that the sample was deposited by an avalanche.

in the following form:

$$\frac{\partial w}{\partial t} = -\nabla_{\boldsymbol{x}} \cdot \left[\frac{1}{\mu} K(w, f_V)\,(\rho_w \boldsymbol{g} - \nabla_{\boldsymbol{x}} \Psi(w, f_V))\right]. \tag{C.5}$$

I first consider the initial infiltration of water in the field. A volume of ≈ 8 l of water is poured over a surface area of ≈ 40 cm $\times 20$ cm and penetrates to a depth ≈ 40 cm, implying a typical value $w \approx 0.25$ and a lengthscale of variation $L_0 = O(10^{-1})$ m. To compare the relative importance of terms in equation C.5, I consider typical magnitudes of its variables. I note that w is bounded below by its value before the addition of water, $w_{min} \approx 0.01$ [217], and that the surface is initially saturated. Therefore, for porosity ν, w has maximum value $1 - \nu \approx 0.5$, so that $\varDelta w = O(10^{-1})$. The density of water $\rho_w = O(10^3)$ m s^{-3} and its dynamic viscosity $\mu = O(10^{-3})$ kg m^{-1} s^{-1}, while the magnitude of gravitational acceleration $g \approx 10$ m s^{-1}. In well-sorted desert sand, I expect K to have a maximum value, at $w = 1 - \nu$, of $K_{sat} = O(10^{-10})$ m^2 [32], and a minimum value $K_{min} \approx 0$ m^2, since $w = w_{min}$ corresponds to the breaking of the fluid contact network and the cessation of flow. At a typical saturation $w = 0.25$, K will be reduced from its value at saturation by a factor of ≈ 10 [124], so that, typically, $K = O(10^{-11})$ m^2. $\varPsi$ also varies strongly with w, attaining its minimum magnitude of 0 at saturation, while its maximum magnitude is achieved at $w = w_{min}$. Assuming the latter to be the field capacity, I have $\varPsi_{max} = O(10^4)$ kg m^{-1} s^{-2} [254]. At the typical saturation $w = 0.25$, $\varPsi$ is also reduced from its maximum value by a factor of around 10, so that typically $\varPsi = O(10^3)$ kg m^{-1} s^{-2} [58]. Therefore, the timescale T_1 for the infiltration for water may be estimated as follows:

$$\frac{\varDelta w}{T_1} = O\left(\frac{1}{\mu L_0}\left(\rho_w \boldsymbol{g} K + \varDelta K \varDelta \varPsi / L_0 + K \varDelta \varDelta \varPsi / L_0\right)\right) \tag{C.6}$$

$$\therefore T_1 = O(10^{-1})/(O(10^{-3}) + O(10^{-1}) + O(10^{-2}))\ \mathrm{s} \tag{C.7}$$

$$= O(1)\mathrm{s} \tag{C.8}$$

A pit is dug after approximately 20 minutes, so I expect volumetric water content to have equilibrated before samples are taken, with the influence of gravity in that equilibration smaller than that of capillarity. With typical rates of evaporative water loss from wet sand in a desert region being O(1) cm day^{-1} [152], fluxes at the boundaries of the wetted sand are negligible, so fluid flux will be negligible throughout our domain. Therefore,

$$\rho_w \boldsymbol{g} - \nabla \varPsi \approx 0. \tag{C.9}$$

Having neglected hysteresis in K and $\varPsi$, I note that w and f_V vary on the scale of our measurements, $L_1 = O(10^{-2})$ m, if not on smaller scales. Therefore, the order of magnitude of $\nabla\varPsi$, were it not constrained by equation C.9, would be at least $O(10^6)$ kg m^{-2} s^{-2}. Meanwhile, $\rho_w \boldsymbol{g} = O(10^4)$ kg m^{-2} s^{-2}. As a result, the majority of the variation of w will be necessary to balance variation in f_V, rather than to balance gravity. Given the complexity of the functional relationship between $\varPsi$, w and f_V, the most accurate strategy would be to calculate water retention curves for local particle distributions g_N (either by simulation, or use of existing pedotransfer functions) and to then calculate the relative values of w necessary for $\varPsi$ to be constant.

However, another approach is to approximate Ψ by unrealistically supposing that, on a scale smaller than that over which I measure f_V, grains are perfectly separated by size and that the shapes and packings of grains within these separated regions are independent of that size. Dividing a control volume V into such regions, the volume of the region of grains of size between x and $x + \mathrm{d}x$ will be $f_V(x)V\mathrm{d}x$ and pore sizes will have an invariant distribution of sizes after scaling all lengths by x. Generalisation of an idealised capillary tube implies that $\Psi \propto 1/x$. To approximate the dependence of Ψ on w, I use the van Genuchten model [288] with residual water content $w_r \approx 0$, saturated water content $w_s = 1 - \nu$, and parameters $\alpha > 0$, $n > 1$:

$$w(\Psi) = w_r + \frac{w_s - w_r}{[1 + (\alpha\Psi)^n]^{1-1/n}} \tag{C.10}$$

$$\Psi(w) = -\frac{1}{\alpha}\left[\left(\frac{w_s - w_r}{w - w_r}\right)^{\frac{n}{n-1}} - 1\right]^{\frac{1}{n}} \tag{C.11}$$

$$\approx -\frac{1}{\alpha}\left(\frac{1-\nu}{w}\right)^{n-1}\left[1 - \left(\frac{w}{1-\nu}\right)^{\frac{n}{n-1}}\right]^{\frac{1}{n}} \tag{C.12}$$

Typical values of n are between 1 and 3, so for $w \not\approx 1-\nu$, the right-hand bracket is approximately equal to 1, and I recover that in our idealised region of equisized grains, $\Psi \approx 1/xw^{n-1}$. Therefore, for Ψ to be constant everywhere, I require that $w \propto x^{-1/(n-1)}$. The total volume of water in our idealised region will then be $\propto x^{-1/(n-1)} f_V(x)V\mathrm{d}x$, and so the mean volumetric water content in our control volume V will be:

$$\langle w \rangle_V \propto \int_0^\infty x^{-1/(n-1)} f_V(x)V\mathrm{d}x/V \tag{C.13}$$

$$\propto d^{-1}_{3-1/(n-1),3} = d^{-1}_{3,3-1/(n-1)}. \tag{C.14}$$

For well-sorted desert sand, $n = 2$ appears to be a typical value [134] (though the literature is far from rigorous), and so under these wildly inaccurate assumptions the volumetric water content will be inversely proportional to the Sauter diameter, $d_{3,2}$.

Appendix D

Supplementary Material for Chapter 5: The effect of sand dunes on seismic surveys

D.1 Details of SPECFEM3D

SPECFEM3D uses a continuous Galerkin method to formulate a discrete approximation to the continuous elastic wave equation. In a Garlerkin method, as applied to some second-order partial differential equation $\partial_t(\boldsymbol{u}, \dot{\boldsymbol{u}}) = (\dot{\boldsymbol{u}}, \mathscr{F}(\boldsymbol{u}, \dot{\boldsymbol{u}}))$, some spatial inner product $\langle \cdot, \cdot \rangle$ is used to express the problem in a weak formulation: for all t, for all test functions $\boldsymbol{w}(\boldsymbol{x})$

$$\langle \boldsymbol{w}, \partial_t \boldsymbol{u} \rangle = \langle \boldsymbol{w}, \dot{\boldsymbol{u}} \rangle, \qquad \langle \boldsymbol{w}, \partial_t \dot{\boldsymbol{u}} \rangle = \langle \boldsymbol{w}, \mathscr{F}(\boldsymbol{u}, \dot{\boldsymbol{u}}) \rangle. \tag{D.1}$$

Then, to discretise the problem, the system (D.1) is enforced only over some finite-dimensional subspace H_n. In a continuous Galerkin method, H_n is chosen to be a subspace of the Hilbert space H that defines the possible functions $\boldsymbol{u}$, under the regularity conditions and boundary conditions of the original, continuous problem. If H_n is spanned by some orthonormal basis of functions $\left\{ w_j(\boldsymbol{x}) \right\}_{j=1}^{n}$, then it is possible to write $\boldsymbol{u} = \boldsymbol{u}_n + \boldsymbol{u}'$ for $\boldsymbol{u}_n = \sum_{j=1}^{n} u_j \boldsymbol{w}_j$ and so the problem can be expressed in $2n$ first-order equations:

$$\partial_t u_j = \dot{u}_j, \qquad \partial_t \dot{u}_j \approx \langle \boldsymbol{w_j}, \mathscr{F}(\boldsymbol{u}_n, \dot{\boldsymbol{u}}_n) \rangle. \tag{D.2}$$

The accuracy of the approximation depends on the strength of the interaction in $\mathscr{F}$ between $\boldsymbol{u}'$ and the basis elements $\boldsymbol{w}_j$, whilst the proximity of the calculated solution $\boldsymbol{u}_n$ to the true solution

$\boldsymbol{u}'$ also depends on the choice of basis.

In SPECFEM3D, the basis is chosen so as to recover a spectral-element method. In such methods, the domain is divided into a finite set of volume elements $\{V_k\}$, defined by a user-generated mesh, and the kth element is associated with a set of basis vectors that are non-zero only within V_k[a]. In SPECFEM3D, each hexahedral volume element can be mapped to a unit cube, and the basis functions are each chosen to be the product of three Lagrange polynomials, of degree up to some n_k, in the coordinates of that cube, multiplied by the determinant of that mapping's Jacobian in such a way to preserve orthonormality.

Since $\boldsymbol{u}_n$ is therefore piecewise-polynomial, the inner product can be exactly calculated by using Gauss-Legendre quadrature within each volume element. In other words, the integral over space is calculated as a weighted sum of different values of $\boldsymbol{w}_j^\dagger \mathscr{F}$, with the points at which that product is evaluated and their associated weights determined by a set of rules. Points and weights are calculated on the unit cube to which each volume element maps and the Gauss-Lobatto rules are used to determine the points and weights to be used along each of that cube's axes, so that the endpoints of each edge are included. SPECFEM3D permits specification of the number of points used along the length of each volume element and I set this value to be 6. Exact integration is therefore possible for polynomials of degree up to 9 and so, given that $\boldsymbol{u}$ appears in $\mathscr{F}$ only linearly and via spatial derivatives, is possible for spectral elements of degree $n_k = 5$.

Despite consisting of a finite number of volume elements, SPECFEM3D is able to approximately simulate an infinite domain, using Convolutional Perfectly-Matched Layers (CPML) to absorb any waves propagating outwards at the exterior boundaries. Perfectly-Matched Layers consist of additional layers of volume elements, adjoining these boundaries. In these layers, all properties match those of the neighbouring, simulated domain, except that the numerical scheme approximates equations in which, in the frequency domain, $s(\omega, x)^{-1}\partial_x$ takes the place of ∂x, for angular frequency ω and coordinate normal to the boundary x. By choosing an appropriate function $s(\omega, x)$, any outwards-propagating plane wave solution must then have an amplitude that decays exponentially with x, but many such implementations of Perfectly-Matched Layers are prone to numerical instability. This is avoided by CPML, which use a specific form of function s and for which the numerical scheme is derived by transforming the

---

[a] By comparison, in a conventional finite-element method, each volume element is associated with a single value, equivalent to a single-element basis. In a fully spectral method, only a single volume element is used.

frequency-domain equations back into the time domain and calculating the convolution product $\tilde{s}^{-1} * \partial_x$.

D.2 Mesh refinement study

I verify the numerical accuracy of my simulations by conducting a mesh refinement study on a quasi-2D model of a transverse dune, with profile given by the midline of my original barchan dune model. The mesh geometry, shown in Figure D.1a, is 200 m long, 200 m wide, and 70 m deep, with CPML 25 m thick on each side and 30 m deep at its base. The dune geometry is defined by a straight brinkline along the mesh's centre, at a height of $H = 10$m, and by constant slope angles on the windward and leeward faces of 10° and 30° respectively. Velocities of the P and S waves are 1000 and 600 m s^{-1} in the desert floor, and 350 and 180 m s^{-1} in the dune. Density is everywhere 2500 kg m^{-3}. I simulate point forces 50 m upwind of, below, and 50 m downwind of the brinkline, acting vertically 1 m below the surface with Ricker function waveforms, central frequency 10 Hz and amplitude 10^5 N. Synthetic seismograms are recorded along a surface receiver line on the desert floor, transverse to the crest, with sources 50 m offline. The simulation duration is 2.4 s.

Varying the interval between mesh points δx, with a proportionate time step, I find that error in displacement decays as $\delta x^{2.9 \pm 0.3}$, with $\delta x = H/2$ sufficient for 10% accuracy. An example of the convergence of simulated displacement is shown in Figure D.1b, with the decay of mean squared error in displacement depicted in Figure D.1c.

D.3 Assessment of CPML efficiency

I assess the efficiency of my convolutional perfectly-matched boundary layers (CPML) by comparing my simulations to analytic solutions in the case of a point force on a homogeneous halfspace. I use a mesh 400 m long, 400 m wide, and 100 m deep, with typical mesh spacing 5 m and CPML 4 grid points thick on each side, and with constant velocities of P and S waves, 1000 m s^{-1} and 600 m s^{-1}, respectively. I simulate a vertical point force 100 m downwind of the centre of the mesh's surface, at a depth of 1 m and with a delta function waveform, and consider receiver locations at the surface, 180 m from the centre and at 5° azimuthal intervals. The duration of the simulation is 6 s. I convolve synthetic seismograms with Gabor

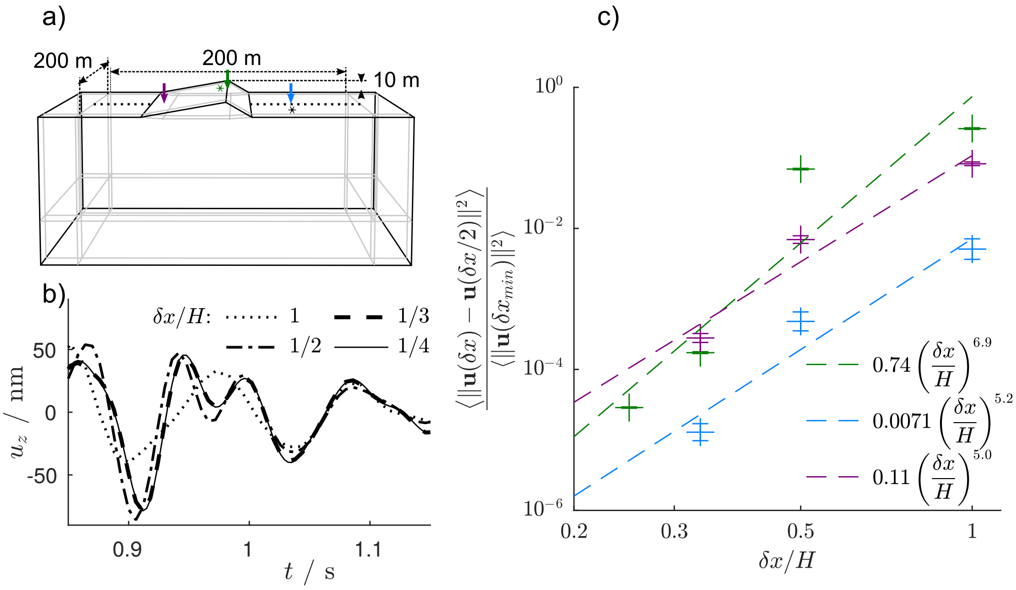

Figure D.1: Numerical convergence in a quasi-2D model. A schematic (a) indicates the locations of sources (↓, with a burial of 1 m) and receivers (■, at the surface). Simulated displacements converge with decreasing interval between mesh points δx, with an example presented (b) for the source receiver pair marked by $*$ in panel a. To analyse this convergence, I plot (c) the mean over time t of squared error in simulated displacement $\boldsymbol{u}(t; \delta x)$, normalised in each case by my best estimate of mean squared displacement. Colours correspond to the source locations in **a**, while error bars are the standard error over the 26 receiver locations.

wavelets, as specified by equation 5.4 with centre frequencies from $f_0 = 6$ Hz to $f_0 = 81$ Hz, and calculate the total energy flux $J_{\text{obs}}(\boldsymbol{x}_R, f_0)$ past each receiver location for each centre frequency. I compare the results to the analytically-derived net energy fluxes for Rayleigh waves, in the same situation, in the cases of a) perfectly-absorbing boundaries ($J_{\text{abs}}(\boldsymbol{x}_R, f_0)$ and of b) perfectly-reflecting boundaries ($J_{\text{ref}}(\boldsymbol{x}_R, f_0)$), using the work of [232] and [258] and the method of images in the case of b).

Since Rayleigh waves dominate the signal received at the simulated receivers, a tight overestimate of the total reflected energy flux is given by $J_{\text{obs}} - J_{\text{abs}}$, and a tight underestimate of the worst-case total reflected energy flux is given by $J_{\text{ref}} - J_{\text{abs}}$. My lower bound for the efficiency of my CPML is therefore $1 - (J_{\text{obs}} - J_{\text{abs}})/(J_{\text{ref}} - J_{\text{abs}})$, and I find that at no receiver, and at no centre frequency analysed, does this fall below 99%.

Appendix E

Problems encounted during research

'[S]and. It's coarse and rough and irritating and it gets everywhere.'

Anakin Skywalker, *Star Wars: Episode II - Attack of the Clones*, dir. George Lucas

E.1 Problems encountered in association with chapter 2

In seeking to describe avalanches on the surface of a channelised grain pile, the central unsolved problem of my work is the deterministic prediction of avalanche lengths in the regime of irregular avalanches, most of which stop partway down the channel's length. In the attempt to predict these lengths, I have tried:

1) Using, in the irregular regime, the overrunning-mobilisation model described in section 2.2 to predict the length of each avalanche, from:
    a) the positions of stopped avalanche fronts after the previous avalanche and the time interval between the two avalanches
    b) Monte Carlo simulations, using the positions of stopped avalanche fronts after the previous avalanche and random distributions of the time interval between avalanches.
2) Supposing, in the simplest case in which no avalanches are overrun, that an avalanche will stop when a critical value is reached of:
    a) local slope $\theta(X)$
    b) fall angle $\theta_{\text{fall}}(X)$ (arctan of the gradient of the line of best fit to the surface profile, from the avalanche's starting point to its current position)

    c) variance $\sigma^2(X)$ of surface height from that line of best fit
    d) a function of the above three.
3) Using the full profile as an initial condition, simulating the evolution of each avalanche's kinetic energy in a block model, using experimentally-motivated parameter values and:
    a) a depth, width and length-averaged model with Coulomb friction and constant shear rate throughout the flow, corresponding to averaging over each avalanche's length the equations of Douady et al. [92].
    b) a depth, width and length-averaged model corresponding instead to the depth-averaged model of Capart et al. [60].
    c) an heuristic model, with mass $\sim$ energy^m and the rate of dissipation with distance $\sim$ energy^n for m, n derived from various different assumptions of internal velocity profiles and stresses, and with parameters chosen by fitting.
4) Simulating the full partial differential equations described by Capart et al. [60], taking as an initial condition the measured profile of the grainpile before each avalanche, and imposing a stopping condition.

The corresponding results of these attempts have been the following:

1) a) Weak, but highly significant, correlation, as described in section 2.2.
    b) Problems in assessing the model. No single statistic accurately represents the full distributions of simulated avalanche lengths, preventing a calculation of correlation. Under the overrunning-mobilisation model, a number of observed avalanche lengths occur with zero likelihood (e.g. where an avalanche encounters a region of low slope and stops soon after overrunning a stopped front, as at $t = 111$ s and $t = 123$ s in Fig. 2.4a). This prevents calculation of a likelihood ratio.
2) No stopping criterion. While each avalanche tends to stop when it encounters low values of θ and θ_{fall} or high values of σ^2, there is no easily definable (and, indeed, no star-convex) surface that defines a stopping criterion for any significant fraction of the avalanches.
3) Poor prediction of avalanche lengths, even in the simplest case in which no stopped avalanche fronts are present. After fitting, model iii often provides accurate predictions, but predictions are inaccurate sufficiently often for there to be no significant correlation between predictions and observed avalanche lengths.

4) No predictive power, and a tendency to instability of the equations (likely due to the ill-posedness as $I \to 0$ of the $\mu(I)$ rheology and its linear approximation, as observed by Barker et al. [28]).

More minor problems were encountered when conducting experiments with glass beads of average diameter $\bar{d} = 0.22$ mm. Firstly, such grains are affected by ambient humidity, with exposed surfaces forming a cohesive crust if left at humidities higher than approximately 35% and dependence of repose angles on humidity even at lower humidities. Working in a laboratory without controlled humidity, experiments could only be conducted in certain weather conditions. Secondly, with such grains I was unable to test my model for transitions between the irregular and quasi-periodic regimes. As a result of the small size of these grains, variation in slope variability σ^2 was comparable to the error in profile measurements with the laser profile scanner.

E.2 Problems encountered in association with chapter 3

While experimentally investigating stratification, the most time-consuming problem I encountered was the selection of appropriate grains. In order for strata to be visible through the sidewalls of the channel, large and small grains have to segregate within the avalanche, but excessively fast segregation results in small grains becoming almost entirely concentrated close to the point of inflow and/or large grains becoming almost entirely concentrated at the bottom of the channel. Previous authors have suggested that segregation occurs only when the ratio d_L/d_S of a large grain's diameter to a small grain's diameter is greater than approximately 1.3 [136, 266], with segregation rate rapidly increasing with d_L/d_S thereafter. Consequently, it is difficult to achieve visible strata if a small range of values of d_L/d_S exist within the flow, as implied when both large and small grains have narrow size distributions.

Using grains with wider size distributions leads to slightly less clear layers, but also complicates the selection of inflow rates. Since large grains become overrepresented at the channel's sidewalls, it is necessary to use an inflow rate of large grains much smaller than that of small grains. However, the total inflow rate must be small for the system to have a separation of timescales between avalanching and inflow, while the smallest grains must be sufficiently large for cohesion to be negligible, leading to difficulties in avoiding jamming at the larger grains' point of inflow.

Due to these two problems, all of my many experiments using well-sorted glass beads failed to produce strata that were visible the entire length of the channel.

E.3 Problems encountered in association with chapter 4

In field measurements of grain size distributions, the most significant problem I encountered was the difficulty of analysing samples taken with the 'aquarium' device described in section 4.2.2. Laboratory tests of resination had shown that both water-based food dye and acrylic paint could be mixed into the resin before addition of the accelerator and would penetrate along with it into sand samples. However, these tests were conducted with dry construction sand rather than slightly moist dune sand and, in the field, neither pigment penetrated into samples. Consequently, no function of each microscope image's colour channels differs sufficiently between grains and resin for thresholding to accurately separate the two. This is especially true given grain imperfections and variations in lighting that filtering can compensate for only partially. Errors in thresholding can be manually fixed and then grain cross-sections automatically calculated from the binary images using ImageJ [250], but this process is less accurate than fully-manual grain identification and is not sufficiently faster to be practical. To identify grains quickly and fully automatically, ImageJ can be used to fix incorrectly-neglected internal grain imperfections (by filling holes) and to separate grains from each other (by 'watershedding'), but the resulting errors are large. If grain contacts form a ring then filling holes incorrectly merges several grains together, while imperfections on grain edges are not fixed by hole-filling and lead to single grains being divided by watershedding. The process and its flaws are illustrated in Fig. E.1.

By contrast, the difficulty of analysing samples from the fine-toother comb device was logistical. The Malvern Instruments Mastersizer 2000 that was available in Cambridge was unable to detect the small grains that most affected water permeation, while the Single Particle Optical Sizer that could detect such grains was little-used and rarely functional. As a result, analyses of the samples from 2017 were performed by a professional technician in Rennes, Jean-Luc Métayer. This involved significant cost per sample and long delays, due to his other commitments, reducing the number of samples that could be analysed. Furthermore, difficulties in communication led to his neglecting all grains of diameter greater than 500 μm. Better planning of sample analysis might have avoided these problems.

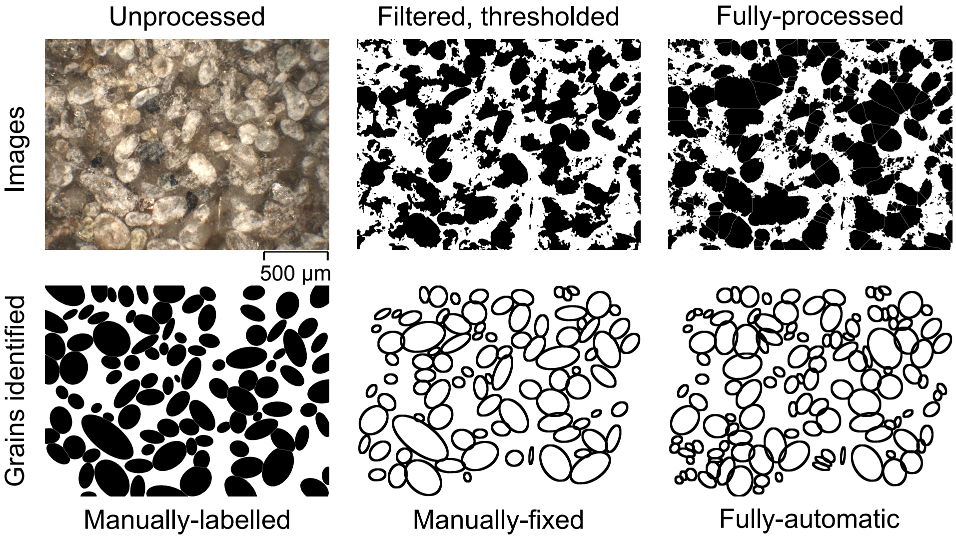

Figure E.1: Methods of extracting grain cross-sections from microscope images. Increased processing of microscope images (top row) of samples from the aquarium device, by sequential band-pass filtering, thresholding, hole-filling and watershedding, is illustrated left to right. Such processing increases the speed with which grain cross-sections (bottom row) can be identified from images, but decreases the accuracy of this identification.

E.4 Problems encountered in association with chapter 5

No major problems were encountered during numerical investigations of the effect of a dune on the propagation of surface waves. The greatest difficulty was the specification of meshes that approximated the shape of a given dunes, satisfied the conditions of SPECFEM3D, and had no element distorted enough that the simulation failed to converge. In particular, SPECFEM3D requires that every mesh element is hexahedral, with zero, four, or all eight of its vertices on any given boundary. Since the unstructured meshes that GMsh produces are tetrahedral and the splitting of tetrahedra into hexahedra can produce very distorted mesh elements, I found it easier to design structured meshes, but avoiding distortion requires care at e.g. the horns of a barchan dune.

A little care is also worthwhile to ensure that, when using high performance computing, the environment in which binaries are created matches that in which they are run. This was found to be a problem only when Schlumberger Cambridge Research changed compilers between one of my periods of work there and another.

Bibliography

[1] S. Abdul Majid, M. F. Graw, H. Nguyen, and A. G. Hay. Draft Whole-Genome Sequence of Urease-Producing Sporosarcina koreensis. *Genome Announcements*, 4(2):e00096–16, 2016.

[2] E. Agate and A. Brooks. *Sand Dunes: A Practical Handbook*. British Trust for Conservation Volunteers, 2000.

[3] K. Aki and P. G. Richards. *Quantitative Seismology: Theory and Methods*. Number v. 1 in A Series of books in geology. W. H. Freeman, 1980.

[4] M. Al-Ansary, M. C. Pöppelreiter, A. Al-Jabry, and S. R. Iyengar. Geological and physiochemical characterisation of construction sands in Qatar. *International Journal of Sustainable Built Environment*, 1(1):64–84, 2012.

[5] H. Al-Dabi, M. Koch, M. Al-Sarawi, and F. El-Baz. Evolution of sand dune patterns in space and time in north-western Kuwait using Landsat images. *Journal of Arid Environments*, 36(1):15–24, 1997.

[6] H. Al-Saad. Lithostratigraphy of the Middle Eocene Dammam Formation in Qatar, Arabian Gulf: effects of sea-level fluctuations along a tidal environment. *Journal of Asian Earth Sciences*, 25(5):781–789, 2005.

[7] A. A. Alghamdi and N. S. Al-Kahtani. Sand Control Measures and Sand Drift Fences. *Journal of Performance of Constructed Facilities*, 19(4):295–299, 2005.

[8] J. R. L. Allen. *Current Ripples*. North Holland Publishing Co., 1968.

[9] J. R. L. Allen. The diffusion of grains in the lee of ripples, dunes, and sand deltas. *Journal of Sedimentary Research*, 38(2):621, 1968.

[10] J. R. L. Allen. The Avalanching of Granular Solids on Dune and Similar Slopes. *The Journal of Geology*, 78(3):326–351, 1970.

[11] H. Almalki and T. Alkhalifah. Mapping the base of sand dunes using a new design of land-streamer for static correction applications. *Journal of Petroleum Exploration and Production Technology*, 2(2):57–65, 2012.

[12] R. S. Anderson. A theoretical model for aeolian impact ripples. *Sedimentology*, 34(5):943–956, 1987.

[13] B. Andreotti, A. Fourrière, F. Ould-Kaddour, B. Murray, and P. Claudin. Giant aeolian dune size determined by the average depth of the atmospheric boundary layer. *Nature*, 457:1120, 2009.

[14] A. Aradian, É. Raphaël, and P.-G. de Gennes. Thick surface flows of granular materials: Effect of the velocity profile on the avalanche amplitude. *Phys. Rev. E*, 60:2009–2019, 1999.

[15] I. S. Aranson, F. Malloggi, and E. Clément. Transverse instability of avalanches in granular flows down an incline. *Phys. Rev. E*, 73:050302, 2006.

[16] I. S. Aranson and L. S. Tsimring. Continuum theory of partially fluidized granular flows. *Phys. Rev. E*, 65:061303, 2002.

[17] I. S. Aranson, L. S. Tsimring, F. Malloggi, and E. Clément. Nonlocal rheological properties of granular flows near a jamming limit. *Phys. Rev. E*, 78:031303, 2008.

[18] M. I. Arran, 2016. Footage of simulated wave propagation in the vicinity of a dune is accessible online, at `https://drive.google.com/open?id=13-F9EgH7_fhLQ7cLfLEnGglceKgel5qy`.

[19] M. I. Arran, 2017. Footage of avalanching in each regime is available online, at `http://drive.google.com/open?id=17bfuJZljUnObsJpnpCo69FmrHZCb5T6r`.

[20] M. J. Aschwanden, N. B. Crosby, M. Dimitropoulou, M. K. Georgoulis, S. Hergarten, J. McAteer, A. V. Milovanov, S. Mineshige, L. Morales, N. Nishizuka, G. Pruessner, R. Sanchez, A. S. Sharma, A. Strugarek, and V. Uritsky. 25 Years of Self-Organized Criticality: Solar and Astrophysics. *Space Science Reviews*, 198(1):47–166, 2016.

[21] M. M. Ashour. Surficial deposits of Qatar Peninsula. *Geological Society, London, Special Publications*, 35(1):361–367, 1987.

[22] R. A. Bagnold. *The Physics of Blown Sand and Desert Dunes*. Methuen, 1941.

[23] R. A. Bagnold. Experiments on a Gravity-Free Dispersion of Large Solid Spheres in a Newtonian Fluid under Shear. *Proceedings of the Royal Society of London A: Mathematical, Physical and Engineering Sciences*, 225(1160):49–63, 1954.

[24] P. Bak, C. Tang, and K. Wiesenfeld. Self-organized criticality: An explanation of the 1/ f noise. *Phys. Rev. Lett.*, 59:381–384, 1987.

[25] P. Bak, C. Tang, and K. Wiesenfeld. Self-organized criticality. *Phys. Rev. A*, 38:364–374, 1988.

[26] S. S. Bang, J. K. Galinat, and V. Ramakrishnan. Calcite precipitation induced by polyurethane-immobilized Bacillus pasteurii. *Enzyme and Microbial Technology*, 28(4):404–409, 2001.

[27] S. G. Banham, S. Gupta, D. M. Rubin, J. A. Watkins, D. Y. Sumner, K. S. Edgett, J. P. Grotzinger, K. W. Lewis, L. A. Edgar, K. M. Stack-Morgan, R. Barnes, J. F. Bell, M. D. Day, R. C. Ewing, M. G. A. Lapotre, N. T. Stein, F. Rivera-Hernandez, and A. R. Vasavada. Ancient Martian aeolian processes and palaeomorphology reconstructed from the Stimson formation on the lower slope of Aeolis Mons, Gale crater, Mars. *Sedimentology*, 0(0), 2018.

[28] T. Barker, D. G. Schaeffer, P. Bohorquez, and J. M. N. T. Gray. Well-posed and ill-posed behaviour of the $\mu(I)$ -rheology for granular flow. *Journal of Fluid Mechanics*, 779:794–818, 2015.

[29] T. Barker, D. G. Schaeffer, M. Shearer, and J. M. N. T. Gray. Well-posed continuum equations for granular flow with compressibility and $\mu(I)$-rheology. *Proceedings of the Royal Society of London A: Mathematical, Physical and Engineering Sciences*, 473(2201), 2017.

[30] J. Barrière, C. Bordes, D. Brito, P. Sénéchal, and H. Perroud. Laboratory monitoring of P waves in partially saturated sand. *Geophys. J. Int.*, 191(3):1152–1170, 2012.

[31] J. Baxter, U. Tüzün, D. Heyes, I. Hayati, and P. Fredlund. Stratification in poured granular heaps. *Nature*, 391:136, 1998.

[32] J. Bear. *Dynamics of Fluids in Porous Media*. Environmental Science series. Dover Publications Inc., 1972.

[33] Y. Ben-Zion, K. A. Dahmen, V. Lyakhovsky, D. Ertas, and A. Agnon. Self-driven mode switching of earthquake activity on a fault system. *Earth and Planetary Science Letters*,

172(1–2):11–21, 1999.

[34] R. Berndtsson, K. Nodomi, H. Yasuda, T. Persson, H. Chen, and K. Jinno. Soil water and temperature patterns in an arid desert dune sand. *Journal of Hydrology*, 185(1):221–240, 1996.

[35] M. A. Bishop. Dune field development, interactions and boundary conditions for crescentic and stellate megadunes of the Al Liwa Basin, the Empty Quarter. *Earth Surface Processes and Landforms*, 38(2):183–191, 2013.

[36] L. Bocquet, J. Errami, and T. C. Lubensky. Hydrodynamic Model for a Dynamical Jammed-to-Flowing Transition in Gravity Driven Granular Media. *Phys. Rev. Lett.*, 89:184301, 2002.

[37] L. Bodet, A. Dhemaied, R. Martin, R. Mourgues, F. Rejiba, and V. Tournat. Small-scale physical modeling of seismic-wave propagation using unconsolidated granular media. *Geophysics*, 79(6):T323–T339, 2014.

[38] T. Börzsönyi, T. C. Halsey, and R. E. Ecke. Two Scenarios for Avalanche Dynamics in Inclined Granular Layers. *Phys. Rev. Lett.*, 94:208001, 2005.

[39] J.-P. Bouchaud, M. E. Cates, and P. Claudin. Stress Distribution in Granular Media and Nonlinear Wave Equation. *Journal de Physique I*, 5(6):639–656, 1995.

[40] J.-P. Bouchaud, M. E. Cates, J. Ravi Prakash, and S. Edwards. A model for the dynamics of sandpile surfaces. *Journal de Physique I*, 4(10):1383–1410, 1994.

[41] J.-P. Bouchaud, M. E. Cates, J. Ravi Prakash, and S. Edwards. Hysteresis and Metastability in a Continuum Sandpile Model. *Phys. Rev. Lett.*, 74:1982–1985, 1995.

[42] F. Bouchut, E. D. Fernández-Nieto, A. Mangeney, and P.-Y. Lagrée. On new erosion models of Savage–Hutter type for avalanches. *Acta Mechanica*, 199(1):181–208, 2008.

[43] T. Boutreux and P.-G. de Gennes. Surface Flows of Granular Mixtures: I. General Principles and Minimal Model. *Journal de Physique I*, 6(10):1295–1304, 1996.

[44] T. Boutreux, É. Raphaël, and P.-G. de Gennes. Surface flows of granular materials: A modified picture for thick avalanches. *Phys. Rev. E*, 58:4692–4700, 1998.

[45] M. Bouzid, A. Izzet, M. Trulsson, E. Clément, P. Claudin, and B. Andreotti. Non-local rheology in dense granular flows. *The European Physical Journal E*, 38(11):125, 2015.

[46] M. Bouzid, M. Trulsson, P. Claudin, E. Clément, and B. Andreotti. Nonlocal Rheology of Granular Flows across Yield Conditions. *Phys. Rev. Lett.*, 111:238301, 2013.

[47] M. Bouzid, M. Trulsson, P. Claudin, E. Clément, and B. Andreotti. Microrheology to probe non-local effects in dense granular flows. *Europhys. Lett*, 109(2):24002, 2015.

[48] M. Bretz, J. B. Cunningham, P. L. Kurczynski, and F. Nori. Imaging of avalanches in granular materials. *Phys. Rev. Lett.*, 69:2431–2434, 1992.

[49] J. Bridgwater, M. H. Cooke, and A. M. Scott. Inter-particle percolation: Equipment development and mean percolation velocities. *Trans. Inst. Chem. Eng.*, 56:157–167, 1978.

[50] J. Bridgwater and N. D. Ingram. Rate of spontaneous interparticle percolation. *Trans. Inst. Chem. Eng.*, 49:163, 1971.

[51] J. Bridgwater, N. W. Sharpe, and D. C. Stocker. Particle mixing by percolation. *Trans. Inst. Chem. Eng.*, 47:t114–t119, 1969.

[52] C. Bristow, J. Pugh, and T. Goodall. Internal structure of aeolian dunes in Abu Dhabi determined using ground-penetrating radar. *Sedimentology*, 43(6):995–1003, 1996.

[53] C. Bristow and P. Vermeesch. Methods to determine sand dune migration benefiting engineering and hydrocarbon companies. Technical report, University College London, Birkbeck College, 2014.

[54] J. M. Broder. Silos Loom as Death Traps on American Farms, 2012. Retrieved from www.nytimes.com.

[55] M. E. Brookfield. The origin of bounding surfaces in ancient aeolian sandstones. *Sedimentology*, 24(3):303–332, 1977.

[56] R. L. Brown. The Fundamental Principles of Segregation. *Journal of the Institute of Fuel*, 13, 1939.

[57] J. Bruch and M. Freeman. Migration of limesand dunes in Western Australia and their impacts. Technical report, Department of Mines and Petroleum, 2017.

[58] E. Buckingham. Studies on the movement of soil moisture. *Bureau of Soils Bulletin*, 38, 1907.

[59] A. P. Campbell and J. Bridgwater. The Mixing of Dry Solids by Percolation. *Trans. Inst. Chem. Eng.*, 51:72, 1973.

[60] H. Capart, C.-Y. Hung, and C. P. Stark. Depth-integrated equations for entraining granular flows in narrow channels. *Journal of Fluid Mechanics*, 765, 2015.

[61] M. Caponeri, S. Douady, S. Fauve, and C. Laroche. Dynamics of avalanches in a rotating

cylinder. In E. Guazelli and L. Oger, editors, *Mobile Particulate Systems*, volume 287, pages 331–365. Kluwer Academic Publishers, 1995.

[62] J. W. Carson and D. J. Goodwill. Understanding and Eliminating Particle Segregation Problems 1. *Bulk Solids Handling*, 6(1), 1986.

[63] M. E. Cates, J. P. Wittmer, J.-P. Bouchaud, and P. Claudin. Development of stresses in cohesionless poured sand. *Philosophical Transactions of the Royal Society of London A: Mathematical, Physical and Engineering Sciences*, 356(1747):2535–2560, 1998.

[64] M. E. Cates, J. P. Wittmer, J.-P. Bouchaud, and P. Claudin. Jamming, Force Chains, and Fragile Matter. *Phys. Rev. Lett.*, 81:1841–1844, 1998.

[65] M. E. Cates, J. P. Wittmer, J.-P. Bouchaud, and P. Claudin. Jamming and static stress transmission in granular materials. *Chaos: An Interdisciplinary Journal of Nonlinear Science*, 9(3):511–522, 1999.

[66] M. E. Cates, J. P. Wittmer, J.-P. Bouchaud, and P. Claudin. Jamming and stress propagation in particulate matter. *Physica A: Statistical Mechanics and its Applications*, 263(1):354–361, 1999. Proceedings of the 20th IUPAP International Conference on Statistical Physics.

[67] F. Charru, B. Andreotti, and P. Claudin. Sand Ripples and Dunes. *Annual Review of Fluid Mechanics*, 45(1):469–493, 2013.

[68] S. S. Chauhan. Desertification Control and Management of Land Degradation in the Thar Desert of India. *Environmentalist*, 23(3):219–227, 2003.

[69] D.-M. Chen, S. Wu, A. Guo, and Z. R. Yang. Self-organized criticality in a cellular automaton model of pulse-coupled integrate-and-fire neurons. *Journal of Physics A: Mathematical and General*, 28(18):5177, 1995.

[70] Y. Chen, S. Jiao, J. Ma, H. Chen, Y. Zhou, and S. Gan. Ground-Roll Noise Attenuation Using a Simple and Effective Approach Based on Local Band-Limited Orthogonalization. *IEEE Geoscience and Remote Sensing Letters*, 12(11):2316–2320, 2015.

[71] H. Chernoff. On the Distribution of the Likelihood Ratio. *Ann. Math. Statist.*, 25(3):573–578, 1954.

[72] P. Cizeau, H. A. Makse, and H. E. Stanley. Mechanisms of granular spontaneous stratification and segregation in two-dimensional silos. *Phys. Rev. E*, 59:4408–4421, 1999.

[73] P. Claudin, J.-P. Bouchaud, M. E. Cates, and J. P. Wittmer. Models of stress fluctuations in granular media. *Phys. Rev. E*, 57:4441–4457, 1998.

[74] E. Clément, J. Rajchenbach, and J. Duran. Mixing of a Granular Material in a Bidimensional Rotating Drum. *Europhys. Lett*, 30(1):7, 1995.

[75] L. Combee. Wavefield Scattering By a 2-D Near-surface Elliptic Anomaly. *1994 SEG Annual Meeting, 23-28 October, Los Angeles, California*, 1994.

[76] M. H. Cooke, J. Bridgwater, and A. M. Scott. Interparticle percolation: lateral and axial diffusion coefficients. *Powder Technology*, 21(2):183–193, 1978.

[77] A. Cordsen and M. Galbraith. Narrow- versus wide-azimuth land 3D seismic surveys. *The Leading Edge*, 21(8):764–770, 2002.

[78] C. Coulomb. Essai sur une application des règles de maximis et minimis à quelques problèmes de statique, relatifs à l'architecture, avec 2 planches. *Mémoires de mathématiques et de physique présentés à l'Académie royale des sciences par divers savants, et lus sans ses assemblées*, 7:343–382, 1773.

[79] D. R. Criswell, J. F. Lindsay, and D. L. Reasoner. Seismic and acoustic emissions of a booming dune. *Journal of Geophysical Research*, 80(35):4963–4974, 1975.

[80] M. D. Dabboor, A. Braun, and M. A. Kneen. Tracking sand dune migration in the Rub Al-Khali with ICESat laser altimetry. *International Journal of Remote Sensing*, 34(11):3832–3847, 2013.

[81] A. Daerr and S. Douady. Two types of avalanche behaviour in granular media. *Nature*, 399(6733):241–243, 1999.

[82] K. A. Dahmen, D. Ertas, and Y. Ben-Zion. Gutenberg-Richter and characteristic earthquake behavior in simple mean-field models of heterogeneous faults. *Phys. Rev. E*, 58:1494–1501, 1998.

[83] H. Darcy. *Les fontaines publiques de la ville de Dijon.* Dalmont, 1856.

[84] P. Dasgupta and P. Manna. Geometrical mechanism of inverse grading in grain-flow deposits: An experimental revelation. *Earth-Science Reviews*, 104(1–3):186–198, 2011.

[85] S. K. de Richter, G. L. Caër, and R. Delannay. Dynamics of rearrangements during inclination of granular packings: the avalanche precursor regime. *Journal of Statistical Mechanics: Theory and Experiment*, 2012(04):P04013, 2012.

[86] J. T. DeJong, M. B. Fritzges, and K. Nüsslein. Microbially Induced Cementation to Con-

trol Sand Response to Undrained Shear. *Journal of Geotechnical and Geoenvironmental Engineering*, 132(11):1381–1392, 2006.

[87] T. Dincer, A. Al-Mugrin, and U. Zimmermann. Study of the infiltration and recharge through the sand dunes in arid zones with special reference to the stable isotopes and thermonuclear tritium. *Journal of Hydrology*, 23(1):79–109, 1974.

[88] V. N. Dolgunin and A. A. Ukolov. Segregation modeling of particle rapid gravity flow. *Powder Technology*, 83(2):95–103, 1995.

[89] M. B. Donald and B. Roseman. Mixing and demixing of solid particles. *Br. Chem. Eng. 7*, 7:749, 1962.

[90] S. Dong, R. He, and G. T. Schuster. *Interferometric prediction and least squares subtraction of surface waves*, pages 2783–2786. 2006.

[91] Z. Dong, G. Chen, X. He, Z. Han, and X. Wang. Controlling blown sand along the highway crossing the Taklimakan Desert. *Journal of Arid Environments*, 57(3):329–344, 2004.

[92] S. Douady, B. Andreotti, and A. Daerr. On granular surface flow equations. *The European Physical Journal B - Condensed Matter and Complex Systems*, 11(1):131–142, 1999.

[93] J. A. Drahun and J. Bridgwater. The mechanisms of free surface segregation. *Powder Technology*, 36(1):39–53, 1983.

[94] B. Drossel. Self-Organized Criticality and Synchronization in a Forest-Fire Model. *Phys. Rev. Lett.*, 76:936–939, 1996.

[95] J. M. Drummond, R. Kasmi, A. Sakani, A. J. L. Budd, and J. W. Ryan. Optimizing 3-D seismic technologies to accelerate field development in the Berkine Basin, Algeria. *Geological Society, London, Special Publications*, 207(1):257–273, 2003.

[96] J. Duffy and R. D. Mindlin. *Stress-strain Relations and Vibrations of a Granular Medium*. Defense Technical Information Center, 1956.

[97] O. Durán, P. Claudin, and B. Andreotti. On aeolian transport: Grain-scale interactions, dynamical mechanisms and scaling laws. *Aeolian Research*, 3(3):243–270, 2011.

[98] O. Durán, P. Claudin, and B. Andreotti. Direct numerical simulations of aeolian sand ripples. *Proceedings of the National Academy of Sciences*, 111(44):15665–15668, 2014.

[99] C. M. Dury and G. H. Ristow. Radial Segregation in a Two-Dimensional Rotating Drum. *Journal de Physique I*, 7(5):737–745, 1997.

[100] A. N. Edwards and J. M. N. T. Gray. Erosion-deposition waves in shallow granular free-surface flows. *Journal of Fluid Mechanics*, 762:35–67, 2015.

[101] A. N. Edwards, S. Viroulet, B. P. Kokelaar, and J. Gray. Formation of levees, troughs and elevated channels by avalanches on erodible slopes. *Journal of Fluid Mechanics*, 823:278–315, 2017.

[102] A. N. Edwards and N. M. Vriend. Size segregation in a granular bore. *Phys. Rev. Fluids*, 1:064201, 2016.

[103] M. I. El-Sayed. Sedimentological characteristics and morphology of the aeolian sand dunes in the eastern part of the UAE, a case study from Ar Rub' Al Khali. *Sedimentary Geology*, 123(3–4):219–238, 1999.

[104] M. I. El-Sayed. The nature and possible origin of mega-dunes in Liwa, Ar Rub' Al Khali, {UAE}. *Sedimentary Geology*, 134(3–4):305–330, 2000.

[105] P. Embree, J. P. Burg, and M. M. Backus. Wide-band velocity filtering; The Pie-Slice process. *Geophysics*, 28(6):948–974, 1963.

[106] P. Evesque. Analysis of the statistics of sandpile avalanches using soil-mechanics results and concepts. *Phys. Rev. A*, 43:2720–2740, 1991.

[107] P. Evesque and J. Rajchenbach. Caractérisation d'avalanches de billes dans un cylindre tournant. *Comptes Rendus de l'Académie des sciences, Série 2*, 307:p223–226, 1988.

[108] Y. Fan, Y. Boukerkour, T. Blanc, P. B. Umbanhowar, J. M. Ottino, and R. M. Lueptow. Stratification, segregation, and mixing of granular materials in quasi-two-dimensional bounded heaps. *Phys. Rev. E*, 86:051305, 2012.

[109] M. Farthing and F. Ogden. Numerical Solution of Richards' Equation: A Review of Advances and Challenges. *Soil Science Society of America Journal*, 81(6), 2017.

[110] F. D. Felitta. Dark Night of the Scarecrow, 1981. Film.

[111] F. Ferris, L. Stehmeier, A. Kantzas, and F. M. Mourits. Bacteriogenic Plugging. In *4th Petroleum Conf. of the South Saskatchewan Section*, 1991.

[112] R. A. Fessenden. Method and apparatus for locating ore-bodies, 1917. US Patent 1,240,328.

[113] H. J. Finkel. The Barchans of Southern Peru. *The Journal of Geology*, 67(6):614–647, 1959.

[114] S. Fischer, M. E. Cates, and K. Kroy. Dynamic scaling of desert dunes. *Phys. Rev. E*,

77:031302, 2008.

[115] E. A. Flinn. Signal Analysis Using Rectilinearity and Direction of Particle Motion. *Proceedings of the IEEE*, 53(12):1874–1876, 1965. cited By 107.

[116] R. L. Folk. A Review of Grain-size Parameters. *Sedimentology*, 6(2):73–93, 1966.

[117] R. L. Folk and W. C. Ward. Brazos River bar; a study in the significance of grain size parameters. *Journal of Sedimentary Research*, 27(1):3, 1957.

[118] J. C. Fontes, M. Yousfi, and G. B. Allison. Estimation of long-term, diffuse groundwater discharge in the northern Sahara using stable isotope profiles in soil water. *Journal of Hydrology*, 86(3):315–327, 1986.

[119] W. S. Foo and J. Bridgwater. Particle Migration. *Powder Technology*, 36(2):271–273, 1983.

[120] F. Forghani and R. Snieder. Underestimation of body waves and feasibility of surface-wave reconstruction by seismic interferometry. *The Leading Edge*, 29(7):790–794, 2010.

[121] V. Frette, K. Christensen, A. Malthe-Sorenssen, J. Feder, T. Jossang, and P. Meakin. Avalanche dynamics in a pile of rice. *Nature*, 379(6560):49–52, 1996.

[122] R. Frigg. Self-organised criticality—what it is and what it isn't. *Studies in History and Philosophy of Science Part A*, 34(3):613–632, 2003.

[123] P. Gajjar and J. M. N. T. Gray. Asymmetric flux models for particle-size segregation in granular avalanches. *Journal of Fluid Mechanics*, 757:297–329, 2014.

[124] C. Gallage, J. Kodikara, and T. Uchimura. Laboratory measurement of hydraulic conductivity functions of two unsaturated sandy soils during drying and wetting processes. *Soils and Foundations*, 53(3):417–430, 2013.

[125] J. R. Garratt. Review: the atmospheric boundary layer. *Earth-Science Reviews*, 37(1):89–134, 1994.

[126] T. W. Garve. Segregation in bins. *J. Amer. Ceram. Soc.*, 80:666, 1925.

[127] T. W. Garve. Die Entmischung gekörnter Stoffe in Vorratsbehältern. *Keram. Rundschau Kunst-Keram.*, 44:231–234, 1936.

[128] E. Garzanti, P. Vermeesch, S. Andò, G. Vezzoli, M. Valagussa, K. Allen, K. Kadi, and A. Al-Juboury. Provenance and recycling of Arabian desert sand. *Earth-Science Reviews*, 120:1–19, 2013.

[129] GDR MiDi. On dense granular flows. *The European Physical Journal E*, 14(4):341–365,

2004.

[130] J. Geng, E. Longhi, R. P. Behringer, and D. W. Howell. Memory in two-dimensional heap experiments. *Phys. Rev. E*, 64:060301, 2001.

[131] J. Geng, G. Reydellet, E. Clément, and R. P. Behringer. Green's function measurements of force transmission in 2D granular materials. *Physica D: Nonlinear Phenomena*, 182(3):274–303, 2003.

[132] H. Gercek. Poisson's ratio values for rocks. *International Journal of Rock Mechanics and Mining Sciences*, 44(1):1–13, 2007.

[133] C. Geuzaine and J.-F. Remacle. Gmsh: a three-dimensional finite element mesh generator with built-in pre- and post-processing facilities. *International Journal for Numerical Methods in Engineering*, 79(11):1309–1331, 2009.

[134] B. Ghanbarian-Alavijeh, A. Liaghat, G.-H. Huang, and M. T. van Genuchten. Estimation of the van Genuchten Soil Water Retention Properties from Soil Textural Data. *Pedosphere*, 20(4):456–465, 2010.

[135] L. A. Golick and K. E. Daniels. Mixing and segregation rates in sheared granular materials. *Phys. Rev. E*, 80:042301, 2009.

[136] R. K. Goyal and M. S. Tomassone. Power-law and exponential segregation in two-dimensional silos of granular mixtures. *Phys. Rev. E*, 74:051301, 2006.

[137] Y. Grasselli and H. J. Herrmann. Experimental study of granular stratification. *Granular Matter*, 1(1):43–47, 1998.

[138] J. M. N. T. Gray. Particle Segregation in Dense Granular Flows. *Annual Review of Fluid Mechanics*, 50(1):407–433, 2018.

[139] J. M. N. T. Gray and C. Ancey. Segregation, recirculation and deposition of coarse particles near two-dimensional avalanche fronts. *Journal of Fluid Mechanics*, 629:387–423, 2009.

[140] J. M. N. T. Gray and V. A. Chugunov. Particle-size segregation and diffusive remixing in shallow granular avalanches. *Journal of Fluid Mechanics*, 569:365–398, 2006.

[141] J. M. N. T. Gray and K. Hutter. Pattern formation in granular avalanches. *Continuum Mechanics and Thermodynamics*, 9(6):341–345, 1997.

[142] J. M. N. T. Gray and A. R. Thornton. A theory for particle size segregation in shallow granular free-surface flows. *Proceedings of the Royal Society of London A: Mathematical,*

Physical and Engineering Sciences, 461(2057):1447–1473, 2005.

[143] G. Grinstein. *Generic scale invariance and self-organized criticality*, pages 261–293. Springer US, Boston, MA, 1995.

[144] D. F. Halliday, P. Bilsby, L. West, E. Kragh, and J. Quigley. Scattered ground-roll attenuation using model-driven interferometry. *Geophysical Prospecting*, 63(1):116–132, 2015.

[145] D. F. Halliday, A. Curtis, P. Vermeer, C. Strobbia, A. Glushchenko, D.-J. van Manen, and J. O. A. Robertsson. Interferometric ground-roll removal: Attenuation of scattered surface waves in single-sensor data. *Geophysics*, 75(2):SA15–SA25, 2010.

[146] Z. Han, T. Wang, Q. Sun, Z. Dong, and X. Wang. Sand harm in Taklimakan Desert highway and sand control. *Journal of Geographical Sciences*, 13(1):45–53, 2003.

[147] Z. Harari. Ground-penetrating radar (GPR) for imaging stratigraphic features and groundwater in sand dunes. *Journal of Applied Geophysics*, 36(1):43–52, 1996.

[148] B. O. Hardin and W. L. Black. Vibration Modulus of normally consolidated Clay. *J. Soil Mech. Found. Div., ASCE*, 95(SM2):353–369, 1968.

[149] J. F. G. Harris and A. M. Hildon. Reducing Segregation in Binary Powder Mixtures with Particular Reference to Oxygenated Washing Powders. *Industrial & Engineering Chemistry Process Design and Development*, 9(3):363–367, 1970.

[150] N. W. Hayman, L. Ducloué, K. L. Foco, and K. E. Daniels. Granular Controls on Periodicity of Stick-Slip Events: Kinematics and Force-Chains in an Experimental Fault. *Pure and Applied Geophysics*, 168(12):2239–2257, 2011.

[151] A. Hazen. *Some Physical Properties of Sands and Gravels*. 1892.

[152] D. H. R. Hellwig. Evaporation of water from sand, 1: Experimental set-up and climatic influences. *Journal of Hydrology*, 18(2):93–108, 1973.

[153] H. Henein, J. K. Brimacombe, and A. P. Watkinson. An experimental study of segregation in rotary kilns. *Metallurgical Transactions B*, 16(4):763–774, 1985.

[154] P. A. Hesp and K. Hastings. Width, height and slope relationships and aerodynamic maintenance of barchans. *Geomorphology*, 22(2):193–204, 1998.

[155] K. M. Hill, D. V. Khakhar, J. F. Gilchrist, J. J. McCarthy, and J. M. Ottino. Segregation-driven organization in chaotic granular flows. *Proceedings of the National Academy of Sciences*, 96(21):11701–11706, 1999.

[156] D. Hirshfeld and D. C. Rapaport. Molecular dynamics studies of grain segregation in sheared flow. *Phys. Rev. E*, 56:2012–2018, 1997.

[157] D. A. Holm. Desert Geomorphology in the Arabian Peninsula. *Science*, 132(3437):1369–1379, 1960.

[158] C. W. A. Holmes. The sampling of coal - II. *Colliery Engineering*, 11:42–44, 1934.

[159] J. Hommel, E. Lauchnor, A. Phillips, R. Gerlach, A. B. Cunningham, R. Helmig, A. Ebigbo, and H. Class. A revised model for microbially induced calcite precipitation: Improvements and new insights based on recent experiments. *Water Resources Research*, 51(5):3695–3715, 2015.

[160] Y. Hu, L. Wang, F. Cheng, Y. Luo, C. Shen, and B. Mi. Ground-roll noise extraction and suppression using high-resolution linear Radon transform. *Journal of Applied Geophysics*, 128:8–17, 2016.

[161] J. A. Hudson and L. Knopoff. Statistical properties of Rayleigh waves due to scattering by topography. *Bulletin of the Seismological Society of America*, 57(1):83–90, 1967.

[162] M. L. Hunt and N. M. Vriend. Booming Sand Dunes. *Annual Review of Earth and Planetary Sciences*, 38(1):281–301, 2010.

[163] R. E. Hunter. Basic types of stratification in small eolian dunes. *Sedimentology*, 24(3):361–387, 1977.

[164] R. E. Hunter. *Stratification styles in Eolian sandstones: some Pennsylvanian to Jurassic examples from the Western Interior, USA.*, volume 31, pages 315–329. Sepm Society for Sedimentary, 1981.

[165] R. M. Iverson. Elementary theory of bed-sediment entrainment by debris flows and avalanches. *Journal of Geophysical Research: Earth Surface*, 117(F3):n/a–n/a, 2012.

[166] R. M. Iverson and C. Ouyang. Entrainment of bed material by Earth-surface mass flows: Review and reformulation of depth-integrated theory. *Reviews of Geophysics*, 53(1):27–58, 2015.

[167] G. M. Jackson, I. M. Mason, and S. A. Greenhalgh. Principal component transforms of triaxial recordings by singular value decomposition. *Geophysics*, 56(4):528–533, 1991.

[168] P. S. Jackson and J. C. R. Hunt. Turbulent wind flow over a low hill. *Quarterly Journal of the Royal Meteorological Society*, 101(430):929–955, 1975.

[169] H. M. Jaeger, C.-h. Liu, and S. R. Nagel. Relaxation at the Angle of Repose. *Phys. Rev.*

Lett., 62:40–43, 1989.

[170] H. A. Janssen. Experiments on Corn Pressure in Silo Cells. *Zeitschr. d. Vereines deutscher Ingenieure*, 39:1045, 1895.

[171] A. Jawad Ali and R. A. Al-Ani. Sedimentological and geomorphological study of sand dunes in the Western Desert of Iraq. *Journal of Arid Environments*, 6(1):13–32, 1983.

[172] L. Jing, C. Y. Kwok, and Y. F. Leung. Micromechanical Origin of Particle Size Segregation. *Phys. Rev. Lett.*, 118:118001, 2017.

[173] P. Jop, Y. Forterre, and O. Pouliquen. A constitutive law for dense granular flows. *Nature*, 441(7094):727–730, 2006.

[174] T. Jotaki and R. Moriyama. On the Bottom Pressure Distribution of the Bulk Materials Piled with the Angle of Repose. *Journal of the Society of Powder Technology, Japan*, 16(4):184–191, 1979.

[175] S. Joussaume. Paleoclimatic tracers: An investigation using an atmospheric general circulation model under ice age conditions: 1. Desert dust. *Journal of Geophysical Research: Atmospheres*, 98(D2):2767–2805, 1993.

[176] L. P. Kadanoff, S. R. Nagel, L. Wu, and S.-m. Zhou. Scaling and universality in avalanches. *Phys. Rev. A*, 39:6524–6537, 1989.

[177] K. Kamrin and G. Koval. Nonlocal Constitutive Relation for Steady Granular Flow. *Phys. Rev. Lett.*, 108:178301, 2012.

[178] A. Kantzas, L. Stehmeier, D. F. Marentette, F. G. Ferris, K. N. Jha, and F. M. Maurits. A Novel Method of Sand Consolidation Through Bacteriogenic Mineral Plugging. In *CIM Paper No. 92-46*. Petroleum Society of Canada, 1992.

[179] D. V. Khakhar, J. J. McCarthy, and J. M. Ottino. Radial segregation of granular mixtures in rotating cylinders. *Physics of Fluids*, 9(12):3600–3614, 1997.

[180] G. A. Kiersch. Small-scale structures and other features of Navajo sandstone, northern part of San Rafael Swell, Utah. *AAPG Bulletin*, 34(5):923, 1950.

[181] W. J. H. King. The Nature and Formation of Sand Ripples and Dunes. *The Geographical Journal*, 47(3):189–207, 1916.

[182] D. M. Kingman, W. E. Field, and D. E. Maier. Summary of Fatal Entrapments in On-farm Grain Storage Bins, 1966-1998. *Journal of Agricultural Safety and Health*, 7(3):169–184, 2001.

[183] F. Kirchheimer. *On some further aspects of fan filtering*, pages 635–638. 1985.

[184] M. G. Kleinhans. Sorting in grain flows at the lee side of dunes. *Earth-Science Reviews*, 65(1–2):75–102, 2004.

[185] M. G. Kleinhans. Grain-size sorting on grainflows at the lee side of deltas. *Sedimentology*, 52(2):291–311, 2005.

[186] M. G. Kleinhans and T. W. J. V. Asch. Grain-size sorting and slope failure in experimental subaqueous grain flows. In *Powders and Grains 2005*, volume 2, pages 977–980, Dept. of Physical Geography, Fac. Geosciences, Utrecht University, Netherlands, 2005.

[187] M. G. Kleinhans, H. Markies, S. J. de Vet, A. C. in 't Veld, and F. N. Postema. Static and dynamic angles of repose in loose granular materials under reduced gravity. *Journal of Geophysical Research: Planets*, 116(E11), 2011.

[188] G. Kocurek. Interpretation of Ancient Eolian Sand Dunes. *Annual Review of Earth and Planetary Sciences*, 19(1):43–75, 1991.

[189] G. Kocurek and J. R. H. Dott. Distinctions and uses of stratification types in the interpretation of eolian sand. *Journal of Sedimentary Research*, 51(2):579–596, 1981.

[190] G. Kocurek. Significance of interdune deposits and bounding surfaces in aeolian dune sands. *Sedimentology*, 28(6):753–780, 1981.

[191] J. P. Koeppe, M. Enz, and J. Kakalios. Phase diagram for avalanche stratification of granular media. *Phys. Rev. E*, 58:R4104–R4107, 1998.

[192] D. Komatitsch, J. Ritsema, and J. Tromp. The Spectral-Element Method, Beowulf Computing, and Global Seismology. *Science*, 298(5599):1737–1742, 2002.

[193] D. Komatitsch and R. Martin. An unsplit convolutional Perfectly Matched Layer improved at grazing incidence for the seismic wave equation. *Geophysics*, 72(5):SM155–SM167, 2007.

[194] W. Köppen. Die Wärmezonen der Erde, nach der Dauer der heissen, gemässigten und kalten Zeit und nach der Wirkung der Wärme auf die organische Welt betrachtet. *Meteorol. Z.*, 1:215–226, 1884.

[195] W. Köppen. Klassifikation der Klimate nach Temperatur, Niederschlag und Jahresablauf . *Petermanns Geogr. Mitt.,*, 64:93–203, 243–248, 1918.

[196] W. Köppen. *Handbuch der Klimatologie*. Verlag von Gebrüder Borntlaeger, W 35 Koester Ufer 17, 1936.

[197] V. Korneev. Resonant seismic emission of subsurface objects. *Geophysics*, 74(2):T47–T53, 2009.

[198] E. Kragh and L. Peardon. Ground roll and polarization. *First Break*, 13(9):369–378, 1995.

[199] D. O. Krimer, M. Pfitzner, K. Bräuer, Y. Jiang, and M. Liu. Granular elasticity: General considerations and the stress dip in sand piles. *Phys. Rev. E*, 74:061310, 2006.

[200] K. Kroy, S. Fischer, and B. Obermayer. The shape of barchan dunes. *Journal of Physics: Condensed Matter*, 17(14):S1229, 2005.

[201] K. Kroy, G. Sauermann, and H. J. Herrmann. Minimal model for aeolian sand dunes. *Phys. Rev. E*, 66:031302, 2002.

[202] P. M. C. Lacey. Development in the theory of particle mixing. *J. Appl. Chem.*, 4:257, 1954.

[203] K. Lambeck. Shoreline reconstructions for the Persian Gulf since the last glacial maximum. *Earth and Planetary Science Letters*, 142(1):43–57, 1996.

[204] N. Lancaster. Grain size characteristics of Namib Desert linear dunes. *Sedimentology*, 28(1):115–122, 1981.

[205] N. Lancaster. Dunes on the skeleton coast, Namibia (South West Africa): Geomorphology and grain size relationships. *Earth Surface Processes and Landforms*, 7(6):575–587, 1982.

[206] F. Lavoie, L. Cartilier, and R. Thibert. New Methods Characterizing Avalanche Behavior to Determine Powder Flow. *Pharmaceutical Research*, 19(6):887–893, 2002.

[207] P.-A. Lemieux and D. J. Durian. From Avalanches to Fluid Flow: A Continuous Picture of Grain Dynamics Down a Heap. *Phys. Rev. Lett.*, 85:4273–4276, 2000.

[208] E. C. Leong and H. Rahardjo. Review of Soil-Water Characteristic Curve Equations. *Journal of Geotechnical and Geoenvironmental Engineering*, 123(12):1106–1117, 1997.

[209] A. R. Levander. Seismic scattering near the earth's surface. *Pure and Applied Geophysics*, 132(1):21–47, 1990.

[210] Y. Li, J. Cui, T. Zhang, T. Okuro, and S. Drake. Effectiveness of sand-fixing measures on desert land restoration in Kerqin Sandy Land, northern China. *Ecological Engineering*, 35(1):118–127, 2009.

[211] Z. S. Li, D. J. Feng, S. L. Wu, A. G. L. Borthwick, and J. R. Ni. Grain size and transport

characteristics of non-uniform sand in aeolian saltation. *Geomorphology*, 100(3):484–493, 2008.

[212] Y. Ling, J. Gao, and R. Zhang. Sand dune reverberation and its suppression. *The Leading Edge*, 17(5):697–702, 1998.

[213] M. Logie. Wind tunnel experiments on dune sands. *Earth Surface Processes and Landforms*, 6:365–374, 1981.

[214] D. B. Loope. Dry-Season Tracks in Dinosaur-Triggered Grainflows. *PALAIOS*, 21(2):132–142, 2006.

[215] D. B. Loope, J. F. Elder, and M. R. Sweeney. Downslope coarsening in aeolian grainflows of the Navajo Sandstone. *Sedimentary Geology*, 265–266(0):156–162, 2012.

[216] O. M. Lopez, K. Z. Jadoon, and T. M. Missimer. Method of Relating Grain Size Distribution to Hydraulic Conductivity in Dune Sands to Assist in Assessing Managed Aquifer Recharge Projects: Wadi Khulays Dune Field, Western Saudi Arabia. *Water*, 7(11):6411–6426, 2015.

[217] M. Y. Louge, A. Valance, A. O. el Moctar, J. Xu, A. G. Hay, and R. Richer. Temperature and humidity within a mobile barchan sand dune, implications for microbial survival. *Journal of Geophysical Research: Earth Surface*, 118(4):2392–2405, 2013.

[218] B. H. Luckman. Talus Slopes. In S. A. Elias, editor, *The Encyclopedia of Quaternary Science, vol. 3*, pages pp. 566–573. Elsevier, 2013.

[219] H. A. Makse. Stratification instability in granular flows. *Phys. Rev. E*, 56:7008–7016, 1997.

[220] H. A. Makse, P. Cizeau, and H. E. Stanley. Possible Stratification Mechanism in Granular Mixtures. *Phys. Rev. Lett.*, 78:3298–3301, 1997.

[221] H. A. Makse, S. Havlin, P. R. King, and S. H. Eugene. Spontaneous stratification in granular mixtures. *Nature*, 386:379, 1997.

[222] Malvern Instruments. Malvern Instruments Mastersizer 2000 Specification. `http://www.malvern.com/en/products/product-range/mastersizer-range/mastersizer-2000/`, 2015.

[223] F. Masrouri, K. Bicalho, and K. Kawai. Laboratory Hydraulic Testing in Unsaturated Soils. 26:691–704, 2008.

[224] H. Matthée. Segregation phenomena relating to bunkering of bulk materials: Theoret-

ical considerations and experimental investigations. *Powder Technology*, 1(5):265–271, 1968.

[225] G. Mavko, T. Mukerji, and J. Dvorkin. *The Rock Physics Handbook: Tools for Seismic Analysis of Porous Media*. Stanford-Cambridge program. Cambridge University Press, 2003.

[226] L. B. H. May, L. A. Golick, K. C. Phillips, M. Shearer, and K. E. Daniels. Shear-driven size segregation of granular materials: Modeling and experiment. *Phys. Rev. E*, 81:051301, 2010.

[227] J. T. McCord and D. B. Stephens. Lateral moisture flow beneath a sandy hillslope without an apparent impeding layer. *Hydrological Processes*, 1(3):225–238, 1987.

[228] E. D. McKee. Small-Scale Structures in the Coconino Sandstone of Northern Arizona. *The Journal of Geology*, 53(5):313–325, 1945.

[229] E. D. McKee. Structures of dunes at White Sands National Monument, New Mexico (and a comparison with structures of dunes of from other selected areas). *Sedimentology*, 7(1):3–69, 1966.

[230] E. D. McKee. A study of global sand seas. Technical report, USGS, 1979.

[231] E. D. McKee. *Sedimentary structures in dunes of the Namib Desert, South West Africa*. Geological Society of America, Boulder, Colo, 1982.

[232] G. F. Miller and H. Pursey. On the Partition of Energy between Elastic Waves in a Semi-Infinite Solid. *Proceedings of the Royal Society of London A: Mathematical, Physical and Engineering Sciences*, 233(1192):55–69, 1955.

[233] C. O. Mohr. *Zivilingenieur*. W. Ernst und Sohn, 1882.

[234] C. Moore and J. Masliyah. Study in particle percolation: Computer program. *International Journal for Numerical Methods in Engineering*, 6(1):25–32, 1973.

[235] P. S. Mozley and J. M. Davis. Internal structure and mode of growth of elongate calcite concretions: Evidence for small-scale, microbially induced, chemical heterogeneity in groundwater. *GSA Bulletin*, 117(11-12):1400, 2005.

[236] S. J. Nasir, I. A. El-Kassas, and A. A. M. Sadiq. Mineralogy and Genesis of Heavy Minerals in Coastal Dune Sands, South Eastern Qatar. *Qatar University Science Journal*, 19:184–201, 1999.

[237] A. Neal. Ground-penetrating radar and its use in sedimentology: principles, problems

and progress. *Earth-Science Reviews*, 66(3–4):261–330, 2004.

[238] J. M. Nield, G. F. S. Wiggs, M. C. Baddock, and M. H. T. Hipondoka. Coupling leeside grainfall to avalanche characteristics in aeolian dune dynamics. *Geology*, 45(3):271, 2017.

[239] N. Nityanand, B. Manley, and H. Henein. An analysis of radial segregation for different sized spherical solids in rotary cylinders. *Metallurgical Transactions B*, 17(2):247–257, 1986.

[240] Y. Oyama. Horizontal rotating cylinder. *Bull. Inst. Phys. Chem. Res. (Tokyo)*, 18(5):600, 1939. (in Japanese).

[241] N. G. Patil and S. K. Singh. Pedotransfer Functions for Estimating Soil Hydraulic Properties: A Review. *Pedosphere*, 26(4):417–430, 2016.

[242] J. D. Pelletier, D. J. Sherman, J. T. Ellis, E. J. Farrell, N. L. Jackson, B. Li, K. F. Nordstrom, L. P. Maia, and M. Omidyeganeh. Dynamics of sediment storage and release on aeolian dune slip faces: A field study in Jericoacoara, Brazil. *Journal of Geophysical Research: Earth Surface*, 120(9):1911–1934, 2015.

[243] D. Peter, D. Komatitsch, Y. Luo, R. Martin, N. Le Goff, E. Casarotti, P. Le Loher, F. Magnoni, Q. Liu, C. Blitz, T. Nissen-Meyer, P. Basini, and J. Tromp. Forward and adjoint simulations of seismic wave propagation on fully unstructured hexahedral meshes. *Geophys. J. Int.*, 186(2):721–739, 2011.

[244] A. Piccolroaz, D. Bigoni, and A. Gajo. An elastoplastic framework for granular materials becoming cohesive through mechanical densification. Part II – the formulation of elastoplastic coupling at large strain. *European Journal of Mechanics - A/Solids*, 25(2):358–369, 2006.

[245] A. Poulovassilis. The effect of hysteresis of pore-water on the hydraulic conductivity. *Journal of Soil Science*, 20(1):52–56, 1969.

[246] G. Power. *Modelling Granular Flow in Caving Mines: Large Scale Physical Modelling and Full Scale Experiments*. PhD thesis, 2004.

[247] R. Qian, J. Li, L. Liu, and Z. Zhao. Internal Structure of Sand Dunes in the Badain Jaran Desert Revealed by GPR and Its Implications to Inter-Dune Lake Hydrology. In *Ground Penetrating Radar (GPR), 2014 15th International Conference on*, pages 166–169. 15th International Conference on Ground Penetrating Radar - GPR 2014, IEEE, 2014.

[248] L. Quartier, B. Andreotti, S. Douady, and A. Daerr. Dynamics of a grain on a sandpile model. *Phys. Rev. E*, 62:8299–8307, 2000.

[249] M. Rahman, K. Shinohara, H. P. Zhu, A. B. Yu, and P. Zulli. Size segregation mechanism of binary particle mixture in forming a conical pile. *Chemical Engineering Science*, 66(23):6089–6098, 2011.

[250] W. S. Rasband. ImageJ, 1997—2012. imagej.nih.gov/ij/.

[251] C. J. Regone. *11. Measurement and Identification of 3-D Coherent Noise Generated from Irregular Surface Carbonates*, pages 281–306. 1997.

[252] O. Reynolds. On the dilatancy of media composed of rigid particles in contact. With experimental illustrations. *Philosophical Magazine Series 5*, 20(127):469–481, 1885.

[253] L. A. Richards. Capillary conduction of liquids through porous mediums. *Journal of Applied Physics*, 1:318, 1931.

[254] L. A. Richards and L. R. Weaver. Moisture retention by some irrigated soils as related to soil moisture tension. *Journal of Agricultural Research*, 69:215–235, 1944.

[255] L. F. Richardson. *Weather prediction by numerical process*, page 105. Cambridge University Press, 1922.

[256] F. E. Richart, J. R. Hall, and R. D. Woods. *Vibrations of soils and foundations*. Prentice-Hall international series in theoretical and applied mechanics. Prentice-Hall, 1970.

[257] C. J. Ritsema and L. W. Dekker. Soil moisture and dry bulk density patterns in bare dune sands. *Journal of Hydrology*, 154(1):107–131, 1994.

[258] L. R. F. Rose. On the energy radiated by Rayleigh waves. *Wave Motion*, 6(4):359–361, 1984.

[259] D. M. Rubin and R. E. Hunter. Bedform climbing in theory and nature. *Sedimentology*, 29(1):121–138, 1982.

[260] A. Saint-Venant. Théorie du mouvement non permanent des eaux, avec application aux crues des rivières et à l'introduction de marées dans leurs lits. *Comptes Rendus des Séances de l'Académie des Sciences*, 73:147–154, 1871.

[261] A. H. Sallenger. Inverse grading and hydraulic equivalence in grain-flow deposits. *Journal of Sedimentary Research*, 49(2):553, 1979.

[262] S. B. Savage and K. Hutter. The motion of a finite mass of granular material down a rough incline. *Journal of Fluid Mechanics*, 199:177–215, 1989.

[263] S. B. Savage and C. K. K. Lun. Particle size segregation in inclined chute flow of dry cohesionless granular solids. *Journal of Fluid Mechanics*, 189:311–335, 1988.

[264] S. K. Saxena and R. M. Lastrico. Static properties of lightly cemented sand. *J. Geotech. Eng. Div.*, 104:1449–1464, 1978.

[265] A. Schofield and P. Wroth. *Critical State Soil Mechanics*. McGraw-Hill, 1968.

[266] A. M. Scott and J. Bridgwater. Interparticle Percolation: A Fundamental Solids Mixing Mechanism. *Industrial & Engineering Chemistry Fundamentals*, 14(1):22–27, 1975.

[267] H. Selmani, A. Valance, A. O. E. Moctar, P. Dupont, and R. Zegadi. Aeolian Sand Transport in Out-of-Equilibrium Regimes. *Geophysical Research Letters*, 45(4):1838–1844, 2018.

[268] M. Shimokawa and S. Ohta. Dual stratification of a sand pile formed by trapped kink. *Physics Letters A*, 366(6):591–595, 2007.

[269] M. Shimokawa and S. Ohta. Spontaneous formation of dual stratification patterns in a large quasi-two-dimensional sand pile. *Phys. Rev. E*, 77:011305, 2008.

[270] K. Shinohara, K. Shoji, and T. Tanaka. Mechanism of Size Segregation of Particles in Filling a Hopper. *Industrial & Engineering Chemistry Process Design and Development*, 11(3):369–376, 1972.

[271] K. Shinohara, K. Shoji, and T. Tanaka. Mechanism of Segregation and Blending of Particles Flowing out of Mass-Flow Hoppers. *Industrial & Engineering Chemistry Process Design and Development*, 9(2):174–180, 1970.

[272] J. Smid and J. Novosad. Pressure Distribution under Heaped Bulk Solids. *Proceedings of 1981 Powtech. Conference*, page 63, 1981.

[273] A. Sneh and T. Weissbrod. Size—frequency distribution of longitudinal dune rippled flank sands compared to that of slipface sands of various dune types. *Sedimentology*, 30(5):717–725, 1983.

[274] H. C. Sorby. On the structures produced by the currents present during the deposition of stratified rocks. *Geologist*, 2:137–47, 1859.

[275] V. Stabnikov, M. Naeimi, V. Ivanov, and J. Chu. Formation of water-impermeable crust on sand surface using biocement. *Cement and Concrete Research*, 41(11):1143–1149, 2011.

[276] K. O. Stanley, W. M. Jordan, and J. R. H. Dott. New Hypothesis of Early Jurassic

Paleogeography and Sediment Dispersal for Western United States. *AAPG Bulletin*, 55(10):1–19, 1971.

[277] W. L. Stokes. Multiple parallel-truncation bedding planes; a feature of wind-deposited sandstone formations. *Journal of Sedimentary Research*, 38(2):510, 1968.

[278] M. Sugimoto and K. Yamamoto. On the Permeation Effects of Particles in a Moving Bed. *Journal of the Society of Materials Science, Japan*, 22(238):684–688, 1973.

[279] S. L. F. Sutton, C. McKenna Neuman, and W. Nickling. Avalanche grainflow on a simulated aeolian dune. *Journal of Geophysical Research: Earth Surface*, 118(3):1767–1776, 2013.

[280] D. Takagi, J. N. McElwaine, and H. E. Huppert. Shallow granular flows. *Phys. Rev. E*, 83:031306, 2011.

[281] W. Tao. Aeolian desertification and its control in Northern China. *International Soil and Water Conservation Research*, 2(4):34–41, 2014.

[282] N. Thomas. Reverse and intermediate segregation of large beads in dry granular media. *Phys. Rev. E*, 62:961–974, 2000.

[283] O. Tiapkina, M. Landrø, Y. Tyapkin, and B. Link. Single-station SVD-based polarization filtering of ground roll: Perfection and investigation of limitations and pitfalls. *Geophysics*, 77(2):V41–V59, 2012.

[284] J. Tromp, D. Komatitsch, and Q. Liu. Spectral-element and adjoint methods in seismology. *Communications in Computational Physics*, 3(1):1–32, 2008.

[285] M. E. Tucker. *Sedimentary Rocks in the Field*. Wiley, 2003.

[286] A. Valance, K. R. Rasmussen, A. O. E. Moctar, and P. Dupont. The physics of Aeolian sand transport. *Comptes Rendus Physique*, 16(1):105–117, 2015.

[287] K. van der Vaart, P. Gajjar, G. Epely-Chauvin, N. Andreini, J. M. N. T. Gray, and C. Ancey. Underlying Asymmetry within Particle Size Segregation. *Phys. Rev. Lett.*, 114:238001, 2015.

[288] M. T. van Genuchten. A closed-form equation for predicting the hydraulic conductivity of unsaturated soils. *Soil Science Society of America Journal*, 44(5):892–898, 1980.

[289] L. Vanel, P. Claudin, J.-P. Bouchaud, M. E. Cates, E. Clément, and J. P. Wittmer. Stresses in Silos: Comparison Between Theoretical Models and New Experiments. *Phys. Rev. Lett.*, 84:1439–1442, 2000.

[290] G. Vermeer. *3D Seismic Survey Design, Second Edition*. Society of Exploration Geophysicists, 2012.

[291] Visiongain. Land Seismic Equipment & Acquisition Market Forecast 2017-2027. Technical report, 2017.

[292] D. Volfson, L. S. Tsimring, and I. S. Aranson. Order Parameter Description of Stationary Partially Fluidized Shear Granular Flows. *Phys. Rev. Lett.*, 90:254301, 2003.

[293] N. M. Vriend, M. L. Hunt, and R. W. Clayton. Linear and nonlinear wave propagation in booming sand dunes. *Physics of Fluids*, 27(10):103305, 2015.

[294] N. M. Vriend, M. L. Hunt, R. W. Clayton, C. E. Brennen, K. S. Brantley, and A. Ruiz-Angulo. Solving the mystery of booming sand dunes. *Geophysical Research Letters*, 34(16), 2007.

[295] K. Walton. The effective elastic moduli of a random packing of spheres. *Journal of the Mechanics and Physics of Solids*, 35(2):213–226, 1987.

[296] N. W. Watkins, G. Pruessner, S. C. Chapman, N. B. Crosby, and H. J. Jensen. 25 Years of Self-organized Criticality: Concepts and Controversies. *Space Science Reviews*, 198(1):3–44, 2016.

[297] A. Watson. The control of wind blown sand and moving dunes: a review of the methods of sand control in deserts, with observations from Saudi Arabia. *Quarterly Journal of Engineering Geology and Hydrogeology*, 18(3):237, 1985.

[298] A. Watson. Grain-size variations on a longitudinal dune and a barchan dune. *Sedimentary Geology*, 46(1–2):49–66, 1986.

[299] W. Whalley, E. Ober, and M. Jenkins. Measurement of the matric potential of soil water in the rhizosphere. *Journal of Experimental Botany*, 64(13), 2013.

[300] S. D. Wicksell. The Corpuscule Problem. A Mathematical Study of a Biometric Problem. *Biometrika*, 17(1-2):84–99, 1925.

[301] S. Wiederseiner, N. Andreini, G. Épely-Chauvin, G. Moser, M. Monnereau, J. M. N. T. Gray, and C. Ancey. Experimental investigation into segregating granular flows down chutes. *Physics of Fluids*, 23(1):013301, 2011.

[302] G. F. S. Wiggs, I. Livingstone, and A. Warren. The role of streamline curvature in sand dune dynamics: evidence from field and wind tunnel measurements. *Geomorphology*, 17(1):29–46, 1996.

[303] S. S. Wilks. The Large-Sample Distribution of the Likelihood Ratio for Testing Composite Hypotheses. *Ann. Math. Statist.*, 9(1):60–62, 1938.

[304] D. Williams. *Linear Models, ANOVA, etc*, pages 283–382. Cambridge University Press, 2001.

[305] J. C. Williams. The segregation of powders and granular materials. *Fuel Society Journal*, 14(29), 1963.

[306] J. C. Williams. The mixing of dry powders. *Powder Technology*, 2(1):13–20, 1968.

[307] J. C. Williams and G. Shields. The segregation of granules in a vibrated bed. *Powder Technology*, 1(3):134–142, 1967.

[308] J. P. Wittmer, M. E. Cates, and P. Claudin. Stress propagation and Arching in Static Sandpiles. *Journal de Physique I*, 7(1):39–80, 1997.

[309] J. P. Wittmer, P. Claudin, M. E. Cates, and J.-P. Bouchaud. An explanation for the central stress minimum in sand piles. *Nature*, 382:336, 1996.

[310] J. Xu and M. Y. Louge. Statistical mechanics of unsaturated porous media. *Phys. Rev. E*, 92:062405, 2015.

[311] X.-H. Xu, G.-Z. Qu, Y. Zhang, Y.-Y. Bi, and J.-J. Wang. Ground-roll separation of seismic data based on morphological component analysis in two-dimensional domain. *Applied Geophysics*, 13(1):116–126, 2016.

[312] D. H. Yaalon and J. Laronne. Internal structures in eolianites and paleowinds, Mediterranean coast, Israel. *Journal of Sedimentary Research*, 41(4):1059, 1971.

[313] X. Yang, T. Liu, and H. Xiao. Evolution of megadunes and lakes in the Badain Jaran Desert, Inner Mongolia, China during the last 31,000 years. *Quaternary International*, 104(1):99–112, 2003.

[314] P. Yu and F. E. Richart. Stress Ratio Effects on Shear Modulus of Dry Sands. *Journal of Geotechnical Engineering*, 110(3):331–345, 1984.

[315] H. W. Zhou. *Practical Seismic Data Analysis*. Cambridge University Press, 2014.

[316] B.-Q. Zhu, J.-J. Yu, P. Rioual, and X.-Z. Ren. Particle size variation of aeolian dune deposits in the lower reaches of the Heihe River basin, China. *Sedimentary Geology*, 301(0):54–69, 2014.

[317] Z. Zhu. Status and trend of desertification in northern China. *Journal of Desert Research*, 5(3):3–11, 1985.

[318] M. A. Zimmer, M. Prasad, G. Mavko, and A. Nur. Seismic velocities of unconsolidated sands: Part 1 — Pressure trends from 0.1 to 20 MPa. *Geophysics*, 72(1):E1–E13, 2007.

[319] K. Zoeppritz. Über Reflexion und Durchgang seismischer Wellen durch Unstetigkeitsflächen. *Nachrichten von der Gesellschaft der Wissenschaften zu Göttingen, Mathematisch-Physikalische Klasse*, 1919:66–84, 1919.

[320] I. Zuriguel and T. Mullin. The role of particle shape on the stress distribution in a sandpile. *Proceedings of the Royal Society of London A: Mathematical, Physical and Engineering Sciences*, 464(2089):99–116, 2008.